FACULTY OF ENGINEERING
AND ARCHITECTURE

Towards an Integrated Photonic Scanning FMCW LiDAR Using a Single Wavelength Variable

Mennatallah Ali Zakaria Kandil

Doctoral dissertation submitted to obtain the academic degree of
Doctor of Photonics Engineering

Supervisors

Prof. Wim Bogaerts, PhD* - Marcus Dahlem, PhD**

* Department of Information Technology
Faculty of Engineering and Architecture, Ghent University

** imec

March 2026

GHENT
UNIVERSITY

ISBN 978-94-93513-30-3
NUR 959
Wettelijk depot: D/2026/10.500/38

Members of the Examination Board

Chair

Prof. Filip De Turck, PhD, Ghent University

Other members entitled to vote

Prof. Johan Bauwelinck, PhD, Ghent University
Prof. Martijn Heck, PhD, Technische Universiteit Eindhoven, the Netherlands
Prof. Hao Hu, PhD, Danmarks Tekniske Universitet, Denmark
Prof. Yanlu Li, PhD, Ghent University

Supervisors

Prof. Wim Bogaerts, PhD, Ghent University
Marcus Dahlem, PhD, imec

Acknowledgments

It has been short-long four years, where I would not have reached this milestone and I would not have grown as a person without the support or just the mere presence of the people I met along the way. I would like to start by thanking my promotors Wim and Marcus for allowing me to have the best of both worlds of the photonics research group in UGent and of imec in Leuven, and for giving me enough space for autonomy. Thanks Wim for all that I learned from you on the technical level and the ethical level. I believe I still have a lot to learn from you, and maybe our paths will cross again for me to learn more. Thanks Marcus for what you taught me specially on the industry level, and for facilitating my access to many resources. For me, I am always most grateful for the gift of empathy and understanding .. sometimes what you need is when your supervisors share an experience that tells you that they went through similar moments, or when they support you when you are drenched in self-doubt. One of the defining moments for me was the conversation I had with Wim in the summer school of photonics after my second year, maybe he doesn't remember it, but it made a difference. And Marcus, you have always reminded me of my potential and never made me feel a distance between me and you as as supervisor which helped me in anxious times. I can not mention empathy without mentioning my daily supervisor Jon Kjellman. You heard infinite amount of rambling from me, helped me refocus and guided me on the technical level, even before becoming my supervisor. My thanks are extended to my "shadow"mentor Mathias prost who offered his time and expertise on the ground from the tapeouts to the the lab work and more. I learned a lot from you.

In a probably failed attempt to capture a picture of the span of the four years of PhD and even the six years in Belgium, there are a lot of people who I met in imec and outside who shaped me, provided companionship and support, even if they don't realize it. I decided for that to follow a semi-chronological approach :) Dear reader, if you made it till here, then just be careful as there will be quite some yapping.

In the first few months of my PhD, I was lucky to meet a bunch of great people in just one floor in imec 2 and then imec 1, Els with her delicate soul, Bogdan and all the chats on philosophy and books, Alberto's imec tips and tricks, Cedric who shared the PhD misery journey and the occasional drawing, Fabrice who made the

place lively, Jeonghwan who told me to run away from photonics ;), our senior PhD Anabel, our cookie monster Ugo, Bruno, Sarvagya, and more .. Then comes all the coffee chats with Tangla and Mathias, and all the prince of Cameroon stories, Saeed with all the humanism and cynicism. Oksana, you have been really a role model for me, a brilliant scientist, a truly loving mother, and a kind woman with a big honest heart. I would not forget my Arabic speaking fellows, Sarah whose love for culture and open mind inspired me, and the fellow Egyptians Kareem and Mahmoud, and all the Ahmeds. I am also thankful to Huaqing and our chats about imec, photonics, disappointments and publications, Manuel with the fighty discussions and to Joonyoung who supported me and is mentoring me in my system engineer transition, Michal and Adam who were great to work with in the end of my PhD. There are more and more people in PRG, Roelof's and Joost's team and the whole imec; Maritza, Filip, Giammarco, Florian, Zeinab, Rossa, Iakov, Racha, Meryem, Nouha, Amir, Liwang, Pieter, Chinmay, Yu, Guillaume, Jing, Ewoud, Dennis, Marjan, Lisa, Valeria, Nirav, Rio, Patrick, Behrooz, Alaeddine, Mulham, Konstantinos, Vladimir (and Nina), Christian, Farhan, Tom, Tingting, Oguz and more ..

My girls who made my family abroad for the past six years of master's and PhD, I love you and I can not be more grateful. Doha, who was there whenever I needed help, who I tried to learn from her strength, who was my flatmate, I hope you and all who are around you the safety in Gaza, May Allah bless you with hopes and dreams that you achieve, and May I see you soon. Woroud, my partner in crime with all the therapy sessions, coffee, desserts, trips and non-executed plans :), May Allah keep your family safe in Gaza and reunite you with them. Alaa, my friend and flatmate, I consider our shenanigans are that of sisters, where our understanding of each other is proven by code names and endless discussions. Elif and Aseel whom I met in the first year of PhD when I was emerging from the darkness of my master's time, you can not imagine how much you helped me and how much I hope we meet again. Maja, who I was blessed to know through imec, the loving giver and rebel with all our similarities and vulnerabilities. Sarah Masaad who I was blessed to know through PRG, I can count on my hand the times we got to meet, but these times were so rich with perspectives and shared experience, I actually look up to you although you are younger than me. Yasmin, I truly feel revived when I meet you and listen to your stories and I am grateful for your support before my private defense, I admire your strength and I cherish the time I get visiting you and your lovely family. Nayera, I just felt safe knowing that you and your family are in Leuven, I truly cherish the moments I spent with you and your three lovely daughters whether it is playing Nintendo, going to the funfair or just having a meal. Jidaa, my temp flatmate and my friend who I learned a lot from, I hope we meet again. Bassant who has been here for a little bit but left her mark. And for more girls who made Leuven a home; Amena, Sarah Salama (Hossam Koko Bookclub), Dina, Nagham, Shorouk, Nuha, Kholoud, Samar, Dalia, Menna, Reem, and Imsal girls. Alhamdulillah, for he blessed me with these honest, kind, and helpful people ...

Now I ought to move to my world-split, if I may call it, for my worlds in Belgium and Egypt have been oddly split and are yet to meet. My dear friends from Bachelor's time, forgive me acting like a ghost, I hope we all reunite one day. Reham, I can not count how many calls we had in my first year of master's, you were there for me, and I wish I was there for you in the subsequent years. Sarah, you will always be my gd3a friend, Nehal, you will always be my wise friend and I wish I was more there for you girls. Esraa, I don't know if I will get to show you this thesis, but you have always been in my mind. Maha, Marwa and Raghda who showed me support whenever we got to meet. Maryam who often checked on me, Aya and Aya, and Alaa.. Menna, my friend since teenage time, my reference frame, with the antenna connection, whenever we meet I get reminded of who I am ..

And finally, thank you my dear parents whom I would have never achieved anything without you, Thank you Baba and Mama. Mama you have been always in my back, from Thanawya exams to my Ielts exam trip and my Cairo shenanigans .. Nana (may Allah bless your soul) you were always waiting for me to come back .. my brothers Mohammed and Omar, I will always count on you < 3

Menna Kandil
Leuven/Damietta, March 2026

Contents

List of Acronyms

A

ADAS	Advanced Driver-Assistance Systems
AWG	Arrayed Waveguide Gratings

B

BTO	Barium Titanate
BPD	Balanced Photodetector

C

CMOS	Complementary Metal Oxide Semiconductor
CRLB	Cramér–Rao Lower Bound

D

DOPA	Dispersive Optical Phased Array
DFB	Distributed Feedback
DBR	Distributed Bragg Reflector
DSP	Digital Signal Processing

E

ECL	External Cavity Laser

F

FoV	Field of View
FMCW	Frequency-Modulated Continuous-Wave
FPA	Focal Plane Array
FT	Fourier Transform
FFT	Fast Fourier Transform
FWHM	Full-Width at Half-Maximum
FSR	Free Spectral Range
FDTD	Finite-Difference Time-Domain
FD-OCT	Frequency-Domain Optical Coherence Tomography
FA	Fiber Array

I

InP	Indium Phosphide

L

LiDAR	Light Detection and Ranging
LNO	Lithium Niobate
LO	Local Oscillator
LPCVD	Low Pressure Chemical Vapor Deposition

M

MEMS	Micro-Electro-Mechanical Systems
MMI	Multi-Mode Interferometer
MZI	Mach-Zehnder Interferometer
MTP	Micro-Transfer-Printing

N

NEP	Noise Equivalent Power

O

OPA	Optical Phased Array

P

PIC	Photonic Integrated Circuit
PDK	Process Design Kit
PCB	Printed Circuit Board

R

RX	Receiver
RF	Radio-Frequency
ROI	Region OF Interest

S

SWaP	Size Weight and Power

SOI	Silicon-On-Insulator
SiN	Silicon Nitride
SNR	Signal-to-Noise Ratio
SLSR	Side Lobe Suppression Ratio
SOA	Semiconductor Optical Amplifier

T

TX	Transmitter
ToF	Time-of-Flight
TEC	Thermoelectric Cooler

Samenvatting

1 Inleiding

Geïntegreerde fotonica maakt compacte, schaalbare en energiezuinige optische systemen mogelijk door traditionele, omvangrijke optische componenten te miniaturiseren tot chipniveau, wat aanzienlijke verbeteringen oplevert in omvang, gewicht en energieverbruik (SWaP). Hoewel de ontwikkeling aanvankelijk werd gedreven door optische communicatie, met name in de telecom- en datacomsector, heeft het vakgebied zich inmiddels uitgebreid naar nieuwe domeinen zoals computing, LiDAR, biomedische beeldvorming en milieumonitoring.

In de kern opereert geïntegreerde fotonica over meerdere hiërarchische niveaus. Op componentniveau omvat het apparaten voor lichtgeneratie, modulatie, geleiding en detectie. Wanneer deze componenten onderling worden verbonden via optische golfgeleiders, vormen zij fotonisch geïntegreerde schakelingen (PIC's) die geavanceerde functies kunnen uitvoeren, zoals coherente detectie en optische bundelsturing. Het opschalen van deze schakelingen tot volledige fotonische systemen brengt echter extra uitdagingen met zich mee, waaronder verpakking, thermisch beheer en fabricagevariaties, die allemaal invloed hebben op de opbrengst en prestaties van de systemen waarin ze worden geïntegreerd.

Binnen deze bredere context heeft de automobielindustrie een cruciale rol gespeeld bij de ontwikkeling van langeafstands-LiDAR-systemen zonder bewegende onderdelen., die een essentieel onderdeel vormen van sensorfusie in geavanceerde rijhulpsystemen (ADAS). Het primaire doel van een LiDAR-systeem is het reconstrueren van een driedimensionale puntenwolk van de omgeving door twee fundamentele functies te combineren: belichting en afstandsbepaling. Dit wordt bereikt door de scène te belichten met een zender; wanneer het uitgezonden optische signaal een object raakt, wordt het gereflecteerd en opgevangen door de ontvanger. De ontvanger bepaalt vervolgens de afstand tot het object door de tijdsvertraging te meten tussen het uitgezonden signaal en het teruggekaatste licht. In dit proefschrift dient optische bundelsturing als belichtingsmechanisme, terwijl frequentiegemoduleerde continue golf (FMCW)-afstandsbepaling wordt toegepast voor het meten van afstanden.

Het onderzoek dat in dit proefschrift wordt gepresenteerd, bevindt zich op het

snijvlak van fotonisch circuit- en systeemontwerp en verkent architecturen die deze twee LiDAR-functies integreren. Door gebruik te maken van golflengteafstemming kan één en hetzelfde mechanisme zowel bundelsturing als afstandsbepaling mogelijk maken, waarmee de basis wordt gelegd voor een volledig geïntegreerd LiDAR-systeem dat wordt aangestuurd door één enkele golflengtevariabele.

2 Dispersieve optische faserarrays

Een optische faserarray bestaat uit meerdere antennes die in één of twee dimensies zijn gerangschikt, waarbij de relatieve fase en amplitude van de signalen die elke antenne voeden, het stralingspatroon in het verre veld bepalen. In geïntegreerde fotonica kunnen lange golfgeleiderroosters fungeren als optische antennes. Wanneer deze uniform worden gerangschikt en met een vaste fase-increment worden gevoed, produceren ze een gecollimeerde bundel in het verre veld waarvan de richting afhangt van dat faseverschil, wat niet-mechanische bundelsturing mogelijk maakt via elektronische of optische fasecontrole.

In dit werk wordt bundelsturing uitsluitend gerealiseerd door het afstemmen van de lasergolflengte, waardoor actieve fase-actuatoren overbodig worden. Door vaste padlengteverschillen tussen de antennes te introduceren via vertraginglijnen, wordt de relatieve fase golflengte-afhankelijk en wordt bundelsturing in één richting bereikt. In de andere richting wordt bundelsturing verkregen door lange golfgeleiderroosters, waarvan de stralingshoek golflengte-afhankelijk is volgens de dispersie van het rooster. Dit principe definieert de dispersieve optische faserarray (DOPA), waarbij elke golflengte overeenkomt met een specifieke richting in het verre veld, wat continue, golflengte-afhankelijke scanning mogelijk maakt.

Deze continue DOPA's kampen echter met verschillende schaalbaarheidsproblemen, waaronder een groot oppervlak, hoge invoegverliezen en opgehoopte fasefouten, voornamelijk veroorzaakt door de omvang van het optische verdelingsnetwerk. Dit motiveert het onderzoek naar oplossingen die de grootte van het verdelingsnetwerk verkleinen, terwijl de vereiste prestaties behouden blijven.

In dit proefschrift wordt het concept van de gepixelde DOPA voorgesteld, waarbij het verdelingsnetwerk wordt opgedeeld in kleinere blokken. Hierdoor blijft de apertuurgrootte gelijk aan die van de continue DOPA, maar wordt de hoekresolutie in het verre veld losgekoppeld van de bundeldivergentie. Gepixelde DOPA's verkorten de totale vertraginglengte zonder het gezichtsveld of de bundeldivergentie aan te tasten en bieden zo een compactere en beter schaalbare oplossing voor projectie over lange afstanden. Terwijl de lasergolflengte wordt verschoven, ontstaan smalle bundels alleen bij discrete werkgolflengten, die elk overeenkomen met een specifiek punt in het verre veld, wat resulteert in een gepixelde in plaats van een continue scan.

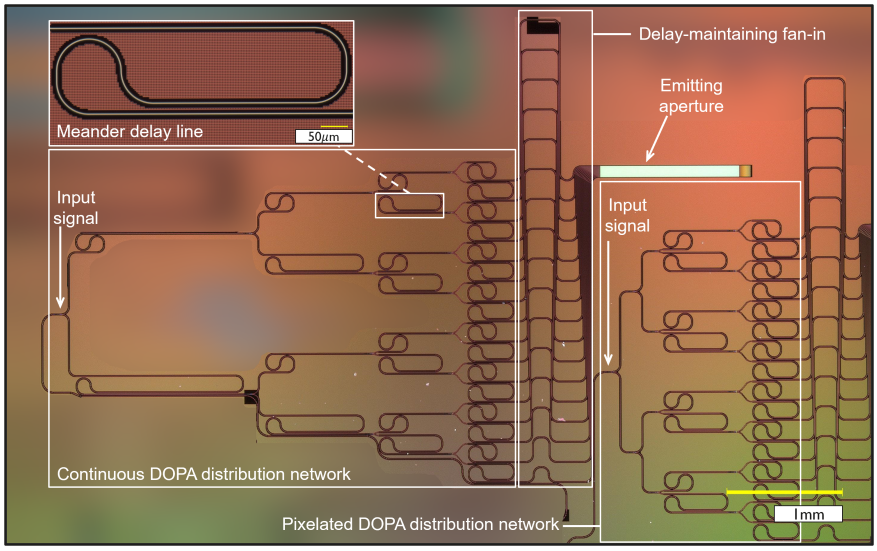

Figuur 1: Microscoopbeeld dat het circuit van de continue DOPA en het verdelingsnetwerk van de gepixelde DOPA toont.

3 Experimentele evaluatie van continue en gepixelde DOPA's voor 2D-bundelsturing

We presenteren twee kleinschalige demonstraties van dispersieve optische faserarrays (DOPA's) om de prestaties van de gepixelde architectuur te vergelijken met die van het conventionele, continue ontwerp. Beide implementaties maken gebruik van een nieuw lichtverdelingsnetwerk gebaseerd op een ongebalanceerde splitterboom-architectuur, die een gunstig evenwicht biedt tussen schaalbaarheid, optisch verlies en circuitcomplexiteit. Het microscoopbeeld van de gefabriceerde schakelingen wordt weergegeven in Fig. 1.

De gefabriceerde demonstratoren realiseren bundelsturing over een gezichtsveld van $15° \times 7.2°$ bij een golflengtebereik van 1500 nm tot 1600 nm. De continue DOPA levert een resolutie van 16×25 pixels, terwijl de gepixelde versie 4×25 pixels bereikt binnen hetzelfde bereik. De overeenkomstige resultaten van de bundelsturing voor de continue en gepixelde apparaten worden respectievelijk getoond in Fig. 2 en Fig. 3. De gepixelde DOPA vertoont een sterkere onderdrukking van zijlobben en achtergrondruis, wat wijst op een verbeterde bundelkwaliteit en minder fasefouten.

Over het geheel genomen benadrukken deze resultaten de voordelen van de gepixelde DOPA-architectuur. Door discretisatie in het verdelingsnetwerk te introduceren, biedt het ontwerp een betere controle over de bundelkarakteristieken,

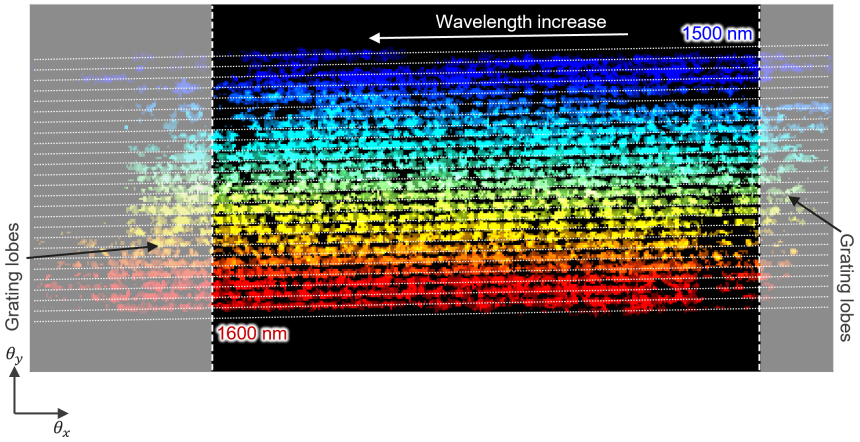

Figuur 2: Een samengesteld verre-veldbeeld van de 2D-bundelsturingsresultaten van de continue DOPA. Het beeld is gegenereerd uit een golflengtesweep van 1500 nm *tot* 1600 nm *met een resolutie van* 0.1 nm*, en beslaat een gezichtsveld (FoV) van* 15°×7.2°*.*

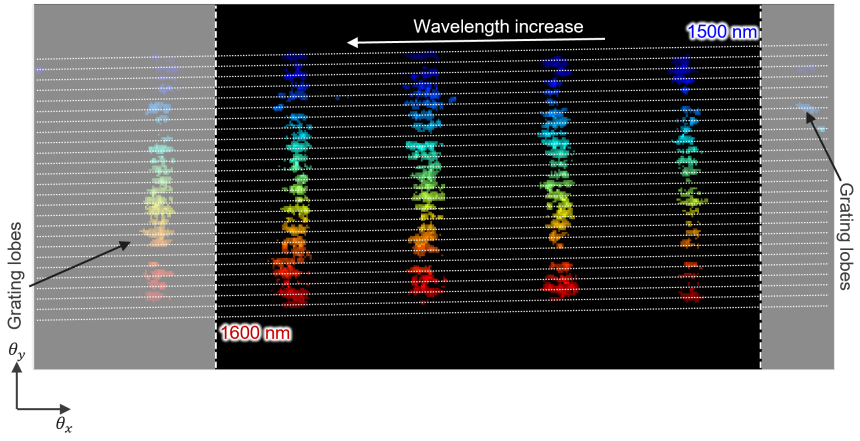

Figuur 3: Een samengesteld verre-veldbeeld van de 2D-bundelsturingsresultaten van de gepixelde DOPA. Het beeld is gegenereerd uit een golflengtesweep van 1500 nm *tot* 1600 nm*, bemonsterd op de golflengten van constructieve interferentie.*

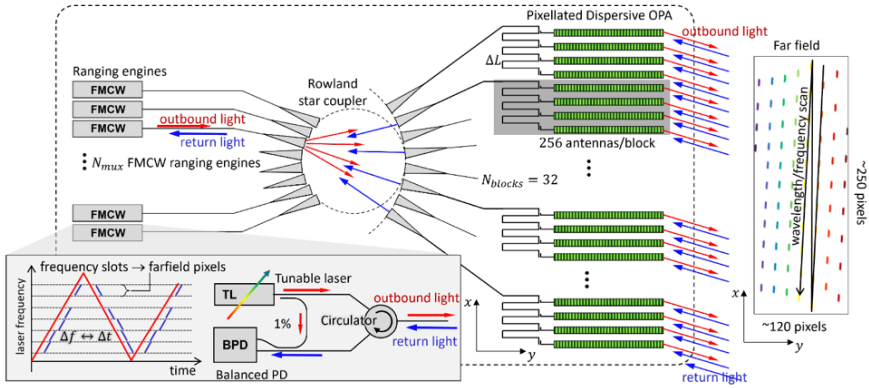

Figuur 4: Bundelsturing en FMCW-afstandsbepaling met één enkele golflengtevariabele, in een systeem dat een 2D-gepixelde DOPA-bundelscanner met gemultiplexte FMCW-afstandsbepalingsmodules integreert.

terwijl het een praktische schaalbaarheid en een haalbaar aantal pixels behoudt voor grootschalige DOPA-implementaties.

4 Bundelsturing en FMCW-afstandsbepaling met één enkele golflengtevariabele

De volgende stap is het combineren van bundelsturing en afstandsbepaling tot een volledig LiDAR-systeem. In een FMCW-LiDAR wordt de laserfrequentie continu gemoduleerd in een lineaire verschuivende afstemming. Een fractie van het lasersignaal wordt gebruikt als lokale oscillator voor coherente detectie, terwijl de rest in de vrije ruimte wordt uitgezonden. Wanneer het signaal door een object wordt gereflecteerd en in de ontvanger wordt gekoppeld, wordt het ontvangen signaal op de fotodetector gemengd met het lokale oscillatorsignaal, waardoor een zwevingsfrequentie ontstaat. Deze zwevingsfrequentie is recht evenredig met de heen-en-terugvertragingstijd van het gereflecteerde signaal.

Wanneer dit principe wordt gecombineerd met een DOPA, maakt de lasersweep niet alleen afstandsbepaling mogelijk, maar zorgt deze ook vanzelf voor golflengte-afhankelijke bundelsturing. Terwijl de laserfrequentie verandert, scant de uitgangsbundel in de tijd over het verre veld, waarbij elke uitgezonden golflengte wordt gekoppeld aan een specifieke stuurhoek en bijbehorende afstandsmeting.

Bovendien kunnen, door gebruik te maken van een gepixelde DOPA met een meerkanaals ster-koppelaar, meerdere afstembare lasers worden aangesloten, die elk een deel van het totale golflengtebereik bestrijken en zo een specifiek gedeelte

van het verre veld aanspreken. Deze configuratie maakt gelijktijdige belichting van meerdere pixels mogelijk en fungeert effectief als een golflengtemultiplexer.

In plaats van elke invoerpoort van de ster-koppelaar enkel te verbinden met een afstembare laser, kan elke poort worden gekoppeld aan een afzonderlijke FMCW-afstandsbepalingsmodule die werkt in een monostatische configuratie. Elke module bestrijkt een specifiek golflengte-deelbereik. Deze architectuur maakt parallelle pixelacquisitie mogelijk, verhoogt de integratietijd per pixel zonder de beeldsnelheid te verlagen, verbetert de signaal-ruisverhouding en benut de golflengteselectiviteit van DOPA's voor zowel transmissie als ontvangst. Een illustratie van het volledige systeem wordt weergegeven in Fig. 4.

5 Middelgrote gemultiplexte gepixelde DOPA met FMCW-afstandsbepaling

We presenteren het ontwerp van een volledig geïntegreerd fotonisch systeem voor FMCW-LiDAR, waarin golflengte-gemultiplexte gepixelde bundelsturing wordt gecombineerd met coherente afstandsbepaling in een monostatische configuratie. De chip integreert twee hoofdcircuits: een 512-kanaals gepixelde dispersieve optische faserarray (DOPA) voor bundelsturing en een afstandsbepalingscircuit met geïntegreerde germanium-fotodetectoren en transfer-geprinte halfgeleideroptische versterkers (SOA's) die dienstdoen als geïntegreerde lasers. Beide circuits zijn onderling verbonden via een meerkanaals ster-koppelaar, die het licht verdeelt over afzonderlijke DOPA-blokken en flexibele werking mogelijk maakt, zodat het systeem kan worden aangedreven door zowel geïntegreerde als externe lasers.

In de monostatische configuratie fungeert de gepixelde DOPA zowel als zender als ontvanger, wat de uitlijning en kalibratie vereenvoudigt. Het systeemontwerp volgt een bottom-up, modulaire aanpak, waarbij elk functioneel blok toegankelijk is via rooster-koppelaars om testen en foutopsporing te vergemakkelijken. Het ontwerp is gerealiseerd op imec's iSiPP50G-siliciumfotonicaplatform en maakt volledig gebruik van silicium-gebaseerde componenten, wat uitdagingen met zich meebrengt op het vlak van optische verliezen en fase-stabiliteit. Om de systeemcomplexiteit te beheersen en risico's te beperken, zijn voor de afzonderlijke subcircuits conservatieve ontwerpskeuzes gemaakt. De fotonische lay-out van het LiDAR-systeem wordt weergegeven in Fig. 5.

Hoewel een volledige experimentele demonstratie van het totale systeem buiten het bereik van dit proefschrift viel, legt dit ontwerp de basis voor de toekomstige realisatie van een volledig geïntegreerd, golflengte-afgestemd FMCW-LiDAR-op-een-chip-systeem, waarin bundelsturing en afstandsbepaling worden verenigd binnen één fotonische architectuur.

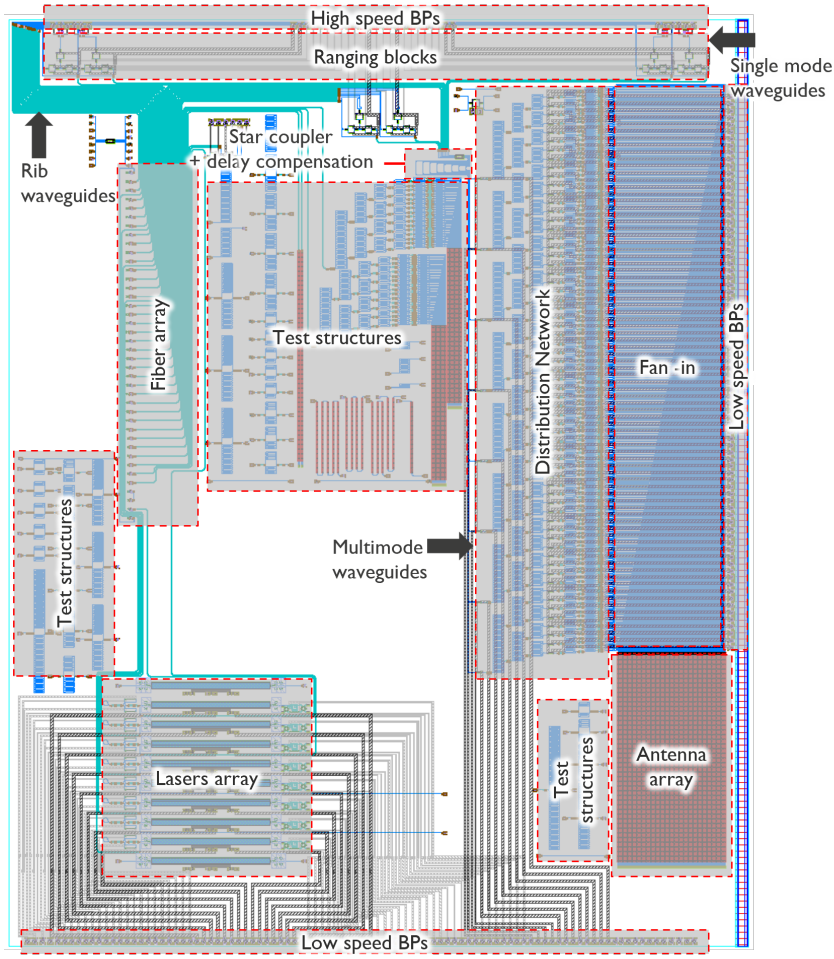

Figuur 5: De fotonische lay-out van het LiDAR-systeem.

6 Conclusie

Concluderend toont dit proefschrift aan dat golflengte-gestuurde gepixelde DOPA's een haalbare benadering vormen voor de realisatie van geïntegreerde FMCW-LiDAR-systemen. Het werk identificeert tevens belangrijke technologische uitdagingen, met name die verband houden met fasefouten en hun correctie. Door bundelsturing en afstandsbepaling te integreren binnen één enkele golflengte-afgestemde fotonische architectuur, legt dit onderzoek de basis voor compacte en kostenefficiënte solid-state LiDAR-platforms, met potentiële toepassingen die verder reiken dan automobiele detectie, zoals robotica en geavanceerde 3D-beeldvormingstechnologieën.

Summary

1 Introduction

Integrated photonics enables compact, scalable, and energy-efficient optical systems by miniaturizing traditional bulk optical components onto a chip, significantly improving size, weight, and power (SWaP). Although its development was initially driven by optical communication, particularly in telecom and datacom, the field has since expanded into new domains such as computing, LiDAR, biomedical imaging, and environmental sensing.

At its core, integrated photonics operates across several hierarchical layers. At the component level, it encompasses devices for light generation, modulation, routing, and detection. When these components are interconnected through optical waveguides, they form photonic integrated circuits (PICs) capable of performing advanced functions such as coherent detection and optical beam steering. Scaling these circuits into full photonic systems introduces additional challenges, including packaging, thermal management, and fabrication variability, all of which impact device yield and performance.

Within this broader context, the automotive industry has played a pivotal role in advancing solid-state long-range LiDAR systems, which serve as a key component of sensor fusion in Advanced Driver-Assistance Systems (ADAS). The primary objective of a LiDAR system is to reconstruct a three-dimensional point cloud of the surrounding environment by combining two fundamental functions: illumination and ranging. This is achieved by illuminating the scene through a transmitter, and whenever the transmitted optical signal encounter an object, it reflects back into the receiver. The receiver measures the distance to objects by determining the time delay between the emitted signal and the back-scattered light returned from the object. In this thesis, optical beam steering serves as the illumination mechanism, and frequency-modulated continuous-wave (FMCW) ranging is employed for distance measurement.

The research presented in this thesis operates at the intersection of photonic circuit and system-level design, exploring architectures that unify these two LiDAR functions. By exploiting wavelength tuning, the same mechanism can simultaneously enable beam steering and distance ranging, laying the groundwork

for a fully integrated LiDAR system governed by a single wavelength variable.

2 Dispersive Optical phased arrays

An optical phased array consists of multiple antennas arranged in one or two dimensions, where the relative phase and amplitude of the signals feeding each antenna determine the far field radiation pattern. In integrated photonics, long waveguide gratings can act as optical antennas. When arranged uniformly and excited with a fixed phase increment, they produce a collimated far field beam whose direction depends on that phase increment, enabling non-mechanical beam steering through electronic or optical phase control.

In this work, beam steering is achieved solely through laser wavelength tuning, eliminating the need for active phase shifters. By introducing fixed path length differences between the antennas through delay lines, the relative phase becomes wavelength-dependent, and beam steering is achieved in one direction. In the other direction, beam steering is achieved by long waveguide gratings, which have wavelength dependent emission angle, following the gratings dispersion. This principle defines the dispersive optical phased array (DOPA), where each wavelength corresponds to a distinct far field direction, enabling continuous wavelength-based scanning.

However, these continuous DOPAs offers face several scaling challenges, including large footprint, high insertion losses, and accumulated phase errors, primarily arising from the size of the optical distribution network. This prompts the exploration of solutions to reduce the size of the distribution network, while meeting performance requirements.

In this thesis, the pixelated DOPA concept is proposed, where the distribution network is divided into smaller blocks, maintaining the same aperture as the continuous DOPA while decoupling the far field angular resolution from the beam divergence. Pixelated DOPAs shorten the overall delay length without compromising the field of view or beam divergence, thus offering a more compact and scalable solution for long-range projection. As the laser wavelength is swept, narrow beams are formed only at discrete operating wavelengths, each mapping to a specific far field point, resulting in a pixelated rather than continuous scanning pattern.

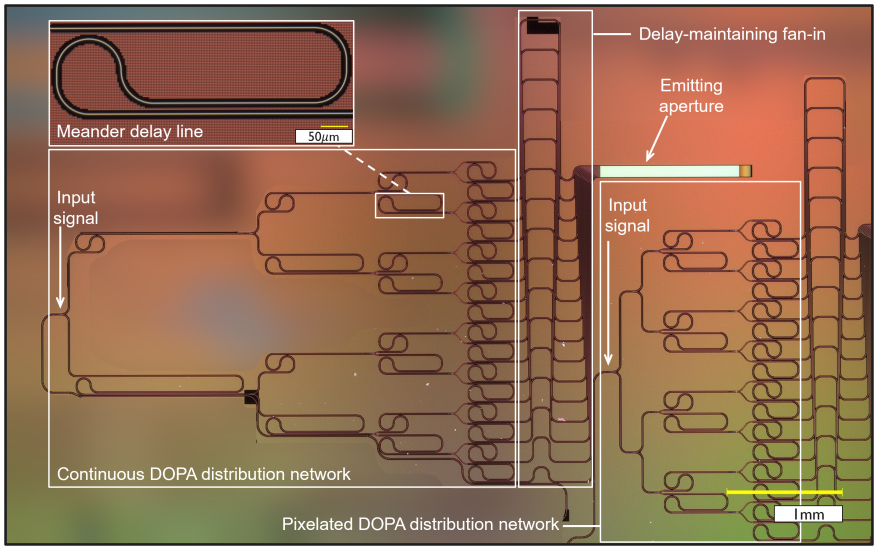

Figure 6: Microscope image showing the circuit of the continuous DOPA and the distribution network of the pixelated DOPA.

3 Experimental evaluation of continuous and pixelated DOPAs for 2D beam steering

We present two small-scale demonstrations of dispersive optical phased arrays (DOPAs) to benchmark the performance of the pixelated architecture against the conventional continuous design. Both implementations employ a novel light-distribution network based on an unbalanced splitter tree architecture, which provides a favorable balance between scalability, optical loss, and circuit complexity. The microscope image of the fabricated circuits is shown in Fig. 6.

The fabricated demonstrators achieve beam scanning over a field of view of $15° \times 7.2°$ for a wavelength sweep from 1500 nm to 1600 nm. The continuous DOPA produces a resolution of 16×25 pixels, while the pixelated version yields 4×25 pixels within the same range. The corresponding beam steering results for the continuous and pixelated devices are shown in Fig. 7 and Fig. 8, respectively. The pixelated DOPA demonstrates superior suppression of sidelobes and background noise, reflecting improved beam quality and reduced phase errors.

Overall, these results highlight the advantages of the pixelated DOPA architecture. By introducing discretization into the distribution network, the design offers enhanced control over beam characteristics while maintaining practical scalability and pixel counts for larger DOPA implementations.

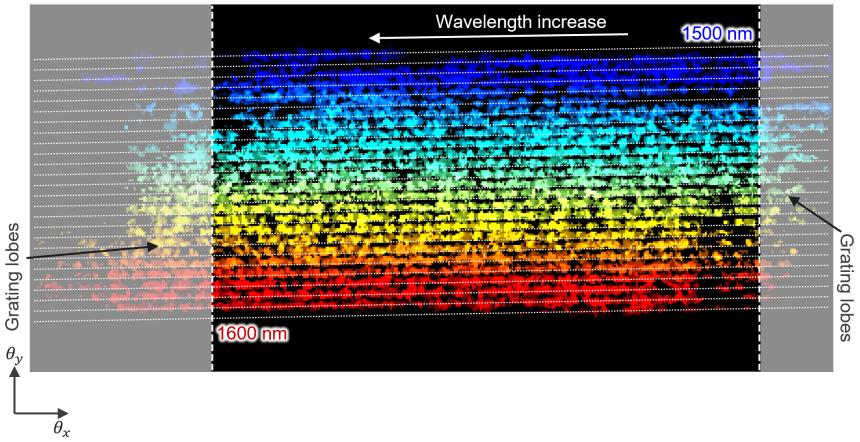

Figure 7: A composite far field image of the 2D beam steering results of the continuous DOPA. The image is generated from a wavelength sweep ranging from 1500 nm *to* 1600 nm *with a resolution of* 0.1 nm*, covering a field of view (FoV) of* 15°×7.2°.

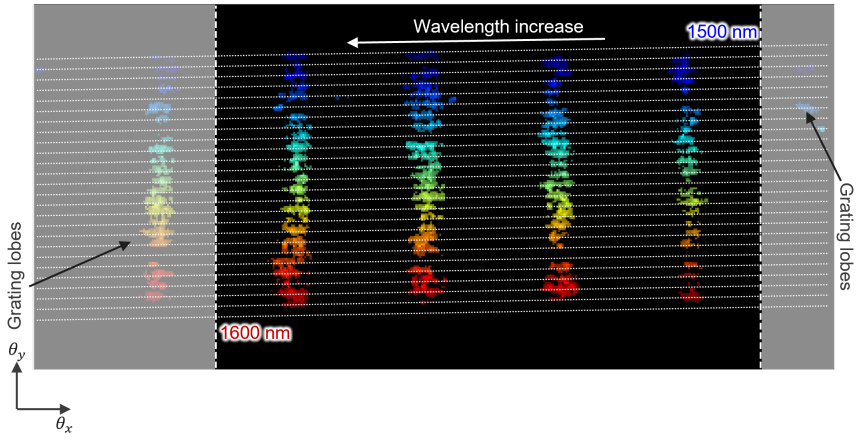

Figure 8: A composite far field image of the 2D beam steering results of the pixelated DOPA. The image is generated from a wavelength sweep ranging from 1500 nm *to* 1600 nm*, sampled at the constructive interference wavelengths.*

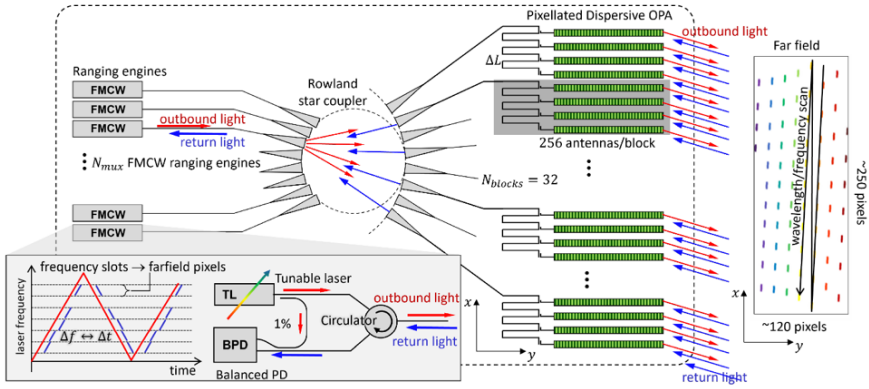

Figure 9: Beam steering and FMCW ranging with a single wavelength variable system incorporating a 2D pixelated DOPA beam scanner with multiplexed FMCW ranging engines.

4 Beam steering and FMCW ranging with a single wavelength variable

The next step is to combine beam steering and ranging into a full LiDAR system. In FMCW LiDAR, the laser frequency is continuously modulated in a linear sweep. A fraction of the laser signal is used as a local oscillator for coherent detection, while the rest is sent into free space. When the signal reflects from an object and coupled into the receiver, the received signal is mixed with the local oscillator signal at the photodetector, and a beat frequency is generated. The beat signal is directly proportional to the roundtrip delay time of the reflected signal.

When combined with a DOPA, the laser sweep not only enables ranging but also naturally produces wavelength-dependent beam steering. As the laser frequency changes, the output beam scans across the far field in time, linking the emitted wavelengths to specific steering angles and to range measurements.

Furthermore, by using a pixelated DOPA with a multi-input star coupler, multiple tunable lasers can be connected, each sweeping over a subset of the wavelength range and thereby addressing a distinct portion of the far field. This configuration allows simultaneous illumination of multiple pixels and effectively serves as a wavelength multiplexer.

Instead of connecting each input port of the star coupler to only a tunable laser, each input port can be connected to a separate FMCW ranging engine operating in a monostatic configuration. Each engine covers a specific wavelength sub-band. This architecture enables parallel pixel acquisition, increasing integration time per

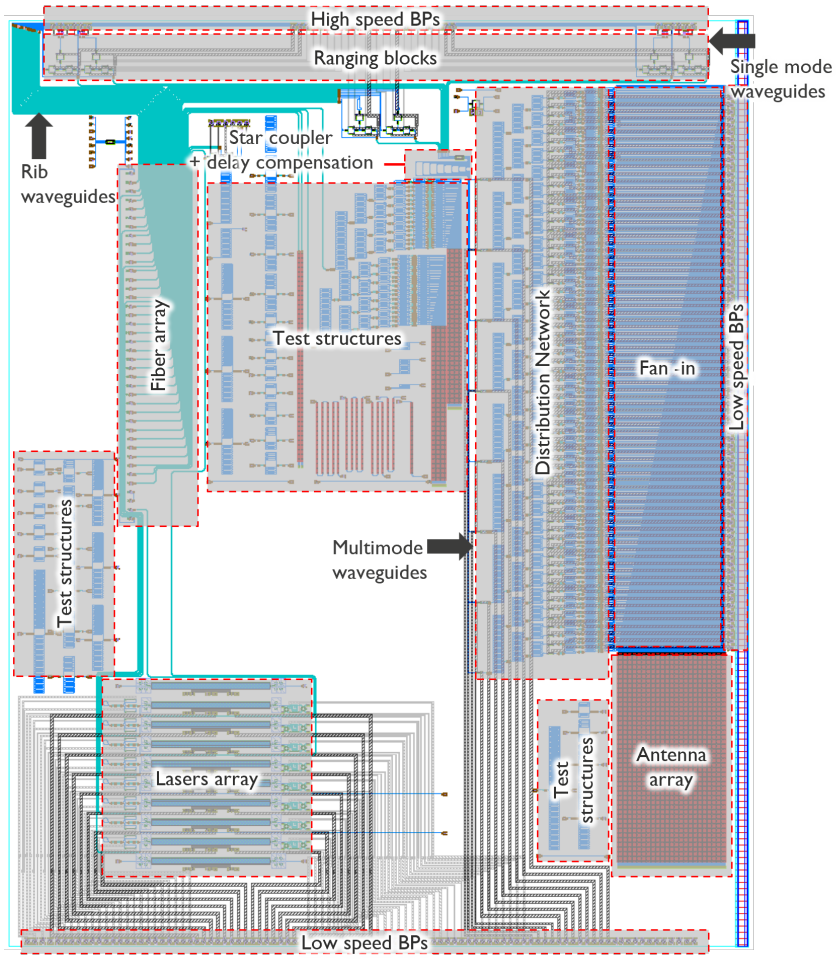

Figure 10: The photonic layout of the LiDAR system.

pixel without reducing frame rate, improving signal-to-noise ratio, and leveraging the wavelength selectivity of DOPAs for both transmission and reception. An illustration of the full system is shown in Fig. 9.

5 Medium-scale multiplexed pixelated DOPA with FMCW ranging

We present the design of a fully integrated photonic system for FMCW LiDAR, combining wavelength-multiplexed pixelated beam steering with coherent ranging in a monostatic configuration. The chip integrates two main circuits: a 512-channel pixelated dispersive optical phased array (DOPA) for beam steering and a ranging circuit featuring on-chip Germanium photodetectors and transfer-printed semiconductor optical amplifiers (SOAs) serving as integrated lasers. Both circuits are interconnected through a multi-input star coupler that distributes light to individual DOPA blocks and enables flexible operation, allowing the system to be driven either by on-chip or external lasers.

In a monostatic configuration, the pixelated DOPA acts as both transmitter and receiver, simplifying alignment and calibration. The overall system follows a bottom-up, modular design methodology, with each functional block accessible through grating couplers for straightforward testing and troubleshooting. Implemented on imec's iSiPP50G silicon photonics platform, the design relies entirely on silicon-based components, which presents challenges in optical loss and phase stability. To manage system complexity and mitigate risk, conservative design choices were made for individual subcircuits. The photonic layout of the LiDAR system is shown in Fig. 10.

While a complete experimental demonstration of full system operation was beyond the scope of this PhD work, this design establishes the foundation for future realization of a fully integrated, wavelength-tuned FMCW LiDAR-on-chip system, unifying beam steering and ranging within a single photonic architecture.

6 Conclusion

In conclusion, this thesis demonstrates that wavelength-steered pixelated DOPAs are a viable approach for realizing integrated FMCW LiDAR systems. The work also identifies key technological challenges, especially those associated with phase errors and their mitigation. By integrating both beam steering and ranging within a single wavelength-tuned photonic architecture, the research establishes a foundation for compact and cost-effective solid-state LiDAR platforms, with potential applications extending beyond automotive sensing to robotics and advanced 3D imaging technologies

1

Introduction

This thesis takes a step towards the realization of a fully integrated photonic Light Detection and Ranging (LiDAR) chip implemented on a silicon photonics platform. In the proposed system, the wavelength of the laser source is the key control variable for both beam steering and coherent detection. The emphasis of this work is placed on photonic circuit and system-level design rather than on the optimization of individual components or fabrication processes. It demonstrates how application-driven specifications shape the photonic design space and dictate the associated trade-offs.

The remainder of this introductory chapter outlines the current landscape of integrated photonics, establishing it as the technological framework of this thesis work. The chapter then introduces the relevant high level design configurations associated with solid-state LiDAR and positions the present work within this design space. Finally, the chapter defines the thesis objectives, provides an overview of its structure, and lists the publications in which portions of this work have been published.

1.1 Integrated photonics

Integrated photonics has emerged as a key technology for enabling scalable, high performance optical systems. A major advantage of integrated photonics lies in its ability to miniaturize the functionalities of traditional bulk optics into chip-scale devices, thereby substantially improving size, weight, and power consumption (SWaP) of these systems. The primary driver behind the innovation in integrated photonics has historically been optical communications, particularly in telecom and datacom markets [1, 2]. The relentless demand for higher data rates and energy-efficient interconnects has accelerated the development of high-bandwidth, low-footprint photonic devices. More recently, the technology is seeing rapid adoption in emerging domains such as computing and sensing, including LiDAR, biomedical imaging, and environmental monitoring [3]. At its core, the field can be organized around multiple layers of abstraction, as shown in Fig. 1.1.

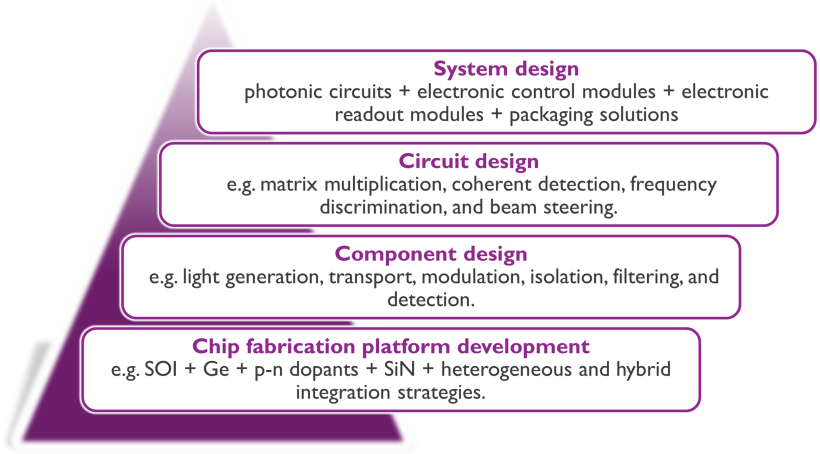

Figure 1.1: Layers of abstraction of integrated photonics.

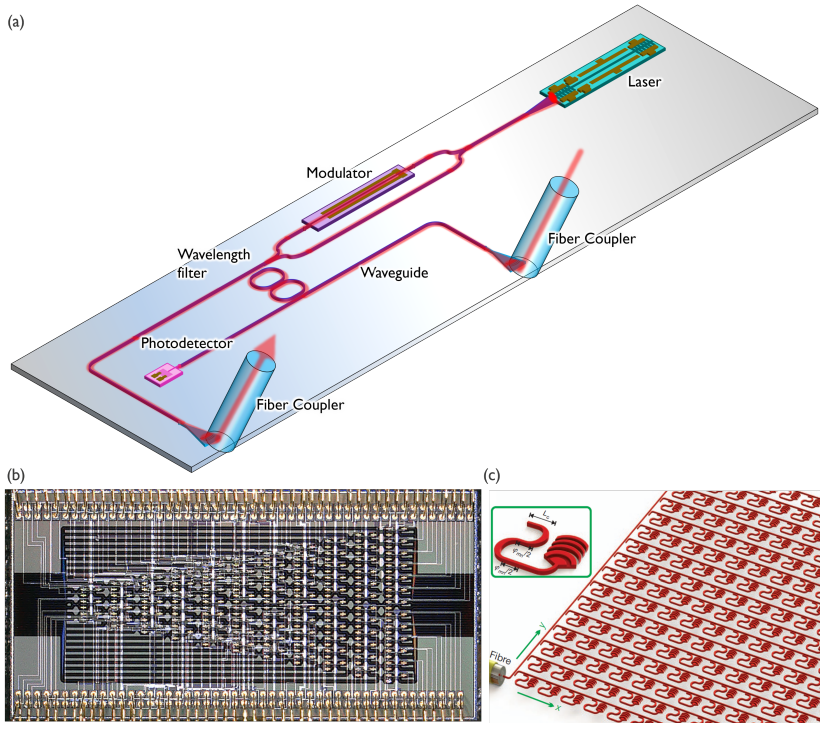

Figure 1.2: Photonic integrated circuits (PICs): (a) A PIC consists of optical components that are interconnected using optical waveguides, figure adapted from Prof. Wim Bogaerts slides; (b) an example of a PIC, which can perform matrix-vector product operation and is used for linear quantum optics, figure adapted from [4]; (c) an example of a PIC, which can perform optical beam steering, figure adapted from [5].

At the level of component design, integrated photonics comprises functional building blocks: individual components that perform essential optical functions. These include light generation, transport, modulation, isolation, filtering, and detection. When interconnected using optical waveguides, these building blocks form photonic integrated circuits (PICs), as shown in Fig. 1.2(a), that enable more complex optical functions, such as matrix multiplication, coherent detection, frequency discrimination and beam steering [6], examples of which are shown in Fig. 1.2(b,c). Moving up the hierarchy, photonic systems are realized by integrating these circuits with electronic control and readout modules, alongside packaging solutions that ensure mechanical robustness, thermal management, and optical/electrical interfacing. As circuits and systems scale, the challenges of design for manufacturability become increasingly critical. Fabrication imperfections, such as waveguide sidewall roughness or etch-depth variability, can accumulate across

large circuits, leading to performance deviations and yield degradation [7, 8].

This hierarchy is supported by a diverse set of material platforms, each suited for specific optical functions and performance requirements. Silicon photonics, introduced in 1985 [9], has gained traction due to its compatibility with CMOS foundries, offering cost-effective large-scale production, and electronic-photonic co-integration on a single chip [10, 11]. The high refractive index contrast of silicon platforms enables compact circuits with tight bends, allowing dense integration. However, silicon can not support active optoelectronic functions at telecom wavelengths such as efficient light emission and detection. This motivates the addition of many materials to the silicon-on-insulator (SOI) technology stack, such as p-n dopants for high speed modulators [12] and Germanium for high-speed photodetectors [13]. In addition, materials like silicon nitride (SiN) are being adopted for ultra low-loss waveguides, higher power handling, and lower phase errors [14, 15]. Furthermore, heterogeneous and hybrid integration strategies can be used for the optical functions associated with the non-native materials to silicon photonic platforms, such as gain media based on III-V semiconductors, electro-optic modulators based on Lithium Niobate (LNO) and Barium Titanate (BTO), and optical isolators based on magneto-optic materials [16–18].

Across all layers of abstraction, integrated photonics presents a rich and rapidly evolving research landscape. Progress in this field can be driven by advancements in device physics, circuit design methodologies, system integration, and scalable manufacturing. As the applications continue to diversify and performance targets become more demanding, integrated photonics will remain a cornerstone of next-generation communication, computation, and sensing technologies.

1.2 Light Detection and Ranging

LiDAR systems, in their simplest form, operate by transmitting a laser signal into free space, where it reflects or scatters off an object in the surrounding scene, and returns back into the receiver. By measuring the time delay between the emission and the reception of the light signal, i.e. time-of-flight (ToF), the system estimates the distance to the object, as shown in Fig 1.3. Capturing both direction and distance information of multiple points in the scene enables the reconstruction of a 3D point cloud of the surrounding. To achieve the LiDAR functionality, different design choices for the LiDAR configurations can be adopted to meet the desired performance metrics associated with the application of interest [19–21].

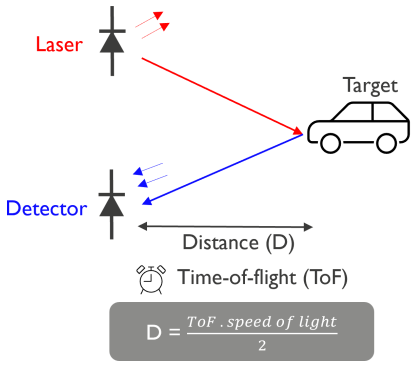

Figure 1.3: Basic concept of LiDAR operation.

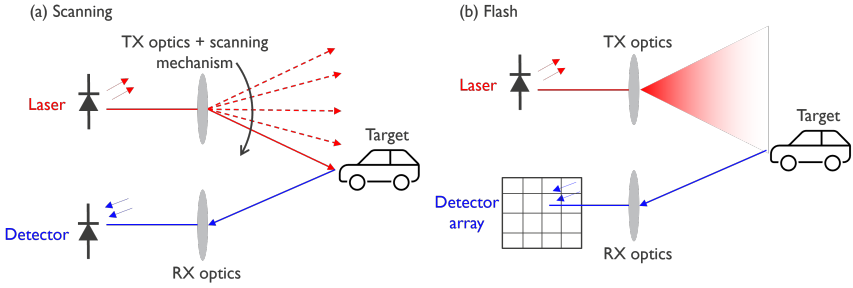

Figure 1.4: Scanning LiDAR vs Flash LiDAR.

1.2.1 Configurations

Recent advances in solid-state LiDAR aim to replace bulky mechanical scanners with integrated or chip-scale technologies to improve the reliability and scalability of the system while meeting the SWaP requirements. For chip-scale LiDAR, large number of design variations are available. A non-exhaustive list showing some of the relevant competing choices are listed below:

Illumination mechanism

The LiDAR transmitter (TX) can illuminate the scene by either a scanning or a flash mechanism, as shown in Fig. 1.4 (a) and (b), respectively. Scanning LiDAR emits a focused laser beam and measures distance in a single direction at a time, where beam steering mechanisms are used to sequentially address the points across the full scene. The return signal is detected by the receiver (RX) using a single-point photodetector. In contrast, flash LiDAR illuminates the entire scene simultaneously

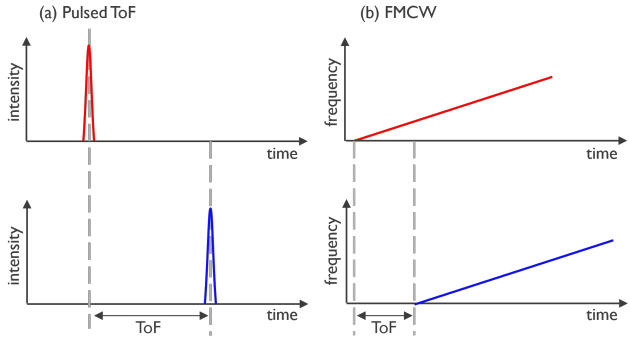

Figure 1.5: Pulsed ToF vs. FMCW.

similar to a camera flash. The reflected light from different points is then captured by a 2D detector array to reconstruct the scene. While flash LiDAR offers high frame rates thanks to its parallel detection, scanning LiDAR enables detection of distant or low-reflectivity objects with a given power budget, since it focuses all the power in one direction. Additionally, a hybrid approach could be adopted where the scanning and flash mechanisms are combined. For instance, a line scanning instead of pixel scanning can be used, and a 1D detector array can be used in the receiver to resolve the return signals from different directions along the line.

Ranging mechanism

In the LiDAR receiver, the roundtrip time of the captured back-scattered light from the target is calculated based on the time delay in its modulation pattern relative to the source light. The modulation can be based on amplitude modulation, for example in pulsed time-of-flight (ToF) or frequency modulation as in frequency-modulated continuous-wave (FMCW), as shown in Fig. 1.5. Pulsed ToF systems send a pulsed light signal, and the time delay can be calculated directly via an electronic clock. On the other hand, FMCW systems rely on measuring the frequency shift of a chirped signal using coherent detection, offering advantages such as high modulation bandwidth, Doppler velocity measurement and improved interference immunity. Further details about FMCW ranging will be discussed in chapter 4.

Transmitting and receiving aperture

Considering the scanning FMCW LiDAR, the transceiver can be in a bistatic or a monostatic configuration, as shown in Fig. 1.6. In the bistatic, the transmitter aperture is different from the receiver aperture, while in the monostatic, they share a common aperture. The bistatic configuration provides more design flexibility by

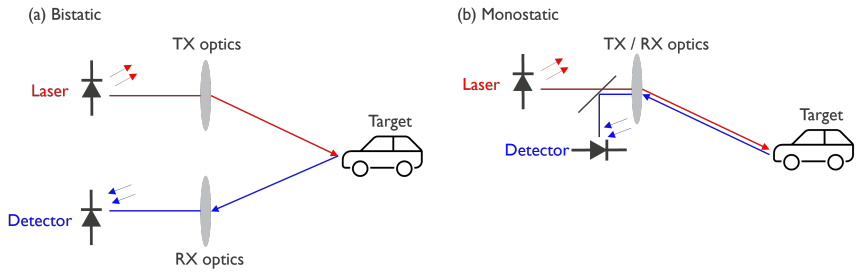

Figure 1.6: Bistatic configuration vs. Monostatic configuration.

allowing independent optimization of the transmitter and receiver. Additionally, since the receiver is spatially separated from the transmitter, it avoids detecting unwanted backreflections from the transmitter's optical elements, leading to a cleaner signal [22]. On the other hand, the monostatic configuration allows a more compact system and eliminates the need for optical alignment between transmitter and receiver, thereby simplifying the system design. It is worth noting that in radar systems, the term bistatic implies that the transmitter and the receiver are spaced far apart, while, in LiDAR the the transmitter and the receiver are next to each other but the apertures are separate. Further elaboration on these configurations is presented in chapter 4.

1.2.2 Performance metrics

The performance of a LiDAR system is characterized by several key metrics [20,24]. The specific application determines which of these metrics should be prioritized in the system design. In this work, the discussion about the performance metrics is framed within the demands of forward-looking long-range LiDAR for autonomous driving as the primary use case, as shown in Fig. 1.7. A visual illustration of the spatial performance metrics discussed in the following lines is shown in Fig. 1.8.

Field of view (FoV) $\Delta\theta$ specifies the angular extent over which the LiDAR system can scan and measure distance.

Angular resolution $\delta\theta$ refers to the minimum angle between two adjacent objects at which the LiDAR can distinguish them as separate targets.

Beam divergence describes how much the emitted laser beam spreads as it propagates. A narrower beam divergence results in longer detection ranges because more optical power is concentrated in a smaller area.

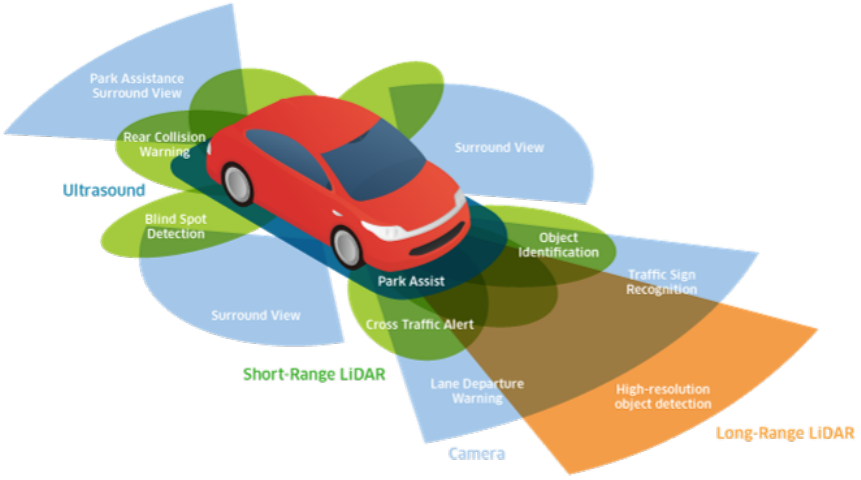

Figure 1.7: Automotive 3D sensing showing long-range LiDAR, figure from [23].

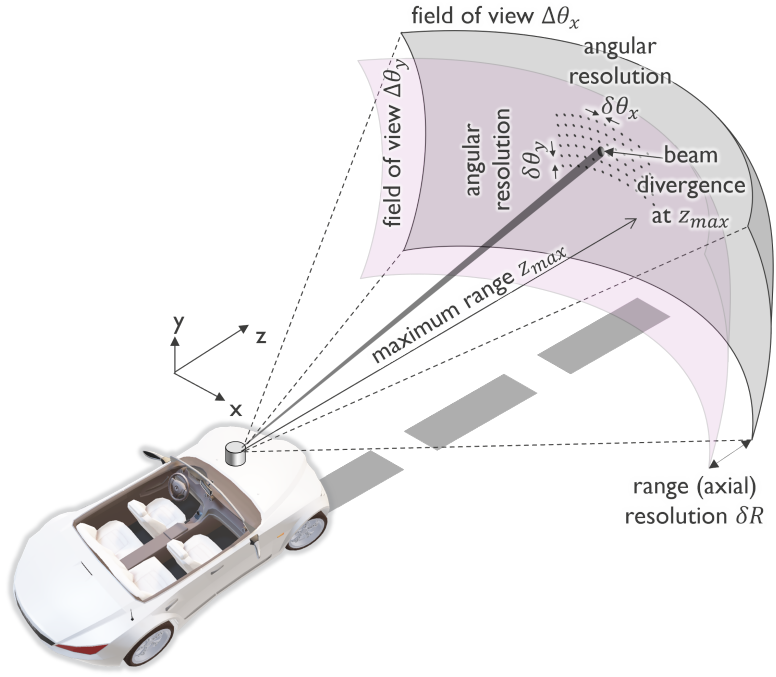

Figure 1.8: Sketch showing some performance metrics of a LiDAR system, figure adapted from [25].

Performance metric	Value
FoV	Horizontal: 45° - 90°, Vertical: 10° - 30°
Angular resolution	$\leq 0.1°$
Maximum range	200 m - 300 m
Range resolution	15 cm
Frame rate	10 Hz - 30 Hz

Table 1.1: Indicative performance specifications for automotive long-range forward-looking LiDAR.

Maximum range z_{max} is the maximum distance at which the LiDAR system can reliably detect and measure a target. It is determined by factors such as emitted optical power from the LiDAR system, and typical reflected power from the LiDAR target. In addition, it can be improved by improving the beam divergence in beam steering LiDAR.

Range (axial) resolution δR defines the system's ability to distinguish between closely spaced targets located at different distances along the same line of sight. It is governed by the bandwidth BW of the LiDAR system, as the range resolution $\delta R = \frac{c}{2BW}$, where c is the velocity of the wave. This implies that the wave's information content must change rapidly enough for the receiver to clearly distinguish reflections from two targets separated by a distance δR. Further details on the range resolution will be discussed in chapter 4.

Frame rate indicates how quickly the LiDAR system can generate a complete 3D point cloud. High frame rates are essential in dynamic environments. However, achieving high frame rates can involve trade-offs with other metrics, such as angular resolution.

Transmitted power directly affects the system's detection range. On the other hand, the maximum emitted power is constrained by eye safety regulations, particularly in consumer and automotive applications.

While final performance specifications for industry adoption in autonomous driving are still being defined, given the evolving and non-standardized nature of the field [26–28], table 1.1 presents representative values to guide our discussion.

1.3 Photonic scanning FMCW LiDAR engine

A set of design decisions were made to define the configuration explored in this thesis. Beam scanning was selected as the illumination method, while

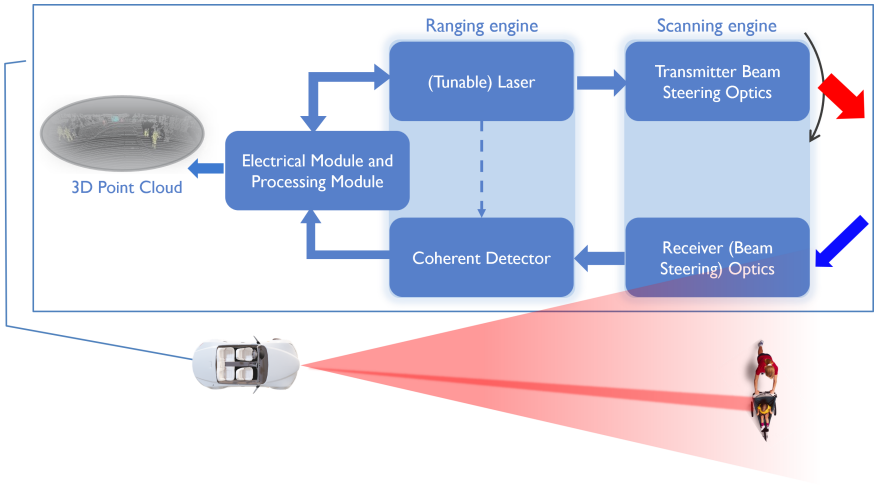

Figure 1.9: Photonic scanning FMCW LiDAR system block diagram. Note that the receiving optics could also accommodate beam steering, to ensure the collection of light only from the illuminated direction and reject light from other directions. In this case, the transmitter and the receiver share the same optics.

frequency-modulated continuous-wave (FMCW) coherent detection was chosen as the ranging mechanism. The discussion on the choice between bistatic and monostatic configurations is deferred to chapter 4 of the thesis. The optical C-band, centered around 1550 nm, is used due to its eye safety at higher power levels [29] and the widespread availability of photonic building blocks and mature technology platforms in this wavelength range. For clarity, the scanning FMCW LiDAR system can be conceptually divided into two functional subsystems: the scanning engine and the ranging engine, as shown in Fig. 1.9.

1.3.1 Scanning engine

For the automotive scanning LiDAR, a beam scanner with large FoV, high resolution, large projection range and low power consumption is desired, which is one of the key themes of this thesis. Currently, the two most promising approaches for beam steering in integrated photonics platforms are focal plane arrays (FPAs) and optical phased arrays (OPAs) [30–33].

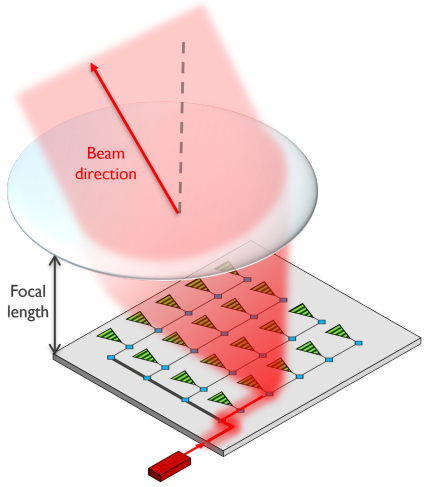

Figure 1.10: Schematic of the operation of focal plane arrays, figure adapted from Prof. Wim Bogaerts slides.

Focal plane arrays

FPAs [34–37] consist of a two-dimensional array of compact optical antennas (pixels), which are mapped onto far field directions using a lens, as shown in Fig. 1.10. The pixel array is positioned at the focal plane of the lens, which collimates the emitted light. An FPA is usually addressed with a switch matrix, illuminating one pixel at a time. Figure 1.11 shows some of the recent demonstrations of FPAs. Note that an FPA requires thickness [38], i.e. the focal distance of the lens, even if a flat-optics meta-lens is used. This is in contrast with OPAs, discussed in the next paragraph, which allow for a completely flat chip.

Optical phased arrays

OPAs are composed of an array of optical antennas, where precise control of the phase and amplitude of the antennas enables both beamforming and beam steering. Further details about the theory of OPAs are discussed in chapter 2.

A one-dimensional OPA can steer beams in a single angular direction, typically by employing phase shifters based on thermo-optic or MEMS mechanisms, as shown in Fig. 1.12(a). Extending beam steering to two dimensions can be achieved by using a 2D antenna array [5], as shown in Fig. 1.12(b); however, the increased control complexity and power consumption of 2D OPAs introduce significant challenges

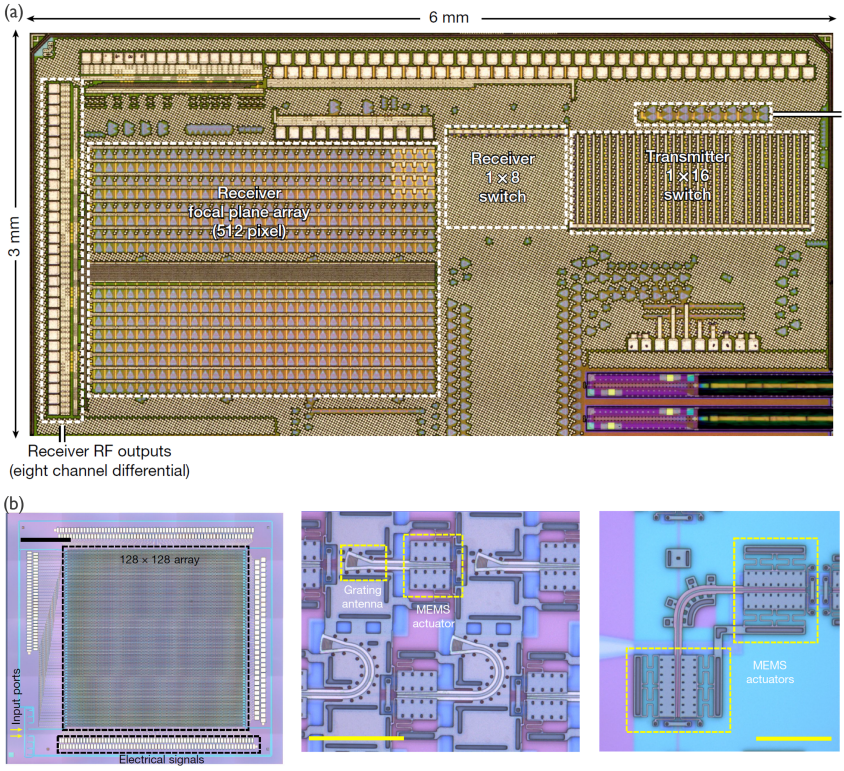

Figure 1.11: Recent demonstrations of FPAs: (a) FPA based on thermo-optic switches, figure from [34]; (b) FPA based on micro-electro-mechanical systems (MEMS) optical switches, figure from [36].

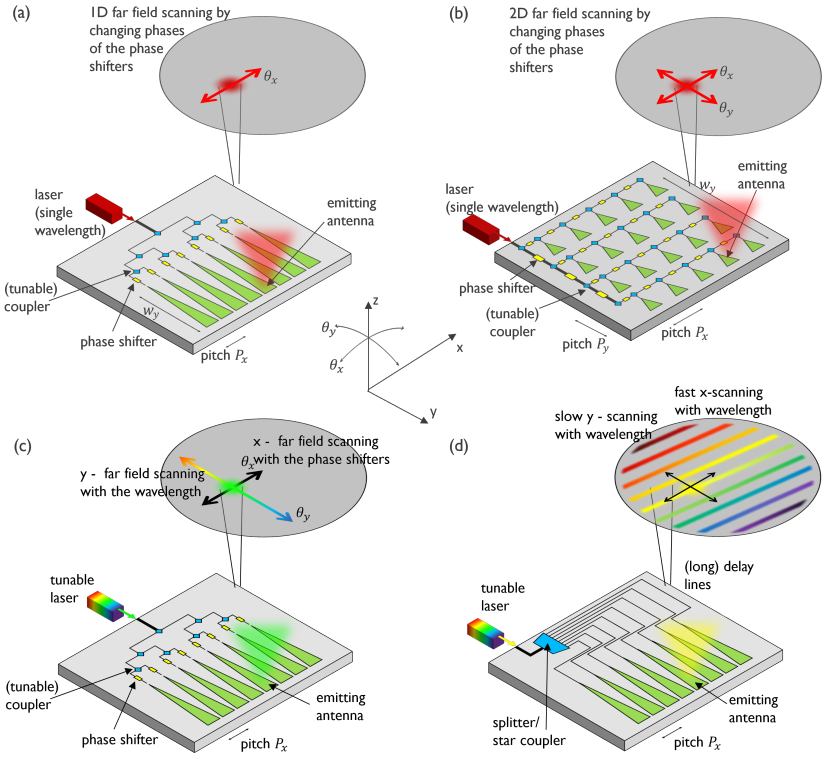

Figure 1.12: Schematics of OPA circuits: (a) 1D optical phased array, where beam steering is based on phase shifters; (b) 2D optical phased array, where beam steering is based on phase shifters; (c) 1D optical phased array, where beam steering is based on phase shifters in one direction, and on gratings dispersion in the other direction; (d) 1D optical phased array, where beam steering is based on delay lines dispersion in one direction, and on gratings dispersion in the other direction, figure from [25].

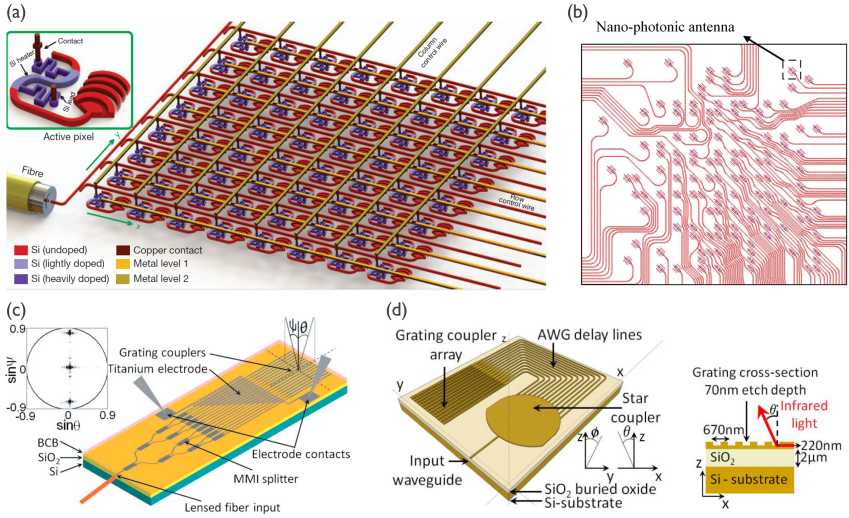

Figure 1.13: Various approaches to achieve 2D beam steering using optical phased arrays: (a) 2D optical phased array, figure from [5]; (b) 2D sparse optical phased array, figure from [39]; (c) 1D optical phased array, where beam steering in one direction, it is realized by means of thermo-optic phase shifters following the optical phased array principle, while in the other direction is realized by wavelength tuning, following the wavelength-dependent emission angle of grating couplers (grating dispersion), figure from [40]; (d) 1D optical phased array, where beam steering in both directions is achieved by tuning the laser wavelength. In one direction, beam steering is due to the optical differential delay of the delay lines, while in the other direction, it is due to the grating dispersion, figure from [41].

for scaling to the large apertures required in long-range LiDAR. To address these limitations, several strategies have been proposed. One approach is the use of sparse or aperiodic arrays [39, 42–44], which reduces the number of antennas while maintaining a large FoV and good beam divergence but at the cost of reduced power in the desired direction and increased background noise level. Another method involves employing a 1D array of long grating antennas, as shown in Fig. 1.12(c), where steering in one dimension is achieved by tuning the phase shifters of the OPA, while steering in the orthogonal dimension is accomplished through wavelength tuning of the source laser [40, 42, 45]. The wavelength-dependent emission angle of the gratings enables this second dimension of control.

This concept can be further extended by replacing the active phase shifters with passive differential delay lines [41, 46–49], as shown in Fig. 1.12(d). In such architectures, the phase difference between the antennas is determined by the differential optical path lengths and can be tuned by adjusting the laser wavelength. As a result, two-dimensional beam steering can be achieved solely through

wavelength control, and such architectures are referred to as dispersive optical phased arrays. However, dispersive OPAs comes with a set of scaling challenges associated with the delay distribution network [25]. The scaling of the differential delay lines increases the footprint, losses, and phase errors. That is why the current demonstrations of dispersive OPAs are limited in scale. Figure 1.13 shows an example of each of these implementation approaches.

1.3.2 Ranging engine

In FMCW LiDAR, as shown in Fig. 1.14, the transmitter signal is continuously frequency modulated using a sawtooth or triangular waveform. Part of the transmitter signal is tapped off to serve as a local oscillator (LO) signal, while the remainder is sent out off-chip through the transmitter optics. Upon back-scattering from a target into the receiver optics, the receiver signal is mixed with the LO signal at the photodetector, generating an RF beat signal. The frequency of the beat signal is proportional the frequency difference between the received signal and the LO signal, and in turn corresponds to the roundtrip time delay. The beat frequency can be estimated using digital signal processing techniques, such as a fast Fourier transform (FFT), enabling accurate distance estimation.

The wavelength tuning not only enables beam steering in the far field, as described above, but also serves as a candidate mechanism for FMCW ranging via a swept-source approach. This concept establishes the foundation for fully integrated LiDAR systems with a single wavelength variable operating both the scanning engine and the ranging engine. Further details of FMCW ranging and fully integrated LiDAR with a single wavelength variable system concept will be discussed in chapter 4 and 5.

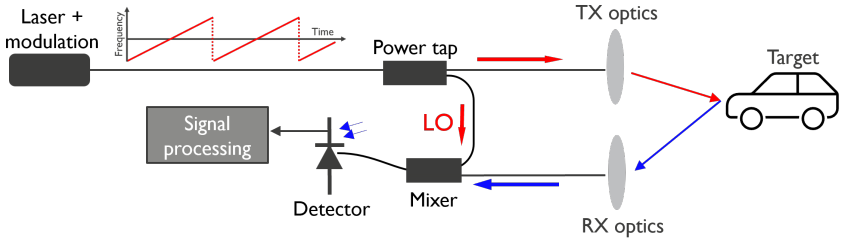

Figure 1.14: Schematic of FMCW ranging.

1.4 Objectives and thesis outline

The overarching goal of this thesis is to advance the development of a LiDAR system that is capable of beam steering and FMCW ranging with a single wavelength variable. The work presented herein is organized around two central themes. First, it explores the design of dispersive optical phased arrays architectures and their potential for scaling to large apertures suitable for long-range LiDAR. Second, it takes a step towards the realization of a fully integrated LiDAR system, in which the laser wavelength tuning is used to perform both beam steering and ranging functionalities. While a fully functional FMCW LiDAR demonstrator remains beyond the scope of this thesis, the groundwork laid here highlights the feasibility of integrating beam steering and ranging in a unified photonic architecture.

The remainder of this thesis is organized as follows:

- **Chapter 2** presents the basic concepts of (dispersive) optical phased arrays. The chapter also introduces the concept of pixelated dispersive optical phased arrays used in this thesis as a potential solution for the scaling bottleneck of dispersive optical phased arrays.
- **Chapter 3** focuses on the design details and the experimental results of a novel dispersive optical phased array architecture; that is the unbalanced splitter tree. The architecture is used in both the continuous and the pixelated variation of the dispersive optical phased arrays to evaluate the performance improvement for the pixelated approach.
- **Chapter 4** introduces the fundamental concepts of frequency-modulated continuous-wave (FMCW) LiDAR, followed by a discussion of the FMCW LiDAR link and its key design considerations. It then presents the concept of employing a single wavelength variable for both beam steering and FMCW ranging. Finally, a case study is provided to illustrate some of the trade-offs and implications of implementing such a system.
- **Chapter 5** covers the design of a medium-scale fully-integrated photonic LiDAR system. This system consists of wavelength multiplexed pixelated dispersive optical phased array with FMCW ranging block. The chapter then discusses the packaging and some preliminary measurements of the fabricated chip.
- **Chapter 6** concludes this thesis, summarizing the key findings and the potential future directions.

1.5 List of publications

This dissertation has led to the following publications.

1.5.1 International journals

1. **M. Kandil**, M. Prost, J. Kjellman, W. Bogaerts, M. Dahlem, "Experimental evaluation of continuous and pixelated dispersive optical phased arrays for 2D beam steering,"*Photonics Research Journal* (2025)

1.5.2 International conferences

1. **M. Kandil**, M. Prost, A. Lebanov, J.O. Kjellman, W. Bogaerts, M. Dahlem, "Experimental Evaluation of Passive 2D Optical Beam Scanners for FMCW LiDAR Applications," *European Conference on Optical Communication (ECOC),* Frankfurt, p.W1F.3 (2024)

2. **M. Kandil**, M. Prost, A. Lebanov, J.O. Kjellman, W. Bogaerts, M. Dahlem, "Passive 2D optical beam scanner: trade-off between angular resolution and sidelobe suppression," *IEEE Photonics Conference (IPC),* Italy, p.TuE2.3 (2024)

3. **M. Kandil**, T.D. Kongnyuy, M. Prost, D. Carbajal, S.S. Saseendran, J. Kjellman, G. Keulemans, W. Bogaerts, M. Dahlem, "Optical Hybrids using 3×3 and 4×4 MMIs with Low Phase Errors at Wavelengths around 850 nm," *IEEE Photonics Conference (IPC),* Italy, p.WD3.3 (2024)

4. **M. Kandil**, M. Dahlem, W. Bogaerts, "System trade-offs in a swept source FMCW LiDAR with dispersive OPA beam steering," *SPIE Photonics West - OPTO **(invited)**,* United States, p.12890-43 (2024)

5. W. Bogaerts, **M. Kandil**, M.S. Dahlem, "Integrated Optical Beam Scanning and FMCW Ranging using Multiplexed Tunable Lasers," *IEEE Photonics Conference (IPC),* United States, Canada (2024)

1.5.3 National conferences

1. **M. Kandil**, F. Peyskens, M. Dahlem, W. Bogaerts, "Photonic Integrated Circuits for Long-Range Solid-State LiDAR Applications," *Faculty of Engineering and Architecture Research Symposium* 2022 (FEARS 2022)

2

Beam steering using optical phased arrays

The theory of phased arrays is well established in radio-frequency (RF) textbooks [50, 51] and underpins a wide range of applications such as radar and wireless communications. These applications often require antennas with high directivity, whereas the radiation pattern of a single antenna element is typically broad and exhibits low directivity. Achieving higher directivity generally demands increasing the effective aperture of the antenna. Rather than increasing the dimensions of single antenna element to expand its aperture, multiple elements can be arranged

in an array and excited with signals that incorporate controlled phase delays, this configuration constitutes a phased-array antenna.

Phased-array antennas are composed of multiple fixed antenna elements that are coherently fed and individually controlled to steer the beam electronically. This is achieved by applying variable phase shifts or time delays to each element, enabling the radiated beam to be directed toward specific angles in space without physically moving the array. In some systems, variable amplitude control is also employed to perform beam shaping in addition to steering. RF phased arrays are widely used in applications such as radar systems for air-traffic control and remote sensing [52] and wireless communication systems [53].

Similarly, optical phased arrays (OPAs) are a class of optical beamforming devices consisting of an array of optical antennas. By controlling the amplitude and phase of the input to each antenna element, OPAs can generate a narrow, steerable optical beam in the far field, achieving functionality analogous to their RF counterparts but at optical wavelengths.

This chapter introduces the working principle of OPAs and outlines the performance metrics that define their functionality within LiDAR. It goes on to describe 1D dispersive optical phased arrays to achieve 2D beam steering, and the possible architectures for the light distribution network. The concept of the pixelated dispersive optical phased array is then introduced as a possible solution to scale dispersive optical phased arrays to the large apertures required for long-range LiDAR. Finally, phase errors, inherent to any practical implementation, are discussed.

2.1 Optical phased arrays

The operation of an OPA relies on the interference in the far field of the light emitted from multiple coherent optical emitters arranged in a one-dimensional or a two-dimensional array. By introducing a controlled phase and amplitude to the emitters, the direction of the beam in the far field radiation can be steered. Consider a periodic 1D array of N_x antennas, where the elements are separated by a pitch p_x and all have the same radiation pattern, as shown in Fig. 2.1. The 1D far field radiation pattern of the array at wavelength λ_0 is given by the summation over all the elements as:

$$E(\theta) = f(\theta) \sum_{n=0}^{N_x-1} a_n \exp\left[-jnk_0 p_x \sin\theta + j\phi_n\right], \tag{2.1}$$

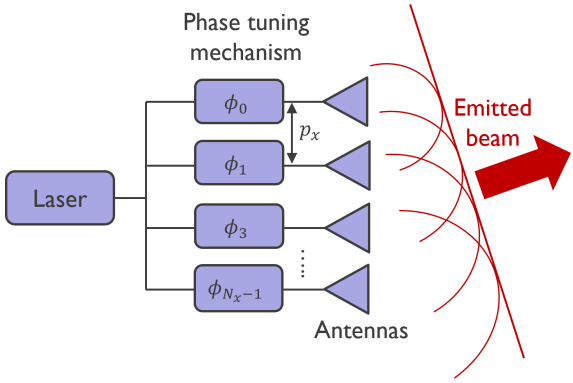

Figure 2.1: An optical phased array consisting of a 1D array of N_x antennas, with a pitch of p_x. By tuning the phase and amplitude of the light signal, a narrow beam can be formed and steered in the far field.

where a_n is the field amplitude of each element, which depends on the power profile input to the array, ϕ_n is the phase input at each element, and $k_0 = \frac{2\pi}{\lambda_0}$ is the free space wave number. $f(\theta)$ is the radiation pattern of the individual elements of the array; called the *element factor*. The far field pattern, Fig. 2.2(c) of the OPA is the product of the element factor, Fig. 2.2(b), and the summation term; which is called the *array factor*, Fig. 2.2(a). The element factor represents the radiation pattern of a single antenna element in the array. The array factor describes the interference pattern formed by the relative positions and phase shifts of the elements in the array, taking the individual antennas as isotropic point sources.

When all the antennas are in phase, one gets a narrow beam in the far field. In order to tilt the wavefront, i.e. scan the far field, a fixed phase difference $\Delta\phi$ should be introduced between the elements, i.e. $\phi_n = n\Delta\phi$.

The maxima of the array factor occur when:

$$\begin{aligned} k_0 p_x \sin\theta - \Delta\phi &= 2m\pi \\ \sin\theta &= (m + \frac{\Delta\phi}{2\pi})\frac{\lambda}{p_x}, \end{aligned} \tag{2.2}$$

where the array far field can have multiple peaks, i.e. orders indicated by the integer m. These orders are referred to as grating lobes. When the array pitch $p_x < \frac{\lambda}{2}$, there will be one order visible; that is the main lobe.

The separation between consecutive grating lobes of the array factor then follows:

$$\sin\theta_{m+1} - \sin\theta_m = \frac{\lambda}{p_x}. \tag{2.3}$$

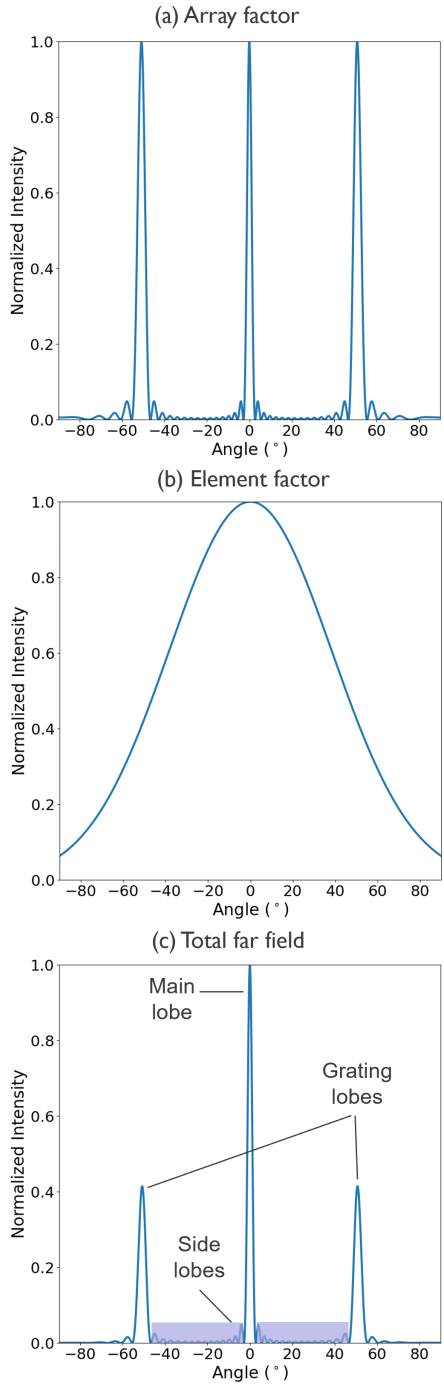

Figure 2.2: OPA far field: (a) array factor, where number of antennas $N_x = 16$, array pitch $p_x = 2\mu m$, wavelength $\lambda = 1.552\mu m$; (b) element factor; (c) total far field pattern, showing the main lobe, grating lobes and side lobes.

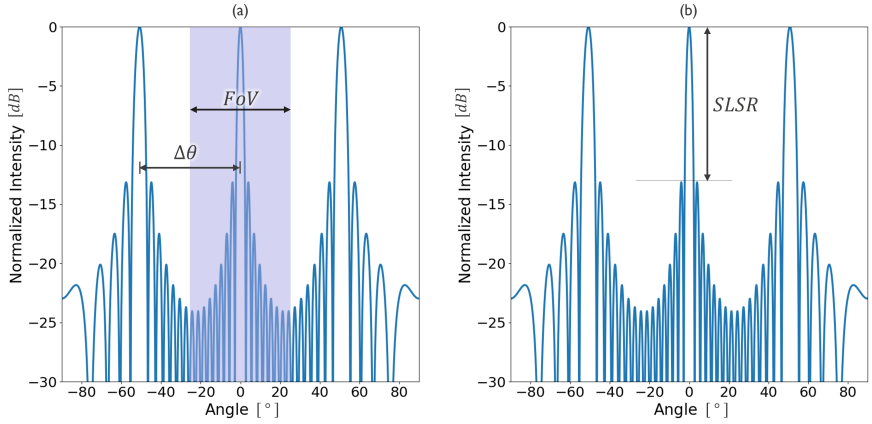

Figure 2.3: Array factor of an optical phased array showing: (a) the angular separation between two diffraction orders (grating lobes) as $\Delta\theta_{FSR}$. This separation is equivalent to the angular span over which the beam can be steered unambiguously, which is the field-of-view (FoV) of the optical phased array; (b) the theoretical side lobe suppression ratio of a uniform linear array being −13.26 dB.

Close to the perpendicular direction, the separation is approximated to

$$\Delta\theta \approx \arcsin\frac{\lambda}{p_x} \approx \frac{\lambda}{p_x}. \tag{2.4}$$

The value of this angular separation represents the steering range over which the beam can be steered unambiguously, that is the representation of the field-of-view (FoV) of the OPA, as shown in Fig. 2.3(a). Additionally, the angular beam divergence/width defined as the full width at half maximum is:

$$\Delta\theta_{FWHM} = \frac{0.886\lambda}{N_x p_x \cos\theta}, \tag{2.5}$$

whereas the far field beam divergence is inversely proportional to the aperture size, i.e. $\frac{1}{N_x p_x}$ factor. Additionally, beam divergence increases for larger off-axis angles, i.e. $\frac{1}{\cos\theta}$ factor. Close to the perpendicular, the beam divergence can be approximated to:

$$\Delta\theta_{FWHM} = \frac{\lambda}{N_x p_x}. \tag{2.6}$$

The approximations of equations 2.4 and 2.6 are useful as rules of thumb for OPAs design. Furthermore, considering that the separation between two consecutive resolvable points is at least the beam divergence, the number of resolvable points scale with the number of antennas:

$$\frac{\Delta\theta}{\Delta\theta_{FWHM}} \approx \frac{\frac{\lambda}{p_x}}{\frac{\lambda}{N_x p_x}} \approx N_x. \tag{2.7}$$

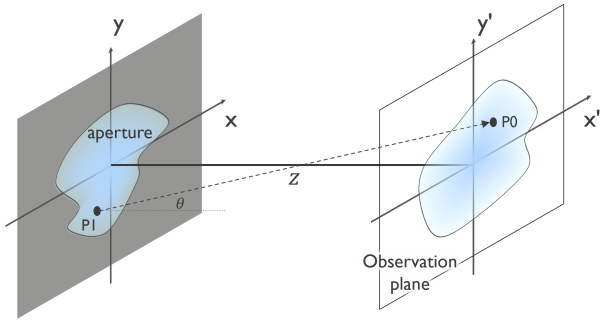

Figure 2.4: Diffraction geometry to illustrate the scalar diffraction theory, figure adapted from [54].

For a beam steering engine with a wide FoV with a narrow spot size, the OPA should have a large number of closely space antennas.

Another property of the OPA is the side lobe suppression ratio (SLSR), which is defined as the ratio between the main lobe and the most prominent side lobe, as shown in Fig. 2.3(b). In OPAs with uniform power distribution, also known as uniform linear arrays, the array factor takes the form of a sinc function, resulting in an SLSR with a theoretical value of −13.26 dB [50]. Further implications related to the SLSR is discussed in later chapters.

Diffraction theory formulation

Another toolbox to navigate the intuition of optical phased arrays is the scalar diffraction theory [54].

Considering the diffraction geometry in rectangular coordinates shown in Fig. 2.4, the diffracting aperture is positioned in the xy-plane and illuminated from left to right. The goal is to determine the resulting field in the $x'y'$-plane, which is parallel to the xy-plane, and is located at a normal distance z away from the xy-plane, where the z-axis passes through the origin of both planes.

Fresnel diffraction integral describes the diffraction of a scalar field U from the xy-plane to the $x'y'$-plane at a distance z:

$$U(x', y') = \frac{je^{-jkz}}{\lambda z} e^{-\frac{jk}{2z}(x'^2+y'^2)} \iint \{U(x, y)e^{-\frac{jk}{2z}(x^2+y^2)}\} e^{j\frac{2\pi}{\lambda z}(x.x'+y.y')} \, \mathrm{d}x\mathrm{d}y, \tag{2.8}$$

where λ is the wavelength of the propagating wave and k is the wave vector of the propagating wave. The integral can be recognized as the Fourier transform of the product of a complex field and a quadratic phase exponential. Wherever the Fresnel approximation is valid, the observer is at the *near field* of the aperture. When the

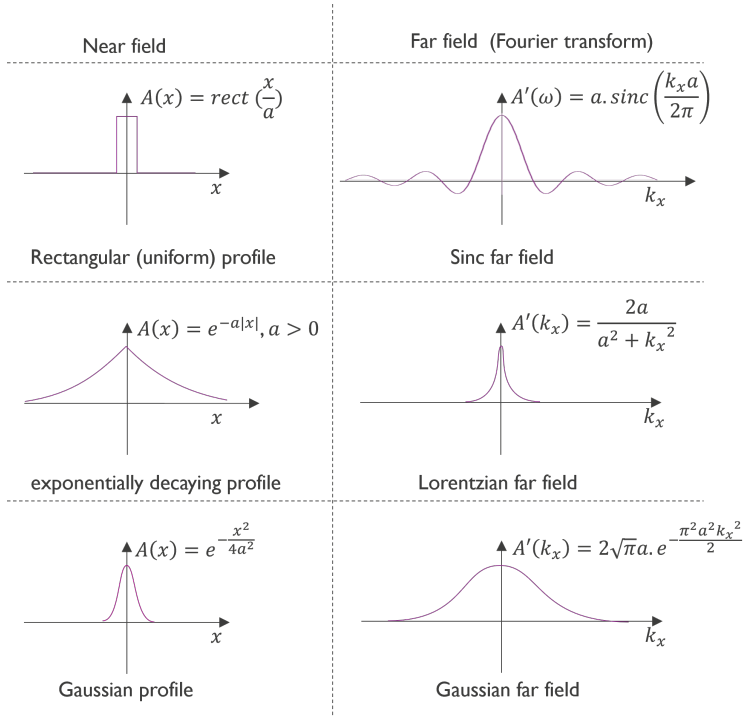

Figure 2.5: Fourier transform pairs.

distance z is far from the aperture such that:

$$z \gg \frac{k}{2}(x^2 + y^2), \tag{2.9}$$

the quadratic phase term is approximately unity over the aperture and we obtain the Fraunhofer diffraction formula:

$$U(x', y') = \frac{je^{-jkz}}{\lambda z} e^{-\frac{jk}{2z}(x'^2+y'^2)} \iint U(x, y) e^{j\frac{2\pi}{\lambda z}(x.x'+y.y')} \, \mathrm{d}x\mathrm{d}y, \tag{2.10}$$

where the observed field can be obtained directly from the Fourier transform of the aperture field distribution itself, evaluated at the spatial frequencies: $f_x = \frac{x'}{\lambda z}$, $f_y = \frac{y'}{\lambda z}$. And, the observer is said to be in the *far field*. Essentially, the Fourier decomposition of the field is a decomposition in plane waves with k-vectors:

$$k_x = 2\pi f_x, \;\; k_y = 2\pi f_y, \;\; and \;\; k_z = \sqrt{k^2 - k_x^2 - k_y^2}, \tag{2.11}$$

and:

$$k_x = k \sin\theta_x, \;\; and \;\; \sin\theta_x = \frac{x'}{z}, \tag{2.12}$$

where θ_x is the projection of the angle θ in the xz-plane, and the term $\sin\theta_x$ is equivalent to the term $\sin\theta$ in the 1D formulation of the OPA equation 2.2.

The Fourier transform (FT) properties can be applied to OPAs, as the far field radiation pattern is mathematically the FT of the aperture near field distribution. Figure 2.5 shows some important FT pairs, which can be used to match the far field power distribution to the aperture power distribution. An important observation is that the FT is a linear operation, consistent with the linear nature of the systems considered in this thesis. For OPAs and their numerical modeling, this linearity implies that the superposition of antenna fields in the near field directly corresponds to a superposition of their respective far field patterns. This property greatly simplifies the analysis and simulation of OPAs, as captured in Eq. 2.1.

2.2 2D beam steering with dispersive OPAs

Dispersion in photonic components refers to the wavelength dependence of the effective refractive index and group delay in optical waveguides and devices. While often considered a challenge in broadband systems, dispersion can also be harnessed as a design tool. Dispersive optical phased arrays leverage the wavelength dependence of photonic structures, such as gratings and waveguides, to

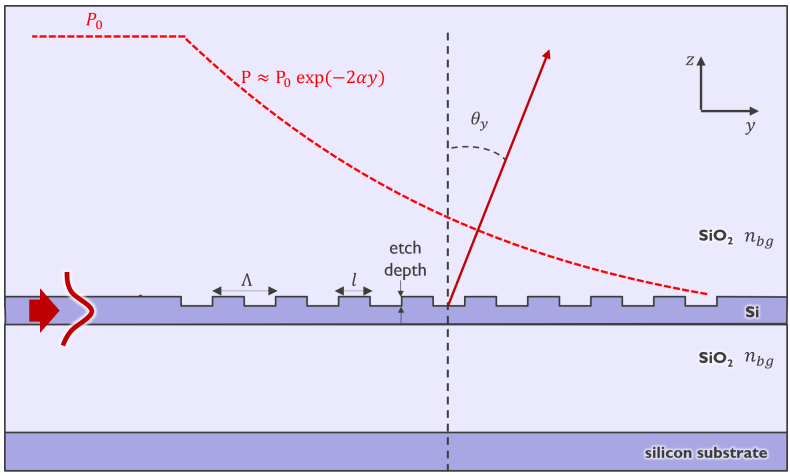

Figure 2.6: Cross-section of gratings with a uniform scattering strength. The grating power profile can then be approximated by an exponentially decaying function.

perform beam steering using a tunable laser source. This approach eliminates the need for multiple active phase shifters, potentially reducing complexity and power consumption. This section introduces the concept of dispersive optical phase arrays (DOPAs), their design parameters, and architectures.

2.2.1 Beam steering with gratings dispersion

Basic principle

Gratings are periodic structures that diffract light. The periodicity of the diffraction across the grating causes constructive interference to occur at specific angles. Gratings are fundamentally described by the Bragg condition that tells us the diffraction orders of a grating, and hence the direction of the diffracted light. The interested reader is referred to [55] for different theoretical frameworks for describing gratings such as Bragg theory, Floquet-Bloch theorem, and coupled mode theory.

Considering the waveguide-based gratings shown in Fig. 2.6, such structures are achieved by introducing a perturbation (forming a grating tooth) to optical waveguides, where the waveguide consists of a core layer with refractive index n_{wg}, sandwiched between a top cladding and a bottom cladding of different or similar material. Here, we take them as the same material of refractive index n_{bg}. The grating is characterized by its etch depth, period Λ, and duty cycle (also referred to

as fill factor) $= l/\Lambda$.

The gratings can also be described as an optical phased array, where the grating coupler is viewed as a periodic array of emitters, i.e. every grating tooth is an emitter. The differential phase between these emitters comes from the phase propagation of the guided mode as a function of the wavelength and the grating period. When the phase term is matched between the plane wave and the guided mode, the light is then coupled from the gratings to plane waves, i.e. light emission. A full derivation of this phase matching condition is presented in [56]. The guided mode has a decaying amplitude due to the light emission along the grating.

If to be considered of the second-order, the gratings allow near-vertical out-coupling of light off the photonic chip plane with an angle θ_y, which is described by the grating equation:

$$\sin\theta_y = \frac{\Lambda.n_{eff} - \lambda}{\Lambda.n_{bg}}, \tag{2.13}$$

where Λ is the grating period, n_{eff} is the grating effective index, and n_{bg} is the background index. From the grating equation, it can observed that grating-based antennas are inherently dispersive. In other words, their emission angle changes by changing the wavelength. The key definitions related to beam steering with waveguide gratings are described below.

Angular scanning rate

The angular scanning rate $\frac{d\theta_y}{d\lambda}$, also called grating tunability, is the rate of change of the grating emission angle with wavelength change. It can then be given by the derivative of the emission angle with respect to the wavelength:

$$\frac{d\theta_y}{d\lambda} \approx \frac{d\sin\theta_y}{d\lambda} = \frac{1}{n_{bg}}(\frac{dn_{eff}}{d\lambda} - \frac{1}{\Lambda}). \tag{2.14}$$

For this thesis, the direction where the steering is based on grating dispersion is denoted as the *y-axis*. The field of view $\Delta\theta_y$ is a function of the available wavelength tuning range $\Delta\lambda$, and the scan rate $\frac{d\theta_y}{d\lambda}$ as follows:

$$\Delta\theta_y = \frac{d\theta_y}{d\lambda} \,.\, \Delta\lambda. \tag{2.15}$$

Strength

When a uniform grating operates as an antenna or output coupler, the scattering strength is uniform along the gratings. Consequently, the optical power confined

in the guided mode decays in an approximately exponential profile along the propagation direction due to radiation/leakage through the grating [57]. The guided-mode power therefore follows:

$$P(y) = P_0 \exp(-2\alpha y), \tag{2.16}$$

where α denotes the strength of the grating. The corresponding grating length (coupling length/decay length) $L_{gr} = \frac{1}{2\alpha}$, i.e. the distance over which the guided power decays by a factor of $2e$ or the $\frac{1}{e}$ decay length of the diffracted field. A grating is described as *weak* when α is small and as *strong* when α is large. The antenna strength depends on the strength of the perturbation introduced by the grating elements. For instance, a shallow etch depth introduces a weak perturbation, allowing for longer grating length. In addition, if a Gaussian or a uniform emission profile is targeted, grating apodization is required, which means that the emission strength of the individual grating elements changes over the gratings length [58, 59]. One useful Fourier transform property here is that the far field beam shape of the uniform (non-apodized) grating along the y-axis is Lorentzian by recognizing it as the FT of the exponentially decaying profile along the grating, as shown in Fig. 2.5.

In order to use these gratings for beam steering, the far field beam divergence should be small to allow projection over long distance. Recalling Fourier transform basics, narrow beam in the far field requires having long gratings, and hence a weak waveguide gratings. Notably, one way of achieving long waveguide gratings is using an optical leaky fin antenna, which relies on the lateral leakage concept for light radiation rather than the periodic gratings [60]. However, this concept is not explored in this thesis.

Efficiency

The coupling efficiency quantifies how effectively the optical power is transferred between the waveguide mode and the external medium, such as an optical fiber or, in our case, free space.

In the context of our simulations, the efficiency is defined as the overall upward emission efficiency that is the fraction of the coupled light to a power detector above the gratings with respect to the power originally carried by the guided mode, as the ratio P_{up}/P_0.

The efficiency of grating couplers is influenced by the symmetry of the structure. For example, if the grating is vertically symmetric, the radiated power splits evenly upward and downward, restricting the upward coupling efficiency to less than 50%. In practice, many gratings exhibit near-vertical symmetry, because their etch depth is small compared to the waveguide thickness.

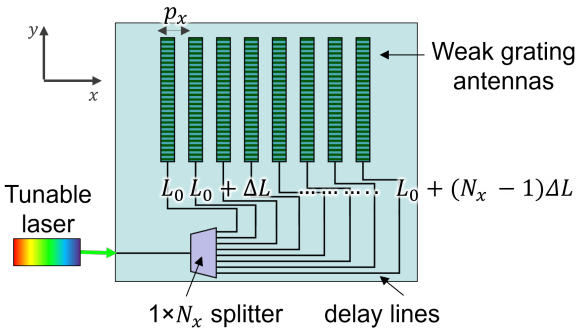

Figure 2.7: Optical phased array, where the phase between the antennas is achieved by delay lines, introducing differential delay of ΔL. Beam steering is achieved by tuning the laser wavelength, where the differential phase is a function of wavelength.

This symmetry constraint can be mitigated by deliberately breaking vertical symmetry, for example by using cladding of different refractive indices above and below the waveguide, or by incorporating a highly reflective substrate beneath the structure to direct more power upward, or by introducing a strong asymmetry in the grating design [59].

In brief, a grating design in the context of grating-based beam steering should co-optimize weak grating strength, with preferably apodization, high tunability and high efficiency.

2.2.2 Beam steering with delay lines

In the orthogonal direction, denoted as the x-*axis*, the phased array principle is the underlying beam steering mechanism. The long grating antennas are positioned in a periodic 1D array, where the differential phase is introduced by means of waveguide delay lines, as shown in Fig. 2.7. The waveguide delay lines should introduce a constant differential delay length ΔL between each two consecutive antennas. Consequently, the phase difference $\Delta\phi$ between each two adjacent antennas is a function of the wavelength λ:

$$\Delta\phi = 2\pi \frac{\Delta L \,.\, n_{eff}(\lambda)}{\lambda}, \tag{2.17}$$

where $n_{eff}(\lambda)$ is the effective refractive index of the delay line waveguide. For a given ΔL, sweeping the wavelength causes the differential phase delay $\Delta\phi$ to cycle from 0 to 2π, resulting in scanning the beam along the x-direction. This is analogous to the grating mechanism, except that the propagation length between consecutive emitters is now much larger than the optical wavelength.

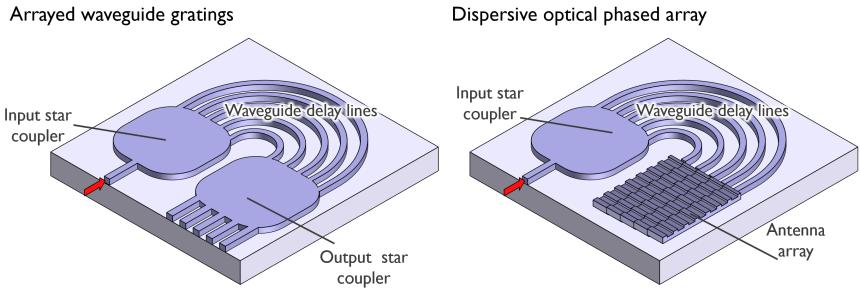

Figure 2.8: Dispersive optical phased arrays (DOPAs) are analogous to arrayed waveguide gratings (AWGs). While AWGs couple the light to the waveguide modes of the output channels via a star couple, DOPAs couple the light to free space via grating antennas, figure based on Prof. Wim Bogaerts slides.

In order to understand how to design for the differential delay length ΔL, we need to recall some of the theoretical basics of the design of PHASARs [61], or as it is commonly referred to as arrayed waveguide gratings (AWGs). In AWGs, the input light is coupled in plane to the waveguide modes of the output channels, while in dispersive OPAs, the input light is coupled off-chip to plane waves in free space, as shown in Fig. 2.8.

The free spectral range (FSR) refers to the wavelength spacing between two adjacent diffraction orders of the AWG, that overlap at the same output channel. This is similar to the separation between two successive grating lobes of the phased array, described by equation 2.3. In other words, the FSR of the AWG is the wavelength shift that causes the phase shift between successive waveguides to complete a full 2π cycle, thereby redirecting the light to the same point on the image plane. In the case of DOPAs, instead of moving the spot back to the same spatial point, the scanning in the y-direction, due to the grating dispersion, shifts the start point along the y-direction. The FSR, being the wavelength range required for one complete 2π phase cycle, is linked to the differential delay length by:

$$FSR_x \approx \frac{\lambda^2}{n_g \,.\, \Delta L}, \tag{2.18}$$

where n_g is the group index of the delay line waveguide. Note that the FSR is fundamentally in frequency units [61], but in photonics it is common to use the wavelength-based quantities rather than frequency-based quantities. Full derivation can be found in [62].

By substituting equation 2.17 in equation 2.2, the peaks of the array factor occur at:

$$\sin\theta_x = m\frac{\lambda}{p_x} + \frac{n_{eff}\Delta L}{p_x}, \tag{2.19}$$

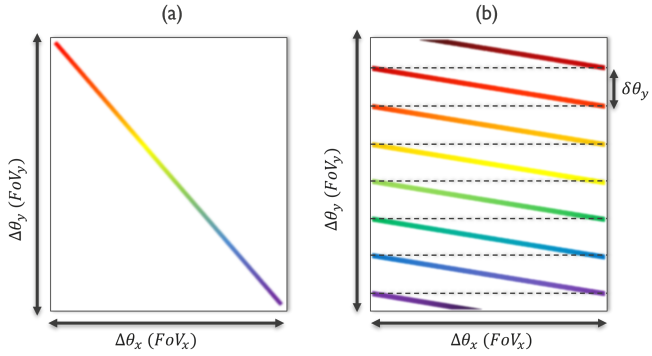

Figure 2.9: The concept of scan lines: (a) when the wavelength tuning range is equal to one FSR, there is one scan line within the FoV; (b) when the wavelength tuning range fits multiple FSRs, multiple scan lines fill the FoV.

where n_{eff} is the effective index of the delay line waveguides. Since ΔL is large, the grating order m is also large, and the scanning speed is:

$$\frac{d\theta_x}{d\lambda} \approx \frac{d\sin\theta_x}{d\lambda} = \frac{m}{p_x} + \frac{dn_{eff}}{d\lambda}\frac{\Delta L}{p_x}. \tag{2.20}$$

The scan rate can be also calculated as function of the FoV $\Delta\theta_x$ and the free spectral range as:

$$\frac{d\theta_x}{d\lambda} = \frac{\Delta\theta_x}{FSR_x}. \tag{2.21}$$

From the optical phased array description of the gratings, one can intuitively deduce that since ΔL is larger than the grating period Λ, the scan rate $\frac{d\theta}{d\lambda}$ along the x-direction is much faster than that along the y-direction. That is why the axis where scanning is due to delay lines is called the *fast axis*, while the axis where gratings dispersion is leveraged is called the *slow axis*.

Let's assume that the available wavelength tuning range $\Delta\lambda$ is equal to the FSR, the result is that one line scans over the full 2D FoV, as shown in Fig. 2.9(a). Increasing the differential delay lengthΔL, reduces the value of the FSR, allowing multiple 2π cycles for a given tuning range, as shown in Fig. 2.9(b). The number of scan lines N_y corresponds to the number of 2π cycles that can be achieved within the wavelength tuning range:

$$N_y = \frac{\Delta\lambda}{FSR_x}. \tag{2.22}$$

Alternatively, the number of scan lines is equivalent to the number of resolvable points along y-direction. The angular separation between each two consecutive resolvable points in the y-direction, or the sampling resolution $\delta\theta_y$, can be calculated

as:

$$\delta\theta_y = \frac{\Delta\theta_y}{N_y}. \tag{2.23}$$

In these DOPAs, each wavelength corresponds to a collimated beam at a specific far field angle. Consequently, when the laser wavelength is scanned, a narrow beam is continuously scanned over the field view of the OPA, hence it is referred to as a *continuous* DOPA.

2.2.3 Architectures

The differential delay can be introduced to the antennas via different architectures, where we take the total length of delay line waveguides as a first indicator of the scaling properties of these architectures. In the original demonstration of dispersive optical phased arrays [41], the differential delay was introduced by an AWG architecture. This architecture is conceptually straight-forward: the light is split over N_x channels using a star coupler or a splitter tree into waveguides with progressively increasing length, as shown in Fig. 2.10(a). The total length of the

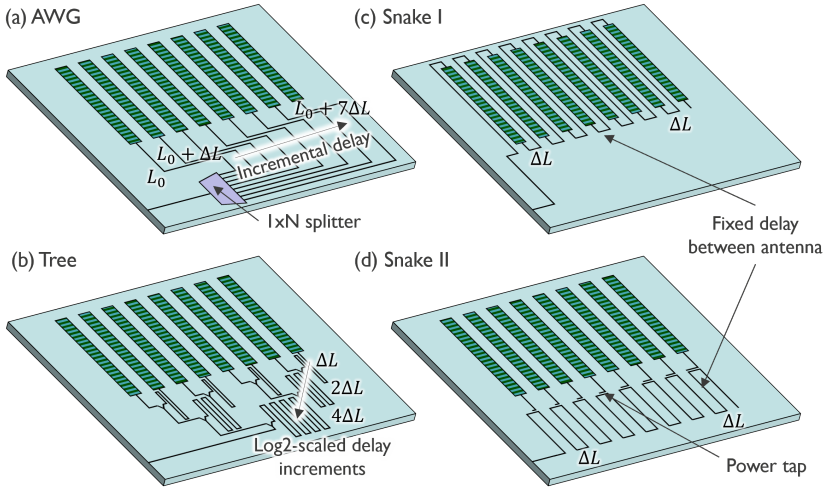

Figure 2.10: Different dispersive optical phased arrays architectures: (a) AWG: set of waveguides, each with a progressively increasing length by ΔL; (b) unbalanced splitter tree: introduces a delay in one arm of each splitter, with the delay in stage m equal to $2^m \Delta L$; (c) snake: design from [46], where delays are implemented using both the long gratings and the 'flyback' waveguides; (d) an alternative snake architecture from [63]: a bus waveguide distributes light, where a fraction of the light is tapped off to the antennas at regular intervals of ΔL, figure based on [63].

delay lines to achieve the differential delay scales with N_x^2, where:

$$L_{tot} = \frac{N_x(N_x - 1)}{2}.\Delta L. \tag{2.24}$$

The delay can be distributed through a snake-like topology, where the delay lines are in a meander/serpentine geometry. The light can possibly be fed to the antennas in two different ways; either by tapping off some of the light into the antennas at intervals of ΔL distance, Fig. 2.10(d), or by incorporating the antennas on the meanders at ΔL intervals and radiating the light off-chip directly, Fig. 2.10(c). In the first approach, the light can be tapped off using directional couplers with accurately controlled coupling ratios. At the first antennas along the light path, only a small fraction of power should be tapped to ensure sufficient light reaches the last antennas, where ideally a larger fraction of the power is tapped off so that all the remaining optical power is coupled to the antennas. This is similar to the apodization of the grating antennas described in section 2.2.1. In the second approach, the grating strength should vary from the first antennas to the last antennas to avoid coupling all the optical power off-chip in the beginning of the aperture. The total length of the delay lines to achieve the differential delay scales with N_x, where:

$$L_{tot} = N_x.\Delta L. \tag{2.25}$$

Finally, the delay can be distributed through an unbalanced splitter tree topology. At the output of each splitter, light signal is split into two sides; let's call these sides *south* and *north*. For the same side of every splitter, for example south, the light propagates through a delay line, while for the other side, the light does not propagate through a delay line. Progressing through the stages of the splitter tree, from the closest to the farthest from the antenna array, the delay lines get longer by a factor of $2^{(stage\ number)} \times \Delta L$. The total length of the delay lines to achieve the differential delay scales with $N_x.\log_2 N_x$, where:

$$L_{tot} = \frac{N_x.\log_2 N_x}{2}.\Delta L. \tag{2.26}$$

Further discussion on the architectures is presented in chapter 3. In this thesis, we will be mainly exploring the unbalanced splitter tree architecture.

2.3 2D beam steering with pixelated dispersive OPAs

The scaling behavior of the delay lines in the aforementioned architectures directly impacts the scalability of DOPAs in terms of three key criteria: footprint, optical

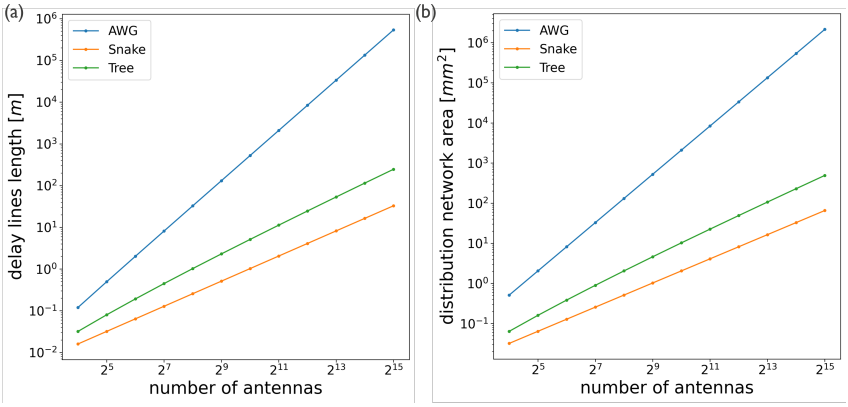

Figure 2.11: Scaling of the DOPA architectures as function of the number of antennas for a differential delay length $DeltaL$ =1 mm: (a) The total delay length for all antennas; (b) the area of the delay lines, assuming a 2 µm *waveguide spacing.*

insertion loss, and phase errors. To obtain an order of magnitude estimate of the relevant parameters, we consider the performance metrics summarized in Table 1.1.

To achieve a FoV of 45° along the x-axis (horizontal direction), an antenna pitch p_x of 2 µm is required, according to Eq. 2.4. Grating antennas in silicon typically exhibit a grating tunability (angular scanning rate) $\mathrm{d}\theta/\mathrm{d}\lambda$ of approximately 0.15 °/nm [41, 46, 47]. For a wavelength tuning range of 100 nm, this corresponds to a vertical FoV of about 15°, which is sufficient given the metrics in Table 1.1. To achieve an angular resolution of 0.1° in the vertical direction, $N_y = 150$ scan lines are required. Assuming a group index for silicon in the range 3.5–4.5 and using Eqs. 2.18 and 2.22, the required differential delay ΔL lies between 0.8 mm and 1 mm. For simplicity, we take $\Delta L = 1\,\mathrm{mm}$.

In addition, the Rayleigh range z_r of the emitted beam should match the maximum range of the LiDAR system. The beam waist w_0 is given by

$$z_r = \frac{\pi w_0^2}{\lambda}, \tag{2.27}$$

and the aperture size L_x must satisfy $L_x \geq 2w_0$. For a maximum range of 300 m, this yields a minimum aperture size of approximately 24 mm. With an antenna pitch of 2 µm, this corresponds to more than 12,000 antennas. In practice, the number of antennas required typically lies in the range 2^{13}–2^{14} antennas.

Taking into account the scaling properties of the architectures described in Section 2.2.3, the total delay line length scales as shown in Fig. 2.11(a). Based on this length, an optimistic estimate of the footprint of the distribution network for

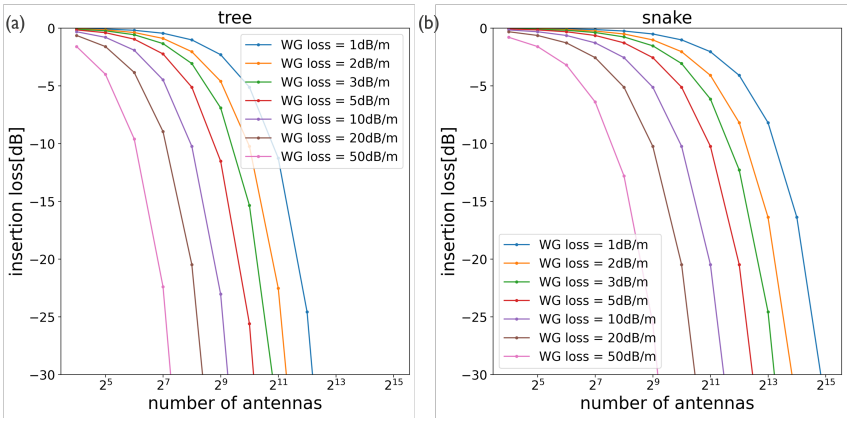

Figure 2.12: Scaling of the cumulative optical insertion losses of the delay lines of the DOPA architectures (excluding optical coupler losses) for a differential delay length $\Delta L = 1$ mm*: (a) tree; (b) snake.*

each topology is presented in Fig. 2.11(b). The results indicate that the AWG-based distribution network cannot fit within a full-field reticle, i.e., 625 mm^2 to 850 mm^2, whereas the snake and tree architectures may potentially do so. However, even for these latter two topologies, the optical insertion losses of the distribution network become a critical concern, as illustrated in Fig. 2.12. In particular, for large number of antennas, the losses rapidly become prohibitive unless waveguide propagation losses can be reduced below 3 dB/m. In submicron silicon waveguides, which are required here to achieve a tight waveguide spacing of 2 µm, practical propagation losses are typically one to two orders of magnitude higher. These limitations reflect current technological constraints. The impact of the distribution network insertion loss on overall LiDAR system performance is further discussed in Section 4.5. While parameters such as group index and grating tunability may vary across implementations, these estimates capture the correct order of magnitude. In summary, the large apertures required for long range LiDAR require few thousands of antennas, causing all considered architectures to violate at least one of the key scaling criteria under present technology constraints [25, 63]. In order to reduce the total length of the delay lines, the design constraints of continuous DOPAs are revisited, which led to the introduction of the pixelated DOPA concept.

2.3.1 Pixelated DOPAs working principle

The continuous DOPA is capable of steering a collimated beam to any direction along a far field scan line. However, practically, the number of resolvable spots , or pixels, equals the number of antennas, following equation 2.7, where the separation

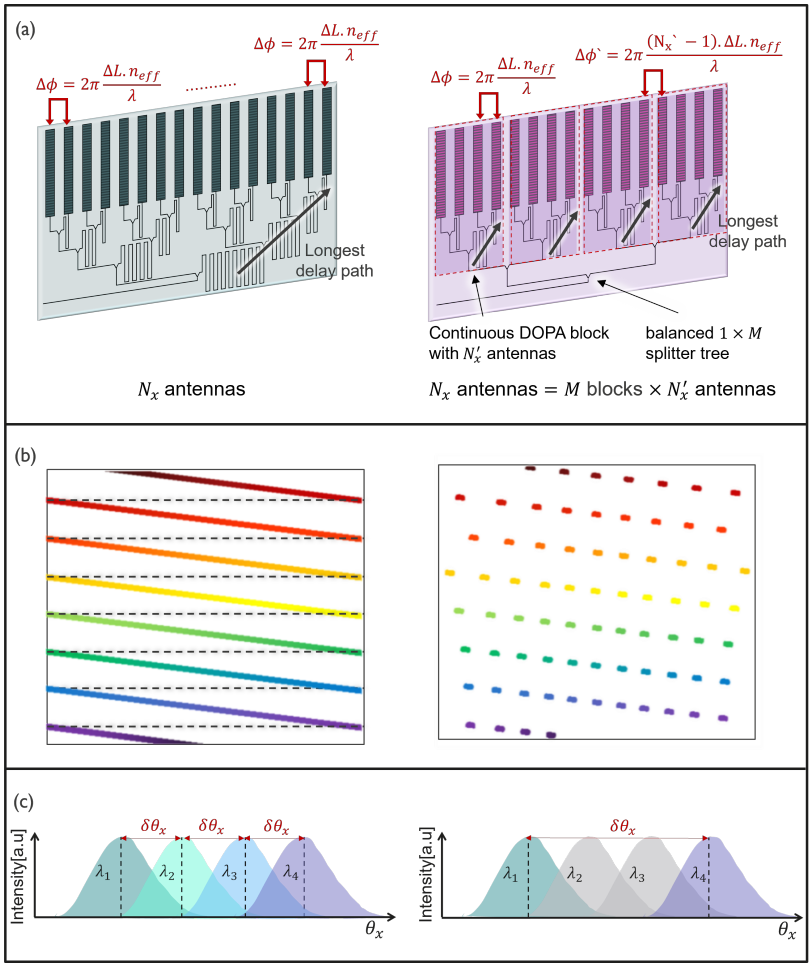

Figure 2.13: Continuous dispersive optical phased array (DOPA) vs. Pixelated DOPA: (a) The phase relation between all the antennas is maintained for all wavelengths in continuous DOPAs. On the other hand, the phase relation between the antenna are broken and is only maintained for specific wavelengths. The longest delay path in the pixelated DOPA is shorter than that of the equivalent continuous one; (b) Upon sweeping the laser wavelength, the far field is scanned continuously in the continuous DOPA, while, for the pixelated DOPA, a narrow beam occurs only for specific wavelengths; (c) The resolution of the continuous DOPA is higher than that of the equivalent pixelated DOPA. As the number of blocks increases, the resolution of the pixelated DOPA decreases.

between one resolvable point to the next equals the beam divergence $\Delta\theta_{FWHM,x}$. As a result, an unintended coupling arises between beam divergence and angular resolution. The beam divergence is typically specified such that the Rayleigh range of the aperture matches the maximum projection distance, ensuring a tightly focused beam at long range. However, in applications like long-range automotive LiDAR, the required beam divergence is significantly narrower than the required angular resolution, highlighting a mismatch between the two specifications. The pixelated DOPA leverages this distinction by decoupling the angular resolution from the constraints imposed by beam divergence.

The aperture is designed according to the beam divergence and FoV requirement, in terms of the aperture size $N_x p_x$ and the array pitch p_x, as what is normally needed for continuous DOPA. On the other hand, a discontinuity is introduced in the delay distribution network design, where the network is divided into M blocks, where each block is connected to N'_x antennas. The inputs of the blocks are kept in phase at all wavelengths by feeding them with a $1 \times M$ splitter, using a balanced splitter tree or a star coupler. Within each block, the differential delay of ΔL between each two consecutive antennas is maintained, preserving the phase relation between the antennas. However, no delay is introduced to the first antenna of each block, breaking the phase relation between the last antenna of a block and the first antenna of the next block, as shown in Fig. 2.13(a). The beams from different blocks interfere constructively only under a specific condition: when the phase delay between antennas within a single block matches the phase difference between the last and first antennas of neighboring blocks. Upon sweeping the wavelength, this condition is satisfied for specific wavelengths corresponding to specific spatial directions. Mathematically, we can assume the phase of the first antenna of the first antenna of the first block is $\phi_1 = 0$, then the phase of the last antenna in the block for N'_x antennas per block is:

$$\phi_{N'_x} = (N'_x - 1)\Delta\phi = 2\pi(N'_x - 1)\frac{\Delta L n_{eff}(\lambda)}{\lambda} \tag{2.28}$$

Since all the blocks are fed with equal phase, the next antenna in the array, i.e. the first antenna of the second block, will have a phase $\phi_{N'_x+1}$, equals to $\phi_1 = 0$, and so on for the subsequent blocks, i.e. $\phi_{N'_x+1} = \phi_{2N'_x+1} = ... = \phi_1 = 0$. For the blocks to interfere constructively, the phase difference between the last and first antenna of consecutive blocks should be equal to the phase difference between each two consecutive antennas within a block $\Delta\phi$, apart from an integer multiple m of

2π :

$$\begin{aligned} \phi_{N'_x+1} - \phi_{N'_x} &= \Delta\phi \pm m \cdot 2\pi \\ 0 - (N'_x - 1)\Delta\phi &= \Delta\phi \pm m \cdot 2\pi \\ N'_x \Delta\phi &= \pm m \cdot 2\pi \\ N'_x \frac{\Delta L . n_{eff}(\lambda)}{\lambda} &= m, \end{aligned} \tag{2.29}$$

where m has a very large value since $\Delta L >> \lambda$. The constructive interference between the blocks occurs at specific (discrete) wavelengths:

$$\lambda_m = \frac{N_x^{'}}{m} \, . \, \Delta L \, . \, n_{eff}(\lambda). \tag{2.30}$$

As the laser wavelength is swept, a narrow spot occurs only at these discrete *operation* wavelengths, each corresponding to a distinct point in the far field. Hence, we refer to this implementation as a *pixelated DOPA*, since sweeping the tunable laser produces discrete far field pixels rather than continuous scan lines, as shown in Fig. 2.13(b). Here, the angular resolution becomes a function of the number of antennas per block N'_x, instead of following directly from the aperture design, and is more coarse compared to that of the continuous DOPA, as shown in Fig. 2.13(c). This added design flexibility in the distribution network allows for a substantial reduction in the total length of the delay lines, thereby simplifying the overall circuit layout and minimizing both optical losses and phase errors.

Performance metric	**Design parameter**	**Equation**
Field of view along x-axis	Array pitch p_x	$\arcsin\left(\frac{\lambda}{p_x}\right)$
Field of view along y-axis	Antenna tunability $\frac{d\theta_y}{d\lambda}$	$\frac{d\theta_y}{d\lambda} \cdot \Delta\lambda$
Number of pixels along x-axis	Number of antennas per block N'_x	N'_x
Number of pixels along y-axis	Differential delay length ΔL	$\Delta L \cdot \frac{n_g \cdot \Delta\lambda}{\lambda^2}$
Beam divergence along x-axis	Antenna array length $N_x p_x$	$\frac{\lambda}{N_x p_x}$
Beam divergence along y-axis	Antenna strength α	$1/\alpha$

Table 2.1: Design parameters are set, assuming fixed material platform, i.e. fixed n_g, and available tuning range for the laser, i.e. fixed $\Delta\lambda$.

The beam steering performance metrics and the corresponding pixelated dispersive optical phased array parameters are shown in Table 2.1. This design space will be reiterated through the thesis, the more complexities are added to the system.

2.4 Phase errors in dispersive optical phased arrays

As with all photonic components and circuits, we are brought back to reality after fabrication, and DOPAs are no exception. Phase errors influence the performance of DOPAs, whether as a stand-alone beam steering element or within a full LiDAR system. This section discusses phase errors in dispersive optical phased arrays.

2.4.1 Origin and influence of phase errors

In fabricated photonic waveguides, the effective refractive index n_{eff} (or equivalently, the propagation constant β) is not perfectly uniform due to fabrication induced variations in the waveguide composition and geometry. These imperfections, such as errors in the waveguide width δw, thickness δt, core refractive index δn_{core}, and that of the cladding δn_{clad}, and even the waveguide length δL, as shown in Fig. 2.14, introduce random phase deviations $\Delta\phi$ along the propagation path [64]. While most of these errors are stochastic, others can be systematic, such as length variations introduced by grid snapping during mask file export [64, 65]. As light propagates, these phase deviations do not cancel out but instead accumulate following a random walk, where the uncertainty in phase gets larger the longer the light travels. In other words, the mean square phase deviation $\langle\Delta\phi^2\rangle$ grows proportionally with the propagation length L[length units]. This random phase accumulation can be characterized by the phase correlation length L_{cor}[length units], an intrinsic property of the waveguide, defined as the propagation length over which the mean square phase deviation $\langle\Delta\phi^2\rangle$ across a set of nominally identical waveguides reaches 2 radians squared [66]:

$$\langle\Delta\phi^2\rangle \equiv \frac{2L}{L_{cor}}. \tag{2.31}$$

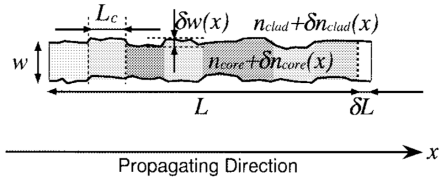

Figure 2.14: Fabrication errors leading to phase error accumulation, figure from [64].

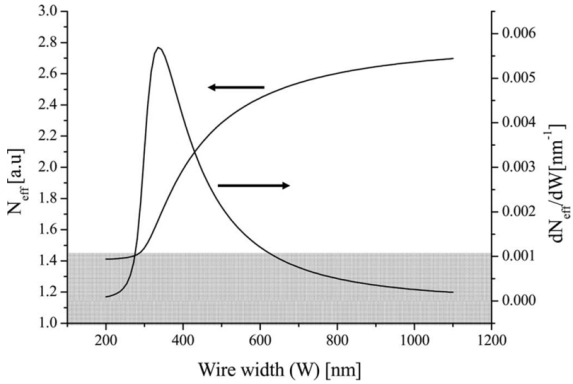

Figure 2.15: Variation of the effective index of the TE0 mode of a Si waveguide of height 220 nm at 1550 nm, figure from [68].

Waveguides with sidewall roughness can be represented as a sequence of segments with uniform width, each having a length equal to the correlation length L_{cor}, as shown in Fig. 2.14. In other words, the sidewall position does not change significantly within the correlation length [67].

The sensitivity of a waveguide to such phase fluctuations is especially pronounced in high index contrast platforms like silicon-on-insulator, where sidewall roughness plays a dominant role, as shown in Fig. 2.15. For a waveguide length that is larger than the correlation length, the standard deviation of the phase error $\delta\varphi$ resulting from the waveguide width deviation δw is:

$$\sigma(\delta\varphi) = \frac{2\pi}{\lambda}\frac{dn_{eff}}{dw} \cdot \delta w\sqrt{L_{cor}L}. \tag{2.32}$$

The effect of the sidewall roughness then propagates from the device level into the circuit level, Fig. 2.16, impacting the performance of more complex photonic circuits such as OPAs. In passive devices like DOPAs, phase errors arising from uncorrected geometry variations in the delay lines after fabrication can significantly degrade performance. In addition to accumulation in delay lines, other non-idealities, such as reflections and cross-coupling between the waveguides can introduce further phase distortions [62]. While this discussion focuses primarily on passive circuits, phase errors are also relevant in active OPAs. There, they may originate from thermal or electrical crosstalk between phase shifters, or from limitations in the optimization algorithms used to set the state of the phase shifters, which may fail to find the optimal point to establish the phase relation between the antennas [42]. Regardless of origin, phase errors at the input or along the antennas of an OPA distort the optical phase front. In the far field, this translates into the redistribution of the power between the main lobe, grating lobes, side lobes, and

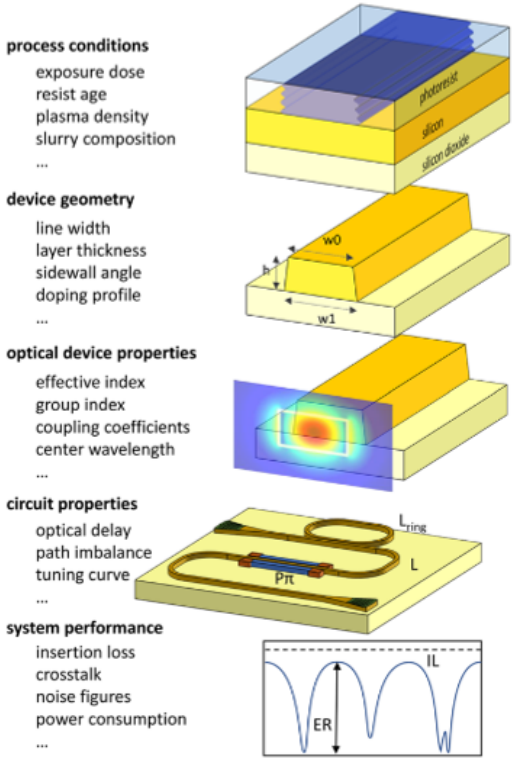

Figure 2.16: Variability can be described at different levels starting from the fabrication conditions up to the system/circuit performance metrics, figure from [6].

the background. This can be observed in the form of raising the background of side lobes between the main lobe and the grating lobes, and in the reduction of the power in the main lobe.

2.4.2 Mitigation of phase errors

There are several strategies to reduce potential phase errors in photonic waveguides and circuits during the design phase. Some of these approaches are used in the designs throughout this thesis. One approach is to use wide multimode waveguides, which better confine light within the core, making the propagation less sensitive to sidewall roughness. Additionally, choosing a lower index contrast platform such as silicon nitride instead of silicon can further mitigate sensitivity to fabrication imperfections. Ensuring symmetry in the design, such as matching the number of bends and tapers across different waveguide paths, also helps minimize differential phase errors. The layout itself can significantly influence phase errors, for example, reducing the length of the waveguides used for routing can reduce the accumulation of phase errors.

Phase errors can be compensated for after fabrication either through active tuning of the photonic circuit or by post-fabrication phase trimming of the waveguides. Active tuning relies on integrated phase shifters to dynamically compensate for phase mismatches, enabling reconfigurable correction at the expense of increased power consumption, control complexity, and thermal crosstalk. In contrast, phase trimming provides a permanent (non-volatile) correction of static phase errors, eliminating the need for continuous power dissipation and long-term feedback control.

A variety of phase trimming techniques have been reported in the literature, including thermal annealing and laser annealing of implanted regions in silicon waveguides [69–71]. While these approaches enable precise phase correction, they require additional fabrication steps such as ion implantation, thereby increasing process complexity. Alternative methods employ ultrafast laser pulses to locally modify the refractive index through amorphization of the silicon waveguide core [72, 73] or the surrounding glass cladding [74]. These techniques have demonstrated accurate phase adjustment of interferometric components, typically within a tuning range of up to 2π, around the design wavelength. However, such trimming inevitably introduces excess optical loss due to increased scattering and absorption at the modified regions.

3

Demonstration of dispersive optical phased arrays

This chapter presents the design, implementation, and experimental evaluation of dispersive optical phased arrays (DOPAs). It begins with the circuit design process of the continuous DOPA, on a schematic and a layout level, and touches on the components design. Here, the approach is bottom-up rather than top-down, aiming for a proof-of-concept demonstration without imposing rigid performance targets. The chapter then compares the pixelated DOPA and the continuous DOPA through

experimental results. Finally, the chapter concludes with a discussion, revisiting key design trade-offs and architecture comparisons to contextualize the performance and scalability of the presented demonstrations.

3.1 Circuit design of the continuous DOPA

A well-designed circuit at the schematic level does not always guarantee optimal performance after layout implementation. Layout decisions can have a significant impact on the overall performance of the system. For instance, the choice of delay line layout can substantially increase the circuit footprint, as will be illustrated in the design discussed in this chapter compared to the more compact implementation in chapter 5. Furthermore, routing strategies can either mitigate or accumulate evitable phase errors, directly affecting the performance of the optical phased array. For these reasons, the reporting of the design process in this work is deliberately divided into schematic level and layout level. This separation reflects a growing recognition in the photonics community of the critical distinction between schematic design and physical layout.

3.1.1 Schematic level

The first design choice is the waveguide material; whether it is Si or SiN [15]. Si has very high index contrast to the cladding, allowing for more compact waveguides and bends as opposed to SiN . In addition, group velocity index n_g of Si is larger

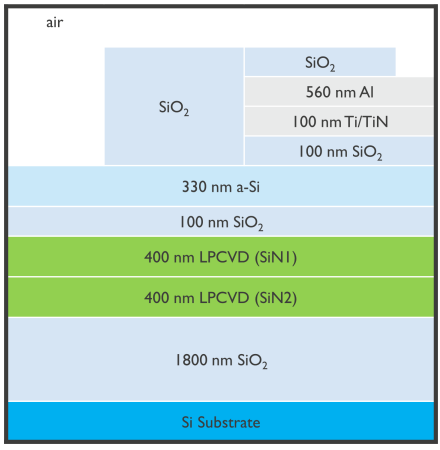

Figure 3.1: The stack used for the fabrication of the DOPAs used in this chapter.

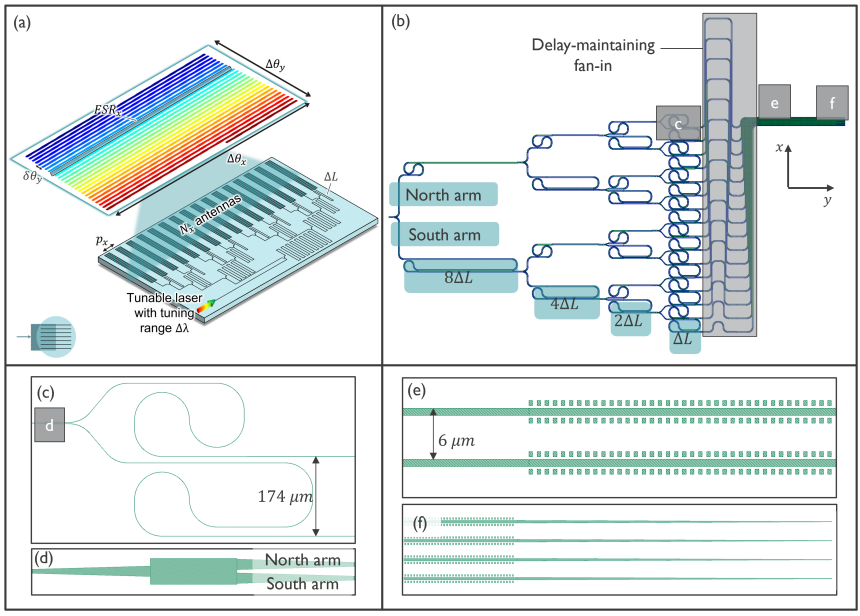

Figure 3.2: Schematic and layout views of the continuous DOPA circuit: (a) schematic view of the continuous DOPA showing the key parameters, and the expected 25 scan lines in the output; (b) layout view of the continuous DOPA showing the progressively increasing delay lines at each stage of the unbalanced splitter tree, the delay maintaining fan-in, and other key layout elements; (c) The output of the splitter showing the meander on the south arm contributing to the differential delay, and the dummy meander on the north arm. The spacing between the output waveguides of the distribution network is also shown to be $174\mu m$*; (d) zoomed view on the splitter that is based on an MMI; (e) zoomed view on part of the antenna array, showing the pitch of* $6\mu m$*; (f) zoomed view on the antenna termination with a taper.*

than SiN which allows slightly shorter delay lines to achieve the same number of scan lines, as given by Eq. 2.18 and 2.22. On the other hand, SiN is favored for its lower propagation losses and the lower sensitivity of its effective index to waveguide width, i.e. reduced phase error sensitivity, compared to Si. For this demonstration, LPCVD SiN stack on imec's 200 mm pilot line was chosen, as shown in Fig. 3.1. Only a single layer of SiN is used, i.e. SiN2. As introduced in Chapter 2, the circuit is based on an unbalanced splitter tree architecture. The antenna array consists of 16 elements, limited by the available chip area. To prevent evanescent coupling between antennas, a pitch of 6 µm was chosen, such that the theoretical x-axis FOV $\Delta\theta_x$ is 15°, following Eq. 2.4. The aperture width is then 90 µm, hence the theoretical beam divergence $FWHM_x$ is 0.87° at 0° emission angle, following Eq. 2.5. We targeted 25 scan lines within the y-axis FOV for the 100 nm wavelength range. The waveguide group velocity index n_g is extracted through Lumerical mode simulations, and is found to be 2.0. Based on Eq. (2.22) and Eq. (2.18), the differential delay line length ΔL is calculated to be 300 µm, around the center wavelength. A schematic of the circuit is shown in Fig. 3.2(a). The design of the antenna determines the FOV and FWHM along the y-axis.

Grating Antenna Design

There are several design configurations for periodic scattering elements to implement a weak and efficient grating antenna suitable for beam steering. Three main classes of weak antenna designs were considered:

- **Sidewall corrugation**, where periodic modulation is introduced directly into the waveguide sidewalls [75, 76], as shown in Fig. 3.3(a),
- **Side box perturbation**, involving periodic features placed adjacent to the waveguide core, as shown in Fig. 3.3(b),
- **Dual-layer**, where perturbations are embedded in a separate layer above or below the core [59, 77, 78], as shown in Fig. 3.3(c).

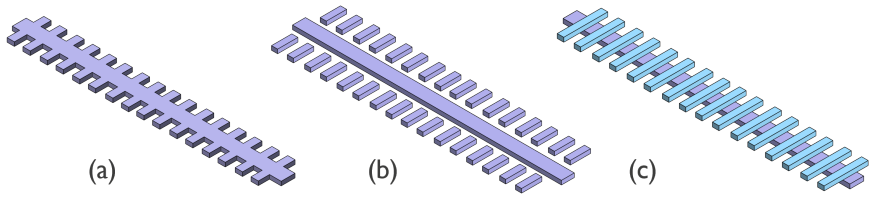

Figure 3.3: Antenna configurations: (a) Sidewall corrugation, (b) Side box perturbation, (c) Dual-layer.

Each configuration offers different trade-offs in terms of design complexity, control over emission strength, and compatibility with fabrication. Ultimately, the side box perturbation approach was selected due to higher control over emission strength compared to the side wall corrugation, and due to its relative simplicity in simulation and fabrication compared to the more complex multilayer structure. The antenna design was evaluated based on:

- *Tunability*, defined as the rate of change of emission angle with wavelength.
- *Antenna strength*, which directly controls the effective antenna length;
- *Emission efficiency*, quantifying the fraction of the light radiated upwards;
- *Emission profile along the cross-section*, describing the element factor contribution of the antenna,

where the first three metrics are described in section 2.2.1.

Design optimization was performed using FDTD simulations in Lumerical. The key design parameters are the grating period and duty cycle, as described in section 2.2.1. For the side box geometry, two extra parameters are considered, which are the side box width and the gap between the side box and waveguide core, as shown in Fig. 3.4 (a). Side perturbation has weak interaction to the field but they have symmetry in the stack, as the waveguide and the side boxes are fully-etched, so the efficiency will be less than 50%. A duty cycle of 0.5 maximizes efficiency but also increases antenna strength. The gap between the side box and waveguide core provides a tuning knob to weaken the interaction and reduce emission strength.

The final grating design features a period of 1 µm, duty cycle of 0.45, side box width of 0.8 µm and box-waveguide gap of 0.3 µm. This configuration yields a simulated antenna strength of approximately 17 dB/mm, resulting in an antenna

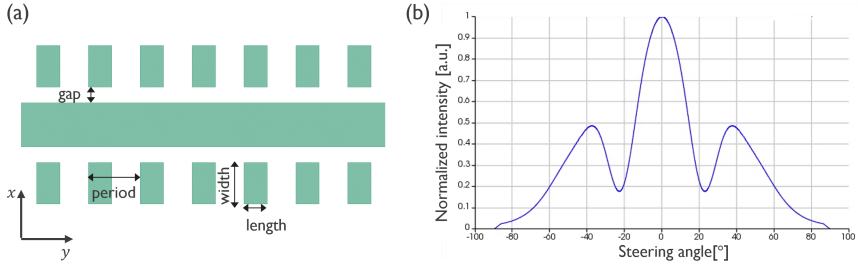

Figure 3.4: Side box antenna: (a) Top view showing the geometrical parameters, (b) Emission profile along the cross-section.

length (coupling length/decay length) just under 1 mm. Note that the unit for the strength is different from the described in section 2.2.1. The strength here is measured in [dB/mm] instead of a linear scale, corresponding to the $\frac{1}{2e}$ factor, meaning that a strength of 14.7 dB/mm corresponds approximately to a 1 mm antenna. The simulated beam steering response shows a tunability of approximately 0.07 °/nm, corresponding to a total field-of-view (FOV) along the y-axis of roughly 7° over a 100 nm tuning range. The element factor is shown in Fig. 3.4 (b).

The rest of the components, grating couplers for fiber in-coupling and 1×2 multi-mode interferometer (MMI), were available from the previous developers of the stack [1].

3.1.2 Layout level

The layout of the circuit is shown in the GDSII layout image, shown in Fig. 3.2(b). The unbalanced splitter tree architecture is designed such that only half of the branches at each splitting stage include delay lines. These delay lines are placed on the south output arm at each level of the splitter tree. The delay lines were implemented using meander-shaped waveguides with a bend radius of 60 µm. To maintain symmetry in the number of bends and reduce phase imbalance, additional "dummy" meanders are included on the north output arms, as shown in Fig. 3.2(c). The splitters themselves are based on 1×2 multi-mode interferometers (MMIs), each occupying a footprint of 62.5 µm×5 µm, including the tapers, as shown in Fig. 3.2(d).

To accommodate the footprint of the meander delay lines, the spacing between the output waveguides of the distribution network differs from the target pitch of the antenna array p_x, as shown in Fig. 3.2(c,e). To reconcile this mismatch without introducing additional delay between the antenna elements, a delay-maintaining fan-in routing strategy is used, as depicted in Fig. 3.2(b). The antennas are terminated with a taper to reduce back-reflections by radiating away any residue power in the antenna, Fig. 3.2(f).

In this layout, delay management and pitch matching are implemented in separate sections of the circuit, which results in a larger footprint than would otherwise be necessary. Moreover, the use of SiN imposes relatively large bend radii of approximately 60 µm to minimize bend losses, further contributing to the circuit's size. The footprint of the meander could be reduced by employing more compact low-loss bend geometries such as spline bends [79], Euler bends [80], or other adiabatic bend designs [81]. Since this work serves as a proof-of-concept

[1] designs by Jon Kjellman, and other legacy designs.

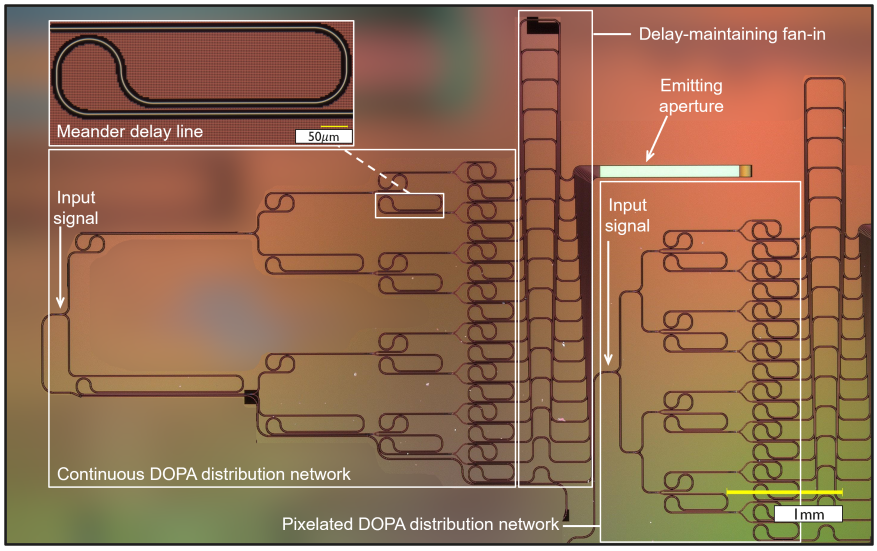

Figure 3.5: Microscope image showing the circuit of the continuous DOPA and the distribution network of the pixelated DOPA.

demonstration, optimization of these building blocks was not prioritized during the design phase.

A microscope image of the fabricated device is shown in Fig. 3.5.

3.2 Experiment results of continuous DOPA

A broadband measurement of the far field of the device is performed over the wavelength range of 1500 nm to 1600 nm. The far field images are acquired through a Fourier imaging setup. The conversion between the number of camera image pixels and the corresponding angular span is confirmed through the calibration on a known sample. For each wavelength, the far field image is taken at different laser power levels. Then, the image where the maximum pixel is on the verge of saturation is selected, where a peak detection algorithm is applied to identify the main lobe and grating lobe pixel positions. For beam steering along the x-axis, the FOV $\Delta\theta_x$ is measured from the separation between the mainlobe and the grating lobe, and is found to be approximately 15° around a central wavelength of 1550 nm, as shown in Fig. 3.6.

After identifying the relative angle of the mainlobe peak at every wavelength point, a mapping between the wavelength and the corresponding mainlobe angle is formed,

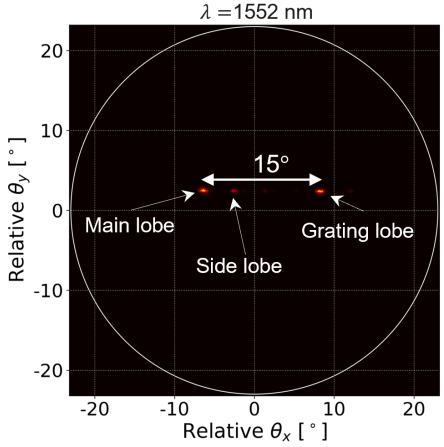

Figure 3.6: Far field image of the fabricated continuous DOPA at 1552 nm*, showing a separation of* ≈ 15° *between the main lobe and the grating lobe.*

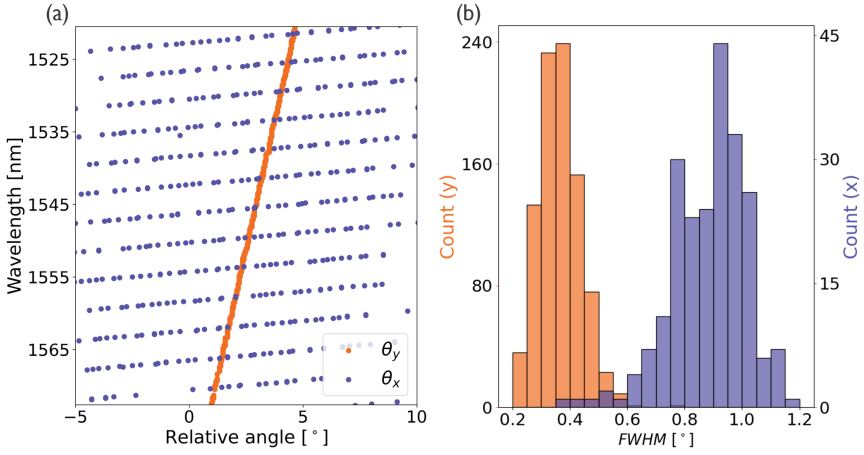

Figure 3.7: Experimental results from the fabricated continuous DOPA show: (a) Mapping between the wavelength and the corresponding mainlobe relative angle for the fast axis (x-axis) corresponding to delay line-based steering, and the slow axis (y-axis) corresponding to the gratings-based steering. Scan rates of approximately 3.66 °/nm *along the x-axis and* 0.072 °/nm *along the y-axis; and (b) FWHM distributions with median values of* 0.92° *in the x-direction and* 0.36° *in the y-direction, as illustrated by the corresponding histograms.*

as illustrated in Fig. 3.7(a). From such mapping, the scan rate $\frac{d\theta_x}{d\lambda}$ is measured to be approximately 3.66 °/nm.

Based on this scan rate and FOV, the wavelength range required to traverse one full scan line, i.e. the free spectral range $FSR_x = \Delta\theta_x/(\frac{d\theta_x}{d\lambda})$, Eq. 2.21, is approximately 4.1 nm. Over a total wavelength sweep of 100 nm, this results in around 24.5 distinct scan lines, as calculated using Eq.2.22.

Here, the beam divergence is defined as the the full width at half maximum (FWHM) of the mainlobe, which is measured as follows. A cutline of an unsaturated far field image is taken to get the cross-section of the beam profile, as shown in Fig. 3.8(a). The resulting cross-sectional profile, shown in Fig. 3.8(b), is normalized to the maximum possible pixel value of the camera. Within the main lobe, the pixels corresponding to half of the peak intensity are identified, and the span between these points is then converted into an angular width corresponding to the FWHM.

Beam divergence in the far field is dependent on both the emission angle and the operating wavelength, as shown in Eq. 2.5, and it can be further influenced by phase errors [82]. Due to the complexity of isolating these dependencies, a statistical approach is taken by plotting a histogram of FWHM divergence along the x-axis $FWHM_x$ based on 225 measurement data points at different wavelengths, as shown in Fig. 3.7(b). The median beam divergence in this direction is 0.92°, implying a far field sampling resolution $\delta\theta_x \approx 0.92°$, indicating 16 fully resolvable points per scan line. Accordingly, the required wavelength step for shifting from one resolvable point to the next within a scan line is approximately 240.4 pm.

In the y-direction, the scan rate $\frac{d\theta_y}{d\lambda}$ is much lower at approximately 0.072 °/nm, as shown in Fig. 3.7(a), leading to a total FOV of $\Delta\theta_y$ is 7.2° over the same 100 nm tuning range. Given the number of scan lines and the FOV, the far field sampling is estimated as $\delta\theta_y \approx 7.2°/24.5 = 0.29°$.

The y-axis beam divergence is also extracted for 910 wavelength points, as shown in Fig. 3.7(b), the median of which is 0.36°. The (decay/coupling) length of the antenna is then approximately 225 µm which is shorter than the design described in section 3.1.1. Designing long gratings in high index contrast platform is a significant challenge, since the guided mode is highly sensitive to geometric variations. At the same time, weak gratings require reproducible nanometer-scale perturbations, which is extremely difficult from a fabrication standpoint. In essence, any grating formed within a high index contrast waveguide tends to be too strong [60]. In addition, the gratings themselves can accumulate phase errors along their length [83].

A composite image of the continuous DOPA beam steering over a wavelength range of 100 nm is shown in Fig. 3.9. The composite is formed by overlaying individual frames acquired at discrete wavelength points. To improve the visual clarity of the

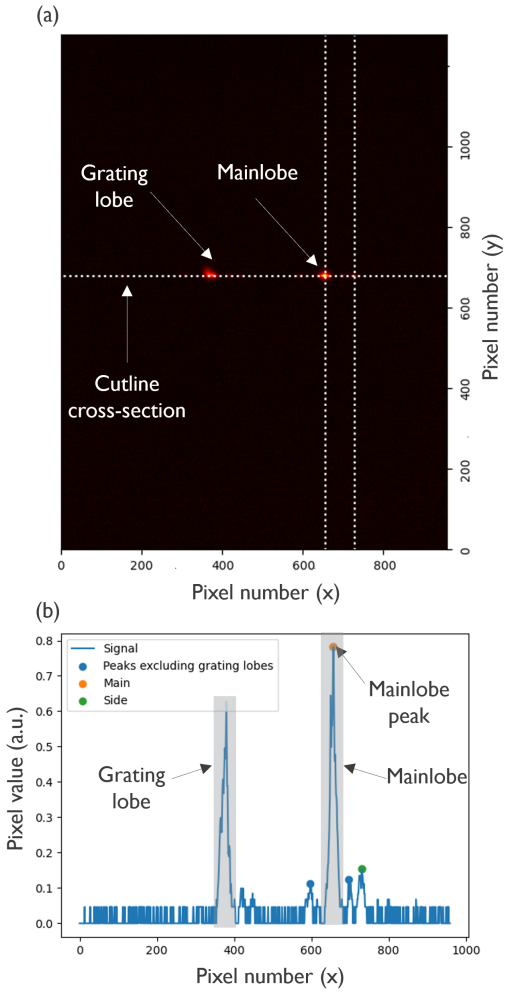

Figure 3.8: FWHM extraction: (a) an unsaturated far field image is used to take a cutline to get the cross-section of the beam profile. Note that this is a raw camera image; (b) The cross-section plot of the value of each camera pixel, the values are normalized to the maximum possible pixel value of the camera.

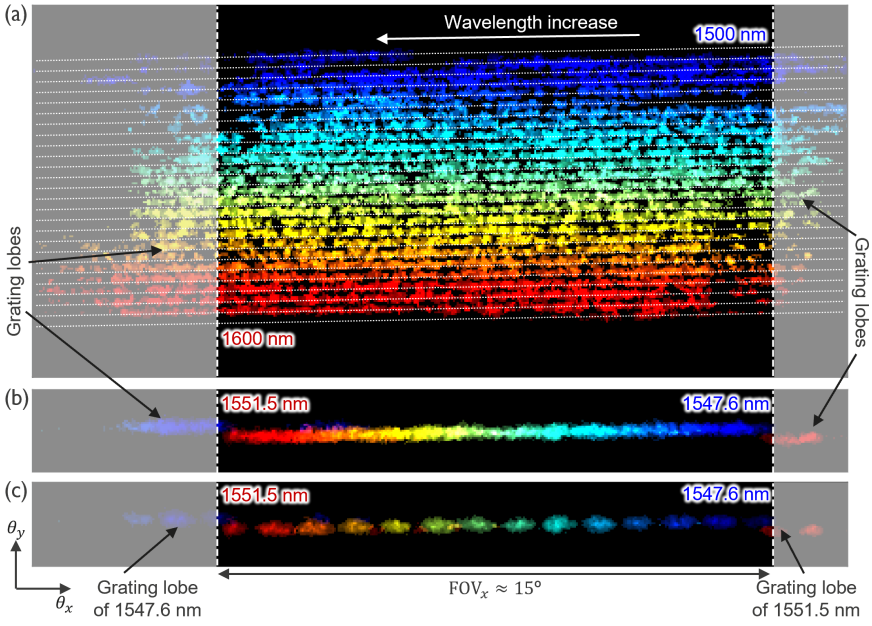

Figure 3.9: 2D beam steering results of the continuous DOPA: (a) A composite far field image generated from a wavelength sweep ranging from 1500 nm *to* 1600 nm *with a resolution of* 0.1 nm*, covering a field of view (FoV) of* 15°×7.2°*. In each frame contributing to the composite, only pixels exceeding a certain threshold are shown to visually separate the scan lines. (b) A single scan line acquired with the same wavelength resolution of* 0.1 nm *as in (a), but using a lower intensity threshold. This allows the scan line to appear visually continuous, as the wavelength resolution is smaller than the resolution limit of* 0.24 nm*, i.e., the wavelength step required to move between two consecutive resolvable points. (c) A single scan line captured using the same threshold as in (b), but with a larger wavelength step of* 0.3 nm*.*

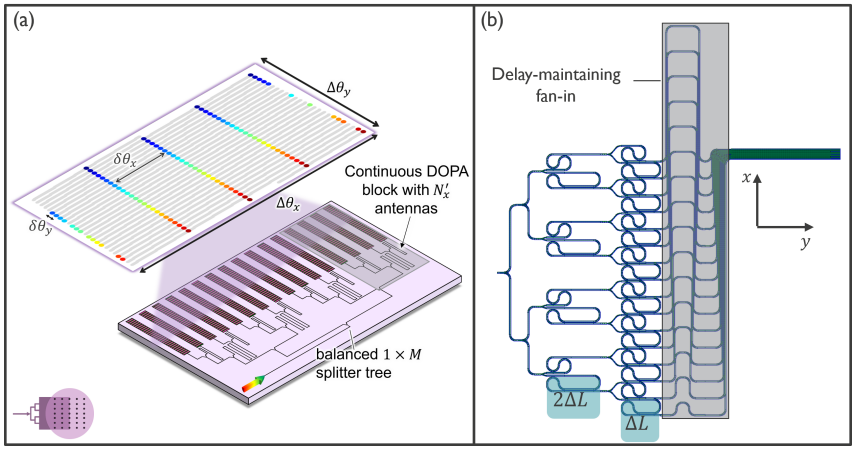

Figure 3.10: Schematic and layout views of the pixelated DOPA circuit: (a) schematic view of the pixelated DOPA showing the key parameters, and the expected 4 pixels per scan lines in the output; (b) layout view of the pixelated DOPA showing the progressively increasing delay lines at each stage of the unbalanced splitter tree and the delay maintaining fan-in.

scan pattern, only pixels exceeding a predefined intensity threshold are displayed in each frame, which allows the scan lines to be more clearly distinguished.

In Fig. 3.9(b), the scan lines appear more continuous than in Fig. 3.9(a), even though both measurements use the same wavelength step. This difference is not due to improved steering performance, but rather results from the lower pixel threshold applied in Fig. 3.9(b). The lower threshold makes the image more sensitive to variations in the detected optical power, thereby revealing a denser set of illuminated pixels along each scan line.

The observed power fluctuations originate from the experimental setup, in which the laser light is coupled into the chip using a fiber that is not mechanically fixed. Combined with the long acquisition time of the far-field measurement, this leads to slow variations in the coupling efficiency. The total measurement duration is substantial due to the large wavelength span of 100 nm, the fine tuning resolution of 0.1 nm, and the acquisition of 21 laser power levels at each wavelength point. These multiple power levels are required for the subsequent SLSR extraction procedure described in Section 3.4.2.

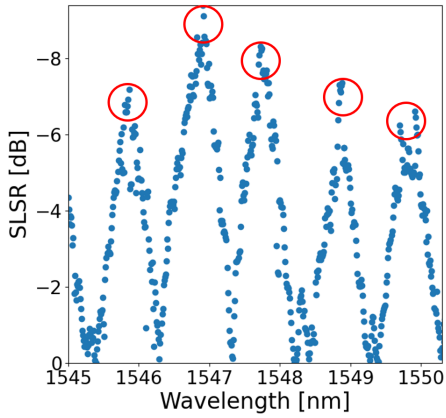

Figure 3.11: In the pixelated DOPA, the SLSR is used to pinpoint the wavelengths at which the constructive interference occurs.

3.3 Design of the pixelated DOPA

In order to perform a one-to-one comparison between the pixelated and continuous DOPAs, we design the pixelated DOPA to have the same aperture, differential delay line length ΔL, and distribution network choice as the continuous one. The distribution network is the only exception, where it is subdivided into four blocks fed by a balanced splitter tree. Each block has four antennas, so that a single scan line would have four pixels. For the continuous DOPA, the unbalanced tree has four levels, and the longest delay line is 4.5 mm. These values are reduced for the pixelated DOPA with two levels for the unbalanced tree, and longest delay of 0.9 mm. The schematic and the layout of the pixelated DOPA are shown in Fig. 3.10.

3.4 Experiment results of pixelated DOPA

Firstly, the specific wavelengths that produce constructive interference are identified, i.e. the operation wavelengths, to evaluate the beam steering of the pixelated DOPA. This is achieved by extracting the SLSR across a fine wavelength sweep. The operation wavelengths are observed as the local maxima for the SLSR, as shown in Fig. 3.11. In the x-axis direction, the steering range spans approximately 15° near 1550 nm, as shown in Fig. 3.12. The scan rate $\frac{d\theta_x}{d\lambda}$ is about 3.66 °/nm and the median $FWHM_x$ is 0.97°, as shown in Fig. 3.13 (a,b). Along the y-axis, the scan rate $\frac{d\theta_y}{d\lambda}$ is ≈ 0.072 °/nm yielding a FoV $\Delta\theta_y$ of 7.2° for the 100 nm sweep, and the median $FWHM_y$ is 0.36°, as shown in Fig. 3.13 (a,b). The angular separation

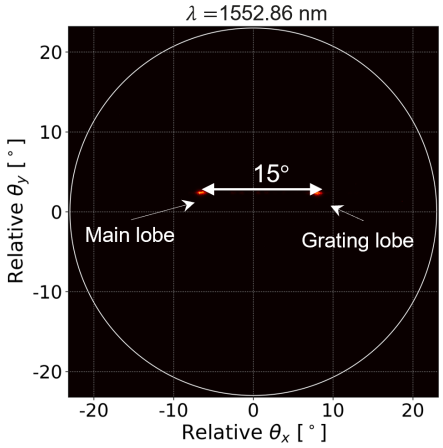

Figure 3.12: Far field image of the fabricated pixelated DOPA at 1552.86 nm*, showing a separation of* $\approx 15°$ *between the main lobe and the grating lobe.*

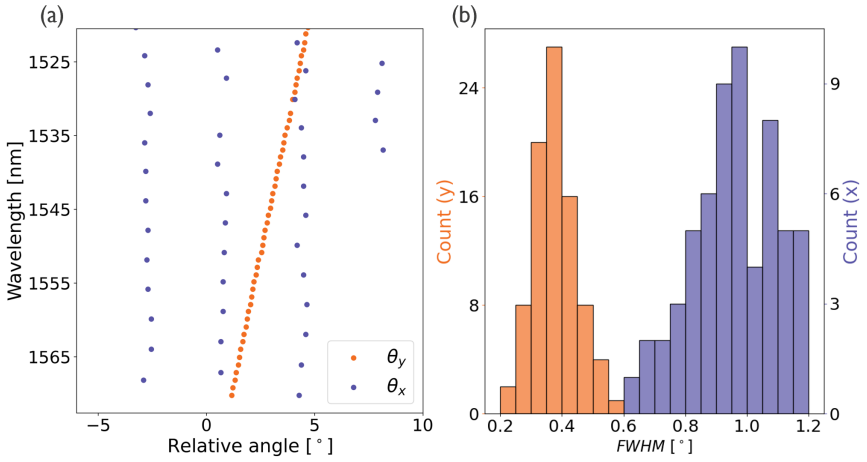

Figure 3.13: Experimental results from the fabricated pixelated DOPA show: (a) scan rates of approximately 3.66 °/nm *along the* x*-axis and* 0.072 °/nm *along the* y*-axis; and (b) FWHM distributions with median values of* 0.97° *in the* x*-direction and* 0.36° *in the* y*-direction, as illustrated by the corresponding histograms.*

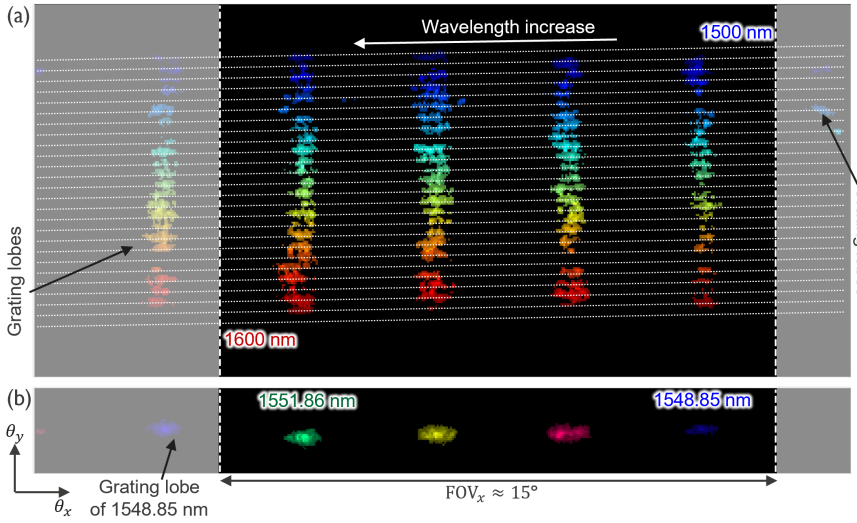

Figure 3.14: 2D beam steering results of the pixelated DOPA: (a) A composite far field image generated from a wavelength sweep between 1500 nm *and* 1600 nm*, sampled at the constructive interference wavelengths. In each frame contributing to the composite, only pixels exceeding a defined threshold are displayed to visually distinguish the individual scan lines. (b) A single scan line illustrating four resolvable spots per line. A lower threshold than in (a) is applied here to make the beam spots more clearly visible.*

between far field points along x is approximately 3.66°, which aligns with the four pixels per scan line set by the number of antennas per block $N_x^{'}$. The full far field beam steering results are shown in Fig. 3.14(a), and the individual pixels per scan line are illustrated in Fig. 3.14(b). The operating wavelengths are spaced by roughly 1 nm, meaning each incremental 1 nm shift in wavelength steers the beam to the next pixel along a scan line.

3.4.1 Phase errors

As mentioned in chapter 2, phase errors occurring either at the input or along the antenna array of an OPA distort the optical phase front. This leads to the redistribution of optical power in the far field, among the main lobe, grating lobes, sidelobes, and background. In order to compare both DOPA variations in terms of the phase errors, this section discusses side lobe suppression, main lobe power, and an introduced metric: crosstalk suppression. Unlike SLSR, crosstalk suppression captures the overall background level by excluding the main and grating lobes pixels and computing the 90^{th} or 95^{th} percentile of the remaining pixels.

Side lobe suppression ratio (SLSR), introduced in chapter 2, is commonly used alongside beam divergence to evaluate far field beam quality. It also serves as an indirect indicator of phase errors in both active and passive OPAs. However, two important questions arise: first, whether the SLSR adequately captures the effect of phase errors in (dispersive) OPAs, and second, whether it serves as a meaningful metric for evaluating a (dispersive) OPA within a LiDAR system.

The evaluation is nuanced. SLSR cannot be used to compare the phase errors resulting from different architectures, e.g. AWG vs. unbalanced splitter tree. Ideal Gaussian beams have no defined sidelobes, but as they are truncated, sidelobes grow, till the truncation is too large that it approaches a uniform distribution with an SLSR of 13.26 dB. However, the beam divergence of the Gaussian power distribution is usually higher than the far field sinc distribution of the uniform power distribution. At low antenna count, the fabricated AWG would have higher SLSR than the unbalanced splitter tree when based on 50:50 splitters, but it definitely has higher phase errors. It is worth noting that the unbalanced splitter tree can be engineered so that the splitting ratios of its branches approximate a Gaussian-like power distribution at the input of the antenna array.

Phase errors redistribute power from the main lobe into unintended directions. This power leakage reduces usable signal strength and can be quantified through main lobe power or crosstalk suppression, but not the SLSR. However, in terms of our measurement, the crosstalk was more straight-forward than the power in the main lobe, as it is a relative measurement.

Although a degraded SLSR implies the presence of phase errors, SLSR alone is not sufficient as it does not reveal where or how power is redistributed and erroneously directed to the all the other angles. Sidelobes that are close to the mainlobe can degrade the beam quality similar to increased divergence, while distant sidelobes pose a greater risk in LiDAR systems. In the worst case, a strong reflection from a distant sidelobe may overpower the true reflection from the mainlobe, leading to errors in ranging.

3.4.2 Measurement

Method

The method of extraction of the crosstalk and the SLSR is similar to the method used in [42].

At each wavelength point, far field images are captured at multiple laser power levels to compensate for the limited dynamic range of the infrared camera. As with

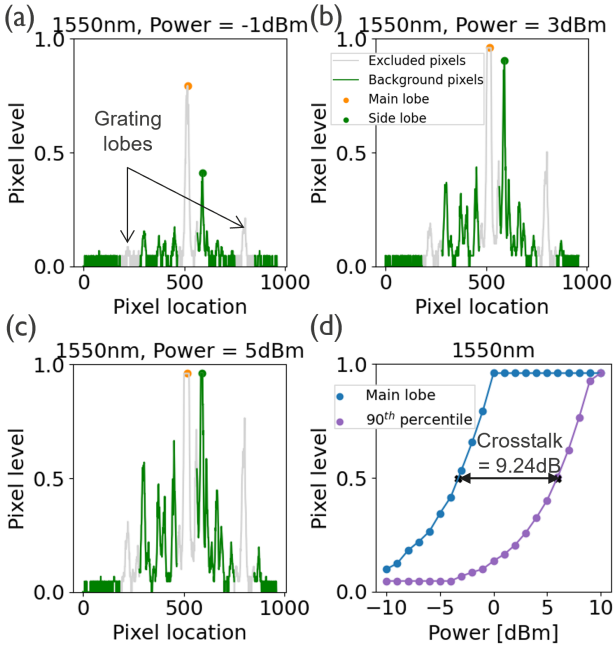

Figure 3.15: Crosstalk measurement method: (a–c) Far field images captured at varying input laser power levels, illustrating the main lobe, grating lobes, and background level; (d) Plot of the main lobe pixel intensity and the 90^{th} percentile of the background pixel intensity as functions of the laser power. The crosstalk level is determined by the difference in laser power at which the 90^{th} percentile background reaches the same intensity as the main lobe.

the beam steering characterization, we select the image where the maximum pixel is on the verge of saturation, and apply a peak detection algorithm to identify the main lobe and grating lobe pixel positions.

At each power level, we extract: the level of the main lobe pixel, the level of the highest side lobe pixel, and the 90^{th} percentile of the background pixel values, as shown in shown in Figs. 3.15(a,b,c). The latter is calculated by first excluding the main lobe and grating lobe pixels, then determining the 90^{th} percentile of the remaining pixel levels. Since the laser wavelength and antenna pitch $p_x$are known, the grating lobe positions relative to the main lobe are predictable.

By plotting the main lobe level and the 90^{th} percentile of the background level as functions of laser power, the crosstalk level can be extracted. The crosstalk level is determined by identifying the difference in laser power at which the 90^{th} percentile background reaches the same pixel value as the main lobe, as shown in Fig. 3.15(d). This comparison at equal pixel levels allows bypassing potential inaccuracies arising from the camera's nonlinear response, where pixel levels may not scale proportionally with the incident optical power. Similar plot is evaluated to extract the SLSR.

Results

The SLSR and the crosstalk suppression of the continuous DOPA are evaluated across 790 wavelength points, obtaining a median value of 3.6 dB and 9.5 dB, respectively. The distribution of these measurements is presented in Fig. 3.16(a). For the pixelated DOPA, the SLSR and crosstalk suppression of the pixelated DOPA are evaluated at the constructive interference (operating) wavelengths, using 70 and 63 wavelength points, respectively. The median SLSR is found to be 7.6 dB, and the median crosstalk suppression is 11 dB. The distributions of these measurements are illustrated in Fig. 3.16(b). It is worth noting that there is an unnecessary waveguide length introduced by delay-maintaining fan-in that contributes to additional phase errors in both devices. Furthermore, the delay lines are made from single mode waveguides which has higher sensitivity to sidewall roughness as opposed to wider multimode waveguides.

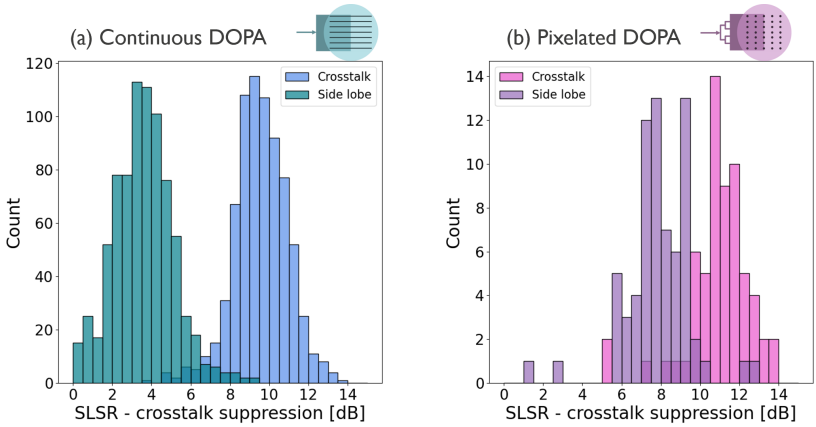

Figure 3.16: Evaluation of side lobe suppression (SLSR) and crosstalk performance of the DOPA devices: (a) For the continuous DOPA, the SLSR and crosstalk suppression were measured across the full wavelength range from 1500 nm *to* 1600 nm*. The results are represented by the histogram, and indicate a median SLSR of* 3.6 dB *and a median crosstalk suppression of* 9.5 dB*; (b) the measurements for the pixelated DOPA were performed at discrete wavelengths corresponding to the constructive interference. The histogram shows improved performance, where median SLSR is* 7.6 dB *and median crosstalk suppression is* 11 dB.

3.5 Discussion

3.5.1 Revisiting design space and tradeoffs

The motivation to introduce the pixelated DOPA can be seen in how it addresses the trade-off between the number of resolvable points along the slow axis (y-axis) and the phase errors inherent in the circuit. In continuous DOPAs, such phase errors are evident in the reduced SLSR, as reported in literature [46, 47, 49]. To achieve finer resolution along the y-axis for a given technology platform and laser tuning range, the differential delay length ΔL must be increased, as indicated by Eq. 2.18. A good continuous DOPA must carefully co-optimize these competing performance requirements.

The pixelated approach modifies the design space of DOPAs by using the number of pixels along the fast axis (x-axis) as a new design degree of freedom, alleviating this trade-off. For a given group velocity index of the waveguides in the distribution network, the required number of pixels along the y-axis (i.e., scan lines) sets the minimum delay line length ΔL for both pixelated and continuous DOPAs. In a continuous DOPA, the total number of antennas needed to achieve the desired beam divergence in the x-axis also determines the number of resolvable pixels

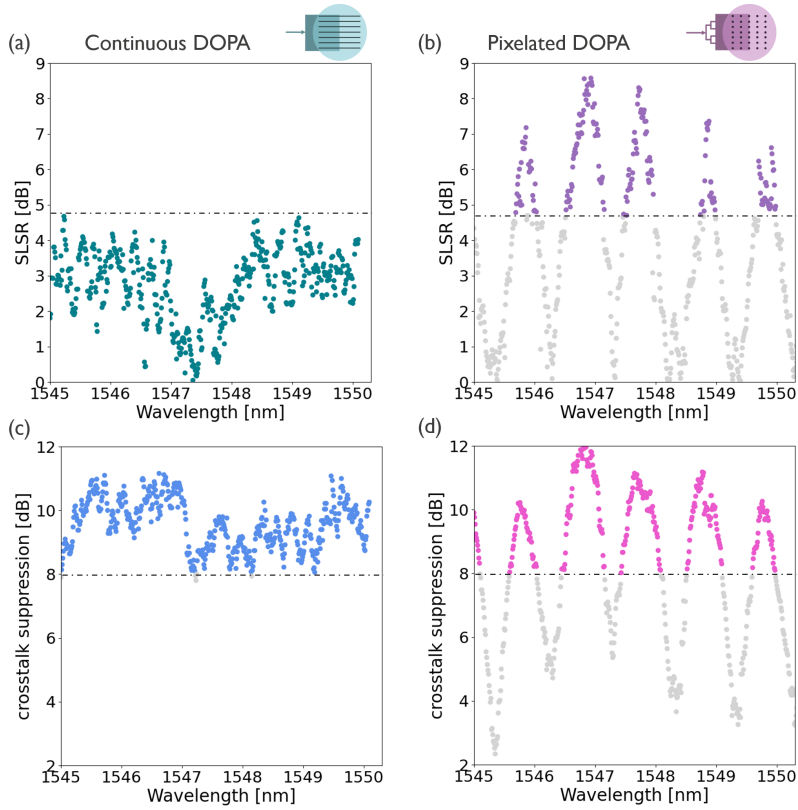

*Figure 3.17: Side lobe suppression ratio (SLSR) and crosstalk suppression performance of the DOPA devices over a a wavelength span of*5 nm*: the pixelated DOPA has an improved SLSR and crosstalk performance (b,d) over a broad wavelength range surrounding these operating points, in contrast to the continuous DOPA, which shows lower performance over the same range (a,c).*

per scan line, which in turn sets the length of the longest delay line. In contrast, for the pixelated DOPA, the number of pixels per scan line along the x-axis is an independent design parameter that defines the level of discretization, i.e., the number of antennas per block. The beam divergence only sets the limit for the best resolution possible with the given aperture. As a result, the degree of discretization controls the length of the longest delay line. This flexibility allows the pixelated DOPA to meet the resolution requirement in the y-direction while maintaining high beam quality, by choosing a practical number of pixels along the x-direction and keeping the overall delay line lengths more manageable.

In this study, the pixelated DOPA demonstrates a higher SLSR than the continuous DOPA at the operating wavelengths where a collimated beam is formed.

Metric	[41]	[46]	[47]	[48]	[49]	This work
Architecture	AWG	Snake	AWG	AWG	AWG	unbalanced tree
Platform	Si	Si	SiN	SiN	Si	SiN
N_x	16	32	39	128	128	16
$p_x[\mu m]$	2	16	6	4	2.07	6
$\Delta L[\mu m]$	87.7	>1600	65.4	54	20	300
$\delta\theta_x[^\circ]$	3.5 - 4	0.2	0.36	0.16	0.233	0.92
$\delta\theta_y[^\circ]$	1.14	0.059	1.4	1.7	3.47	0.29
$\Delta\theta_x[^\circ]$	50	5.5	15	22.9	43.9	15
$FWHM_x[^\circ]$	4	0.2	0.36	0.16	0.233	0.92 (median)
$FWHM_y[^\circ]$	3.5-4	0.11	0.175	0.13	0.05	0.36 (median)
SLSR [dB]	-	3 @ 1550nm	10 - 30	12.61	4.16	3.6 (median)

Table 3.1: Different realizations of the continuous DOPA architectures.

Additionally, it maintains superior SLSR performance over a broad wavelength range surrounding these operating points, as illustrated in Fig. 3.17 (a,b). A similar trend is observed for the crosstalk suppression as shown in Fig. 3.17 (c,d). From the comparison between Fig. 3.17 (a,c) and Fig. 3.17 (b,d), the pixelated DOPA outperforms the continuous version in terms of beam quality over a wavelength range of approximately 0.4 nm, corresponding to a bandwidth of about 50 GHz.

On the other hand, significant scanning blind spots along the x-direction can be observed in Figure 3.14. This is a result of the small scale of this demonstration, where the far field pixelation is relatively coarse, leading to an angular resolution of 3.66° in the x-axis. Conversely, the resolution along the y-axis reaches 0.29°, which is close to the 0.1° angular resolution typically required in LiDAR applications, due to the large differential delay used in the design. This results in minimal blind spots in the y-direction. To achieve both high beam quality and sufficient pixel density, an effective design must carefully balance the degree of discretization with the differential delay length.

3.5.2 Revisiting the architectures

Any of the architectures presented in chapter 2 can be employed within the pixelated DOPA to implement the individual blocks of the distribution network. Here, we present some of the considerations of these architectures by inspecting the relevant literature that implemented them in the continuous approach, as shown in table 3.1.

Most implementations [41, 47–49] use an arrayed waveguide grating (AWG) network. These typically employ a differential delay length $\Delta L < 100\,\mu\mathrm{m}$, resulting in poor resolution along the y-axis ($\delta\theta_y > 1^\circ$). While increasing ΔL and the number of antennas could improve resolution, it degrades beam quality due to

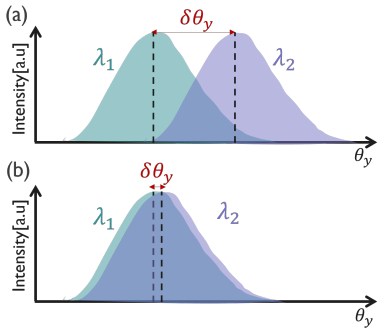

Figure 3.18: The angular resolution (a) becomes limited by the spot size when the FWHM is larger than the angular resolution (b).

accumulated losses and phase errors.

The snake architecture in [46] achieves superior angular resolution $\delta\theta_y$, but suffers from a limited unambiguous field of view in the x-direction $\Delta\theta_x$ due to the wide spacing between the antennas accommodating "flyback" paths, needed to connect the antenna. In contrast, the splitter tree allows higher aperture fill factor since it is not limited by the bend radius. Notably, the snake design reported in [46] uses an excessively large ΔL. When the spot size (FWHM_y) exceeds the resolution ($\delta\theta_y$), the number of resolvable points is limited by the spot size rather than the delay, as illustrated in Fig. 3.18. Since FWHM_y depends on the antenna emission profile, and $\delta\theta_y$ on ΔL, matching both ensures efficient use of delay length without introducing unnecessary phase errors.

Regarding the theoretical sidelobe suppression ratio (SLSR), the AWG can achieve high SLSR when using a star coupler as a splitter, due to its Gaussian-like power distribution. Similarly, the unbalanced splitter tree can achieve a Gaussian-like power profile by tuning the splitting ratios, typically ranging between 10:90 and 90:10, values well within fabrication tolerances. In contrast, replicating such a profile in the snake architecture would require extremely small initial splitting ratios, which are difficult to fabricate accurately.

The AWG is likely unsuitable for integration within large-scale DOPAs, even with the pixelated approach. However, a more detailed study of the snake and unbalanced tree architectures is needed to determine which is more appropriate for various application scenarios.

3.5.3 Revisiting LiDAR performance metrics

It is instructive to evaluate the performance of the Chapter 3 designs in the context of the automotive LiDAR metrics introduced in Chapter 1. The relevant performance parameters are summarized in Table 3.2.

The horizontal field of view (FoV) corresponds to scanning along the x-direction and is primarily limited by the antenna array pitch. As discussed in Chapter 3, the pitch must be sufficiently large to avoid evanescent coupling between the fan-in waveguides or adjacent antennas. This FoV can be expanded by optimizing the antenna design such that the antenna element factor suppresses the grating lobes.

The vertical FoV is determined by the wavelength tuning range and the grating tunability. It can be enhanced either by increasing the tuning range, similar to the approach in [46], where a 200 nm tuning range was employed, or by improving the grating tunability. The latter can be achieved by adopting slow-light grating implementations, such as those based on photonic crystal waveguides [84].

The strategies outlined above for extending the FoV to meet automotive LiDAR specifications would each require dedicated research efforts. From a rapid-development, or industrial perspective where leveraging existing technologies is often preferable to developing entirely new solutions, an alternative approach is to employ multiple OPAs to collectively cover the required FoV. This strategy is consistent with the approach demonstrated in [47] for DOPA based beam steering.

The maximum achievable range is constrained by the Rayleigh range of the optical aperture, which is limited to approximately 4 cm in the current design. Achieving the 30 mm aperture required for automotive LiDAR would necessitate a substantial increase in the effective aperture size. Along the x-direction, this can only be accomplished by increasing the number of antennas. In contrast, along the y-direction, the aperture can be extended through antenna optimization. In particular, long antennas can be realized by moving beyond conventional weak grating designs toward alternative concepts, such as the leaky fin antenna proposed in [60].

The differential delay line length of 300 µm results in a y-direction angular resolution of 0.29°, which is comparable to the 0.1° resolution typically required for automotive LiDAR. This delay line length also yields a wavelength step of 0.24 nm between adjacent resolvable points, corresponding to a bandwidth of approximately 30 GHz. This bandwidth comfortably exceeds that required to achieve the target range resolution, i.e.15 GHz. Consequently, the delay line length could be moderately increased to further improve angular resolution without compromising range resolution. This assessment, however, does not account for

LiDAR metric	Value	DOPA metric	Value
Horizontal FoV	45° – 90°	FoV_x	15°
Vertical FoV	10° – 30°	FoV_y	7.2°
Horizontal resolution	$\leq 0.1°$	$\delta\theta_x$	CDOPA 0.92°, PDOPA 3.66°
Vertical resolution	$\leq 0.1°$	$\delta\theta_y$	0.29°
Maximum range	200 m – 300 m	aperture size	96 µm×225 µm
Range resolution	15 cm	FSR_x	4.1 nm

Table 3.2: Comparison of LiDAR and DOPA performance metrics.

the increased phase errors that would accompany longer delay lines, which must be carefully considered.

Finally, the horizontal angular resolution of both the continuous and pixelated designs is significantly coarser than that required for automotive LiDAR. For a horizontal FoV of 15°, achieving the minimum angular resolution of 0.1° necessitates approximately $\frac{15}{0.1} = 150$ antennas. If this number of antennas is implemented in the continuous architecture, the resulting aperture size remains insufficient to meet the Rayleigh range requirement. In the pixelated architecture, using 150 antennas per block would require a total of $\frac{30\times10^3}{6\times150} \approx 33$ blocks to achieve the necessary effective aperture for the target Rayleigh range. As before, the impact of increased phase errors associated with the larger antenna count and extended optical paths needs to be taken into account.

4

Dispersive OPAs with FMCW ranging

In this chapter, we will widen our scope to outline the principles and design considerations for combining frequency-modulated continuous-wave (FMCW) ranging with dispersive optical phased arrays (DOPAs). The chapter begins by reviewing the principles of FMCW ranging, including the LiDAR equation and key performance metrics, such as range resolution and precision. Beam steering and FMCW ranging with a single wavelength variable is then explored, where various implications on the system operation are discussed. The discussion extends to multiplexing strategies for ranging engines, revisiting the design space in view of system trade-offs, followed by a case study to consolidate the understanding of this coupled design space.

4.1 FMCW ranging

4.1.1 Working principle

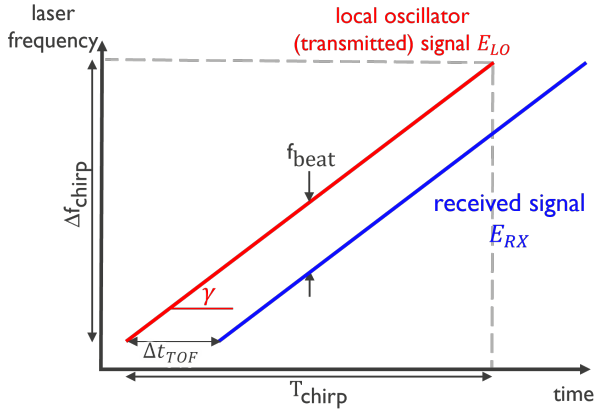

Figure 4.1: FMCW waveform and its parameters.

In FMCW LiDAR receiver, a frequency-modulated waveform, typically sawtooth, or triangular for additional velocity measurement, is generated. The sawtooth waveform is a linearly chirped optical signal, as shown in Fig. 4.1, where the chirp rate is:

$$\gamma = \frac{\Delta f_{\text{chirp}}}{T_{\text{chirp}}}, \tag{4.1}$$

with Δf_{chirp} representing the chirp bandwidth and T_{chirp} the duration of the chirp.

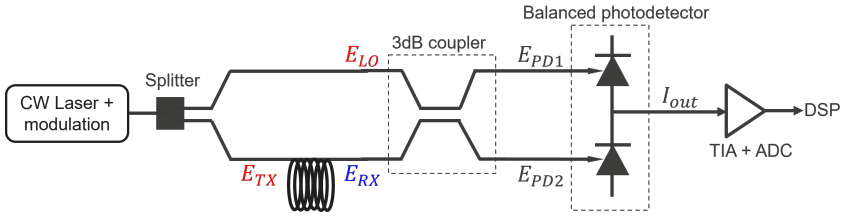

Figure 4.2: FMCW coherent detector.

The laser output is split into two paths, as shown in Fig. 4.2. The first acts as the local oscillator signal E_{LO} for the coherent receiver. Ideally, the local oscillator signal should be high enough to achieve the shot noise-limited detection. In the shot noise limit, the local oscillator shot noise overpowers other extraneous noises, such as thermal noise, that they can be neglected.

The other path serves as the transmitter signal. The transmitter signal couples to free space through transmitter optics. Upon hitting a target, part of the signals scatters back into the receiver after a round-trip time delay Δt_{TOF}, as illustrated in Fig. 4.1. This return signal E_{RX} is collected by the receiving optics and is directed to the coherent receiver.

In the coherent receiver, the received signal is mixed with the local oscillator signal. The optical realization of the mixer is a symmetric 2×2 3 dB coupler, represented by the matrix:

$$c = \frac{1}{\sqrt{2}} \begin{bmatrix} 1 & -j \\ -j & 1 \end{bmatrix} \tag{4.2}$$

In principle, a single port of the output can be used with a single photodiode, however this means that half of the input power is wasted. That is why coherent receiver use at least two photodiodes in a *balanced photodetector* (BPD) configuration, as shown in Fig. 4.2. In addition, if the optical paths of the coupler are balanced and the frequency response of the photodiodes is matched, then the DC currents of the photodiodes cancel out, achieving common mode rejection [85]. The photodetector current is proportional to the optical power of the signal, and the detector responsivity R_{PD}. The signal power on the first photodetector is:

$$\begin{aligned} |E_{PD1}|^2 &= \frac{1}{2}\left(E_{RX}e^{-j\omega_1 t} - jE_{\mathrm{LO}}e^{-j\omega_2 t}\right)\left(E_{RX}e^{j\omega_1 t} + jE_{\mathrm{LO}}e^{j\omega_2 t}\right) \\ &= \frac{1}{2}\left(E_{RX}^2 + E_{\mathrm{LO}}^2 + jE_{RX}E_{\mathrm{LO}}e^{-j(\omega_1-\omega_2)t} - jE_{RX}E_{\mathrm{LO}}e^{j(\omega_1-\omega_2)t}\right) \\ &= \frac{1}{2}\left(E_{RX}^2 + E_{\mathrm{LO}}^2 - 2E_{RX}E_{\mathrm{LO}}\sin((\omega_1-\omega_2)t)\right), \end{aligned}$$

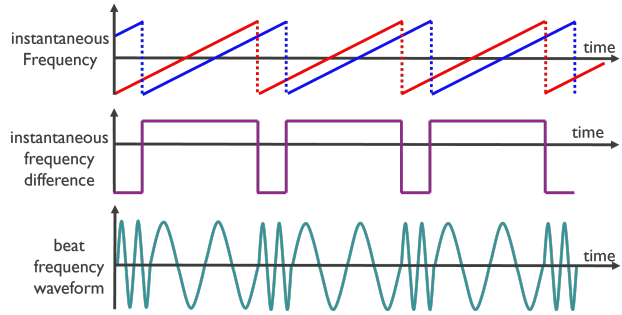

Figure 4.3: FMCW beat signal representations.

where $e^{jx} = \cos x + j \sin x$, following basic trigonometry. Similarly, the signal power on the second photodetector is:

$$\begin{aligned} |E_{PD2}|^2 &= \frac{1}{2}\left(E_{\text{LO}}e^{-j\omega_2 t} - jE_{RX}e^{-j\omega_1 t}\right)\left(E_{\text{LO}}e^{j\omega_2 t} + jE_{RX}e^{j\omega_1 t}\right) \\ &= \frac{1}{2}\left(E_{RX}^2 + E_{\text{LO}}^2 + jE_{RX}E_{\text{LO}}e^{j(\omega_1-\omega_2)t} - jE_{RX}E_{\text{LO}}e^{-j(\omega_1-\omega_2)t}\right) \\ &= \frac{1}{2}\left(E_{RX}^2 + E_{\text{LO}}^2 + 2E_{RX}E_{\text{LO}}\sin((\omega_1-\omega_2)t)\right) \end{aligned}$$

In a balanced configuration, the photocurrent output from the photodiodes is proportional to the power difference between the two outputs of the 3 dB coupler:

$$\begin{aligned} |E_{PD2}|^2 - |E_{PD1}|^2 &= 2E_{RX}E_{\text{LO}}\sin\left((\omega_1-\omega_2)t\right) \\ I_{out}(t) &= 2R_{PD}E_{RX}E_{\text{LO}}\sin\left((\omega_1-\omega_2)t\right). \end{aligned} \tag{4.3}$$

This mixing process produces a baseband signal whose instantaneous frequency corresponds to the beat frequency f_{beat}, as shown in Fig. 4.3. The frequency of the BPD output waveform is the beat frequency:

$$\omega_{beat} = \omega_1 - \omega_2 = 2\pi\gamma(\tau_1 - \tau_2) = 2\pi\gamma\Delta t_{TOF} \tag{4.4}$$

The range to the target is then derived from this beat frequency using the relation:

$$R = \frac{c \cdot \Delta t_{\text{TOF}}}{2} = \frac{c \cdot f_{\text{beat}}}{2\gamma}, \tag{4.5}$$

where c is the speed of light. As shown in Fig. 4.2, a digital signal processing (DSP) module is used to compute the discrete Fourier transform of the beat signal and identify its peak frequency, from which the distance is estimated.

4.1.2 Advantages

The nature of operation of coherent detection is inherently immune to ambient light, where only light that is phase coherent with the local oscillator contributes to the detected signal, effectively rejecting background illumination and crosstalk from other sources. Additionally, the coherent detection allows the amplification of the weak return signal through the mixing process with the strong local oscillator, as shown in equation 4.3. This amplification permits the use of relatively noisy detectors typically operating in shot-noise-limited regime. This condition is met when the local oscillator signal is strong enough such that its shot noise dominates all other noise contributions in the system, including the detector noise. Finally, the down-converted beat signal lies in the RF domain, enabling efficient and precise electronic processing.

4.2 FMCW LiDAR link

4.2.1 Signal-to-noise ratio

Understanding the signal-to-noise ratio (SNR) in coherent LiDAR enables a more concrete approach to system design, guiding initial choices such as the minimum required received power and the optimal local oscillator power for shot noise limit.

The electrical power SNR is the ratio between the mean squared signal current to the mean squared noise current [86]. The mean squared signal current is:

$$\bar{i}_s^2 = 2R_{PD}^2 P_{LO} P_{RX}. \tag{4.6}$$

As mentioned in the previous section, the detector is shot noise limited, where the mean squared noise power is:

$$\bar{i}_N^2 = 2qR_{PD} P_{LO} B, \tag{4.7}$$

where B is the detection bandwidth, which is the inverse of the measurement (integration) time. Note that the measurement time is often approximated as the chirp time:

$$B = \frac{1}{T_{meas}} \approx \frac{1}{T_{chirp}}. \tag{4.8}$$

The signal to noise ratio is then:

$$SNR = \frac{R_{PD}.P_{RX}}{q.B}, \tag{4.9}$$

where the term $\frac{q.B}{R_{PD}}$ is the noise equivalent power (NEP) of the receiver. It can be observed that shorter measurement durations demand higher received power to maintain the same SNR performance. This balance is critical in meeting performance targets within system constraints like frame rate and link budget.

4.2.2 Link budget and LiDAR equation

The received power P_{RX} in a coherent LiDAR link is described by the LiDAR equation, which incorporate all the losses (efficiencies) along the signal path until its detection. There are few assumptions to start with and to make along the way as first approximations.

First, a monostatic configuration is assumed, meaning that the transmitted and received beam share the same path. The monostatic configuration can be in a dual aperture configuration where the transmitter aperture is different from the receiver aperture, but they are close enough that the transmitted and received beam share the same path. Additionally, the monostatic configuration can be in a single aperture configuration where the transmitter and receiver share the same aperture. Here, a monostatic single aperture is referred to as monostatic configuration and a monostatic dual aperture as bistatic configuration. This is not to be confused with the radar terminology where the bistatic configuration means that the transmitter and receiver are separated by a significant distance.

Second, an untruncated infinite Gaussian beam is assumed. Essentially, we are dealing with a collimated beam, which requires operation within the Rayleigh range. The received powerP_{RX} can be expressed as [86]:

$$P_{RX} = 2\eta_p \, \rho(\pi) P_T \, \frac{\lambda^2}{\pi \omega^2(z)} \eta_T \eta_D, \tag{4.10}$$

where P_T is the transmitted power. $\omega(z)$ is the beam radius. η_T is known as the *capture efficiency*. η_D takes values between $\frac{1}{2}$ for an infinitely large diffuse target, and 1 for the limiting case where the power intercepted by the target is much smaller than the beam. $\rho(\pi)$ is the inverse steradian power reflectivity of the target. η_p accounts for the overall system efficiency. That is $\eta_p = \eta_o \eta_e \eta_a$, where η_o accounts for the internal optical losses of the system, η_e is the heterodyne or mixing efficiency, and η_a accounts for the atmospheric losses from absorption and scattering. The concept of heterodyne efficiency is rooted in Siegman's antenna theorem [87] that describes the wavefront alignment between the signal and the local oscillator. The maximum heterodyne efficiency occurs when the signal and the local oscillator overlap perfectly, where the two beams are aligned in phase and polarization. The mixing efficiency can be calculated by the backpropagated local

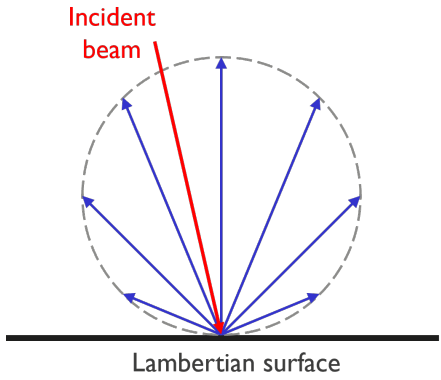

Figure 4.4: Diffuse Lambertian scatterer behavior.

oscillator method. In this method, the local oscillator field is backpropagated to the far field to the same plane as the transmitted beam, and the overlap integral can be taken at this plane to calculate the mixing efficiency.

The target is modeled as a diffuse Lambertian scatterer. A Lambertian scatterer diffuses incoming light such that the scattered intensity follows a cosine angular distribution, as shown in Fig. 4.4. This distribution remains the same regardless of the angle at which the light strikes the surface. The target is assumed to be infinite compared to the beam, which makes $\eta_T \rightarrow 1$ and $\eta_D \rightarrow \frac{1}{2}$. For a collimated beam with Rayleigh range $z_0 = \frac{\pi\omega_0^2}{\lambda}$, and for an infinite target, the received power P_{RX} can be written as:

$$P_{RX} = \eta_p \, \rho(\pi) P_T \, \frac{\pi D^2}{4z^2}, \tag{4.11}$$

where $D = 2\omega_0$ is the diameter of the receive aperture.

It is important to note that the received power is inversely proportional to the square of the distance, which is a direct consequence of operating within the Rayleigh range with a collimated beam. If the beam is diffracted beyond the Rayleigh range, where the target is considered smaller than the beam, equation 4.11 becomes:

$$P_{RX} = 2\pi \, \eta_p \, \rho(\pi) P_T \, \frac{\pi D^2}{4z^2} \frac{A_t}{A_b}, \tag{4.12}$$

where the term $\frac{2A_t}{A_b}$ is the first-order approximation of the capture efficiency η_T. When A_b is expanded, the received power scales inversely with the distance to the power of four, i.e. $P_{RX} \propto \frac{1}{z^4}$ [86], and the equation is called R^{-4} range equation or two-way range equation. That is why it is important to operate within

the Rayleigh range in our context to reduce the penalty of free-space propagation in the link budget.

4.2.3 Ranging performance metrics

Range resolution

Range resolution δR represents the smallest separation at which two targets, along the same line of sight, can be distinguished. If the separation exceeds δR, the targets can be resolved individually in range; if it is smaller, they will appear at the same distance. δR is fundamentally limited by the chirp bandwidth [88]:

$$\delta R = \frac{c}{2BW} = \frac{c}{2\Delta f_{chirp}} \tag{4.13}$$

This equation applies to any time-of-flight range measurement method, however, coherent LiDAR typically achieves the highest range resolution [20]. A typical range resolution requirement for autonomous driving is 15 cm which corresponds to a chirp bandwidth of 1 GHz.

Range precision

The measurement precision quantifies the uncertainty in the measurement. The range measurement is essentially an *estimation* of the distance from the received signal. The range precision is the standard deviation of this estimate error [89]. The variance of a parameter estimate is inversely proportional to the SNR :

$$\sigma_R^2 = \frac{k}{SNR}, \tag{4.14}$$

where k is some constant. For such parameter estimation, it is useful to know the theoretical limit on the accuracy achievable with the available data. The Cramér–Rao lower bound (CRLB) specifies the minimum possible variance (i.e., squared precision) attainable by any unbiased estimator. It can be shown that the variance in the time-delay estimation σ_τ^2 is inversely proportional to the bandwidth, so the CRLB of the time-delay estimation:

$$\sigma_\tau^2 \geq \frac{1}{SNR\,.\,BW^2}. \tag{4.15}$$

It is valid to take the range precision as:

$$\sigma_R \geq \frac{c}{2BW\sqrt{SNR}} = \frac{\delta R}{\sqrt{SNR}}. \tag{4.16}$$

The range precision improves with higher SNR and finer range resolution. In this work, the design space will be considered in terms of SNR and range resolution, where range precision will not be treated as an independent performance metric.

Equations 4.13 and 4.16 show that the chirp bandwidth and the signal-to-noise-ratio (SNR) of the system are the fundamental limiting factors for the ranging engine.

Minimum detectable signal

The minimum detectable signal is the weakest signal a receiver can reliably identify [52]. Setting a specification to the minimum detectable signal is challenging due to its statistical nature and the ambiguity in defining what constitutes a detectable target. Detection relies on setting a threshold at the receiver output: lowering the threshold improves sensitivity to weak signals, but increases the risk of detecting the noise crossing the threshold as signal. Such incidence is called false alarms. Conversely, raising the threshold reduces false alarms but may cause missed detections.

Due to the inherent randomness of signals, lidar/radar detection performance is described using probabilities, most commonly the probability of detection P_D and the probability of false alarm P_{FA}. P_D refers to the probability that a signal containing both target and noise exceeds the detection threshold, while P_{FA} represents the probability that noise alone crosses the threshold, falsely indicating a target. Increasing the probability of detection will automatically raise the probability of false alarm. Therefore, selecting the optimal threshold is a trade-off between the probability of missing a real signal and falsely detecting one.

The system requirements set the required detection probability P_D and the acceptable limits for the probability of false alarm P_{FA}. The minimum required signal-to-noise ratio $SNR_{threshold}$ is then determined based on the combination of these requirements, as shown in Fig. 4.5. For instance, a probability of detection of 0.9 and probability of false alarm of 10^{-6} requires an $SNR_{threshold}$ of 13.2 dB. This $SNR_{threshold}$ is used to calculate the minimum detectable signal, which is also called the receiver sensitivity:

$$P_{RX} \geq \frac{q.B}{R_{PD}}.SNR_{threshold}. \tag{4.17}$$

4.3 FMCW LiDAR link considerations

In this section, the FMCW LiDAR link is qualitatively described, including considerations that are not addressed in this thesis. The goal is to provide a big picture perspective, and touch on some of the mentioned aspects at later points. These considerations are summarized in Fig.4.6.

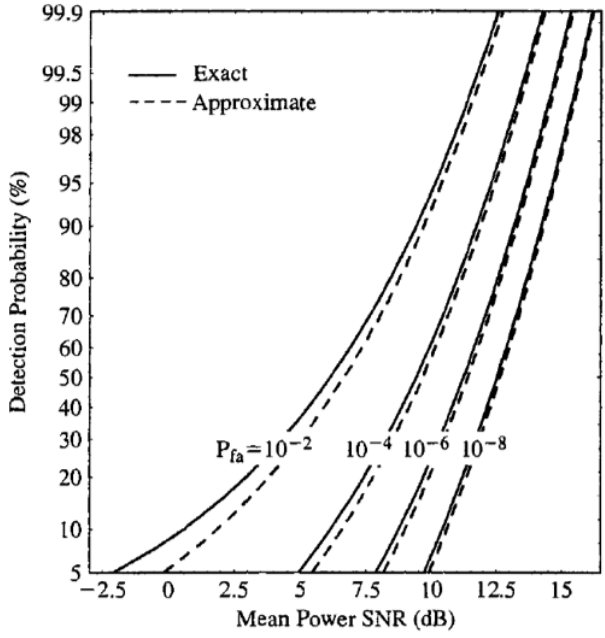

Figure 4.5: Probability of detection as a function of the mean power signal-to-noise ratio with the probability of a false alarm as a parameter, figure from [86].

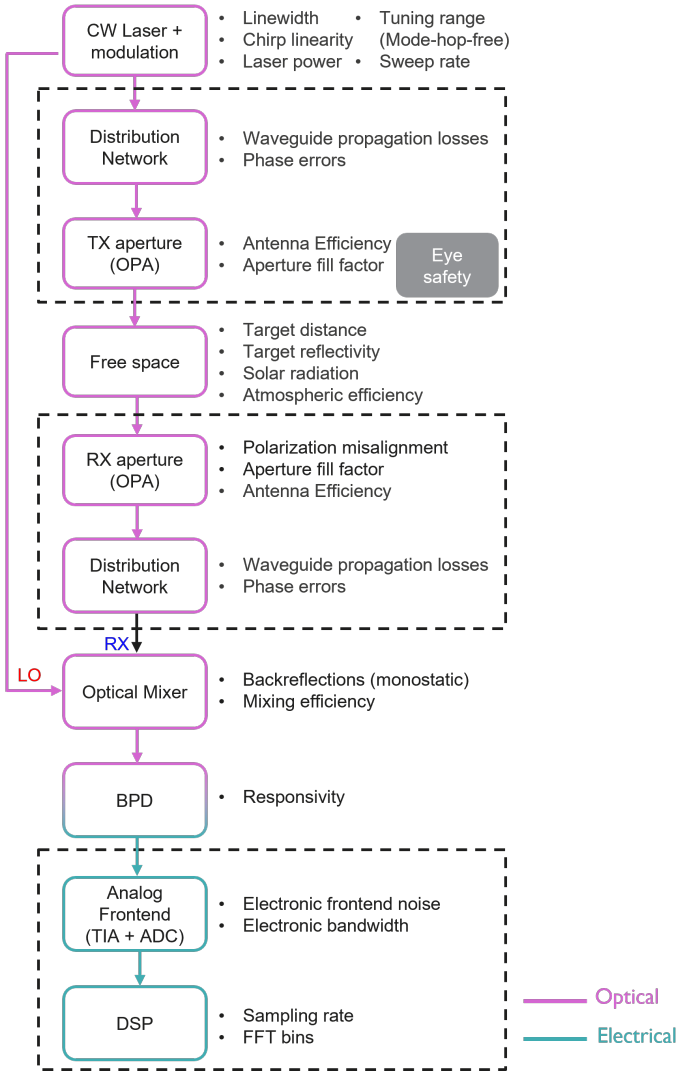

Figure 4.6: Some practical considerations associated with FMCW LiDAR link.

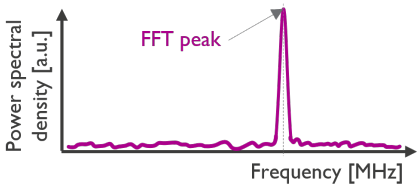

Figure 4.7: FMCW beat signal waveform in the frequency domain.

FMCW signal generation

The light signal is generated by a continuous-wave (semiconductor) laser. The laser signal is modulated in a sawtooth or triangular waveform, where the modulation is achieved either by externally modulating the laser or by directly tuning the laser frequency.

The laser phase noise determines the spectral linewidth of the laser Δv, which is a critical parameter for both the maximum range and the range resolution [90].

Phase noise introduces power penalties in the detected signal and directly impacts the maximum range [91]. Optimally, the received signal should have traveled a distance less than the coherence length L_{coh} of the laser, where:

$$L_{coh} \approx \frac{c}{\Delta v}. \tag{4.18}$$

As mentioned earlier, the theoretical range resolution is limited by the chirp bandwidth. However, with non-ideal lasers, the range resolution degrades with chirp non-linearity and laser phase noise [90, 92]. Since the range is estimated from the FFT spectral peak, as shown in Fig. 4.7 the width of the FFT peak affects the resolution of the range measurement. The laser linewidth causes spectral broadening in the beat signal reducing the measurement resolution, while non-linear chirp causes variation in the beat frequency, which increases the bandwidth of the beat signal.

A portion of the laser signal is tapped off to act as the local oscillator (LO), typically taking $1\% - 10\%$ of the laser signal, while the remaining power is routed to the transmitter. Rigorously calculating the local oscillator power for shot noise limit requires considering the thermal noise and the electronic frontend noise [82].

Link budget

During propagation through the distribution network, the signal experiences losses due to propagation in waveguides and splitting.

Phase errors at the input of the aperture can distort the phase front by redistributing the power from the desired emission angle (main lobe) to other angles. This means that the effective signal power is attenuated. Additionally, the power increase at other angles can result in the reflections off other objects, contributing to crosstalk, especially if the object along the main lobe direction is far, and the other objects are close.

Additional losses occur at the aperture, originating from limited antenna efficiency and non-unity aperture fill factor. We can assume that we are able to push the power out of the aperture up to the eye safe limit despite circuit losses. This is considered an assumption because if the circuit losses are too high, it might be impossible to push the output power to eye safe limit. Either because of the limited laser power, or because of high power-induced non-linear effects in the waveguides. Once coupled into free space, the optical signal propagates toward the target, experiencing free-space path loss. This includes the diffraction which contributes to the inverse square distance factor in the LiDAR equation (Eq. 4.11). The light can also be scattered by the atmosphere, which is a phenomenological parameter that we will not discuss here.

Upon reaching the target, which is typically modeled as a Lambertian scatterer, where the signal gets further attenuated because only a portion of the optical power is reflected back to the receiver. A common approximation assumes a target reflectivity of 10% for the receive angle aligned with the transmit angle. Solar spectrum irradiance represent a source for background noise that can enter the coherent detector and mix with the local oscillator or with itself [93].

The return signal then propagates back through the same optical path and enters the receiving aperture. Reception introduces additional challenges, including polarization misalignment and wavefront distortion. These factors collectively affect the coupling/mixing efficiency of the returning light into the receiver. Assuming monostatic single aperture, the light would pass through the same antenna efficiency, aperture fill factor and distribution network losses. In addition, a monostatic configuration has the extra challenge of dealing with back reflections from the transceiver circuit as they can have much higher power compared to the return signal [94].

Electronics

Finally, the received signal is mixed with the LO signal to generate the RF beat signal. The electronics bandwidth should be high enough to detect the beat signal which is usually in the MHz scale. The analog signal is then converted into a digital signal using an ADC.

It is essential to ensure that the digital signal processing stage does not impose a stricter limit than the analog domain as follows. In the analog domain, range resolution is fundamentally limited by the chirp bandwidth. In the digital domain, the range resolution can be considered as the ability to distinguish two consecutive FFT peaks [95].

The range resolution can be further constrained by the discretization of the FFT, where the bin width determines the ability to resolve closely spaced targets. For a fixed number of FFT bins N_{FFT}, reducing the sampling rate improves the range resolution. However, the maximum range is set by the maximum beat frequency, which in turn depends on the sampling frequency. Consequently, improving resolution without increasing N_{FFT} reduces the maximum measurable range.

4.4 Beam steering and FMCW ranging with a single wavelength variable

4.4.1 FMCW signal generation

The methods used in literature to generate the FMCW signal in semiconductor lasers can be broadly categorized into external modulation of a single wavelength laser, or the use of a tunable laser. The key distinction between the two approaches lies in the domain where the frequency sweep is generated. In the external modulation approach, the chirp is first created in the electrical domain and subsequently imposed onto the optical carrier, whereas in the tunable laser, the frequency chirp is generated in the optical domain.

External modulation

In external modulation, one begins with a narrow-linewidth continuous-wave (CW) laser at a fixed wavelength and modulate it externally. Using an electro-optic modulator, an RF frequency chirp is applied to shift the optical carrier frequency in time. The resulting optical frequency sweep inherits its chirp characteristics

directly from the applied RF signal. However, the electro-optic modulators create two sidebands in the optical spectrum. That is why an in-phase/quadrature-phase (I-Q) electro-optic modulator configuration is usually used to suppress the carrier and the unwanted sideband, creating a single side-band signal. While this approach conveniently decouples the laser from the chirp generation, allowing the use of stable, narrow-linewidth lasers, it also requires high-bandwidth electronics for the RF signal generation. This makes it more suitable for proof-of-concept demonstrations [94, 96, 97].

Tunable laser

The most basic approach to the tunable laser involves direct frequency tuning through modulation of the injection current of a single-wavelength semiconductor laser, such as distributed feedback (DFB) or distributed Bragg reflector (DBR). Changing the current alters both the carrier density and the junction temperature, which in turn modifies the refractive index of the active region. This shifts the lasing frequency continuously, producing the desired chirp over a small wavelength range. Maintaining a narrow linewidth with highly linear chirp remains a challenge, with various approaches to handle it are shown in literature such as pre-distortion [98] or opto-electronic feedback [99, 100].

Swept source

Laser-based ranging encompasses a variety of applications beyond FMCW LiDAR, one of the most prominent being frequency-domain optical coherence tomography (FD-OCT) [101, 102]. FD-OCT enables three-dimensional reconstructions of biological tissue with spatial resolutions on the order of a few tens of micrometres. FD-OCT relies on the same fundamental principle as FMCW LiDAR, namely encoding depth information into the frequency domain by sweeping the source wavelength and analyzing the resulting interference signal.

FD-OCT, however, typically demands a much broader tuning range because achieving sub-millimeter range (axial) resolution requires high optical bandwidths, often approaching 100 nm, together with rapid wavelength sweeps. Lasers meeting these requirements are referred to as wavelength-swept sources, denoting their capability for wide, continuous tunability combined with fast periodic modulation of the instantaneous optical frequency [103]. Unlike LiDAR, the coherence length requirement in OCT is modest, as light generally travels only a few centimeters within the biological tissues.

For lasers intended as swept sources for FMCW ranging, several features

must be simultaneously optimized: narrow optical linewidth, continuous and wide wavelength tunability, highly linear frequency chirp, and fast sweep rate (i.e., high frequency agility). Current demonstrations enabling laser-based ranging [99, 104–107] typically excel in some of these aspects but seldom achieve all of them in a single device.

4.4.2 Concept

Consider a simplified LiDAR system employing a generic beam steering engine. As discussed previously, the beam steering device must scan the entire scene within a time window equal to the frame time specification. Simultaneously, to achieve FMCW ranging, one can use a tunable laser with a chirp rate $\gamma = \frac{\Delta f_{chirp}}{T_{chirp}}$, as described in section 4.1.1, and illustrated in Fig. 4.8(a). The chirp bandwidth Δf_{chirp} is selected according to the desired range resolution, following Eq. 4.13. The chirp time T_{chirp} should be sufficiently long so that each pixel (angle) in the scene is illuminated for enough time to (i) allow the signal to propagate to the farthest target and return, and (ii) permit adequate signal integration to meet the required signal-to-noise ratio (SNR), as described by equation 4.9. In other words, the following condition should hold:

$$T_{chirp} >> T_{return\,max}, \tag{4.19}$$

where $T_{return\,max}$ is the round-trip time from the maximum measurement range. A common rule of thumb in radar systems [108] is:

$$T_{return\,max} = 0.1\,T_{chirp}, \tag{4.20}$$

which reserves 10% of the chirp duration as dead time and leaves 90%, available for useful measurements. Thus, each pixel's measurement effectively starts after a delay of $0.1T_{chirp}$ within the illumination period. While the approximation of equation 4.8 can still be considered valid, the initial fraction of the chirp corresponding to $T_{return\,max}$ can be considered a dead zone for the measurement. This is because (i) the tail end of the return signal from the previous chirp may still overlap within this interval, and (ii) for the most distant targets, the return signal may not yet have arrived.

Ranging with swept source

Equivalently, one can also use a swept source, despite the additional technical challenges associated with its realization. Conceptually, this approach can be viewed as unwrapping the triangular waveform into a purely linear frequency-time

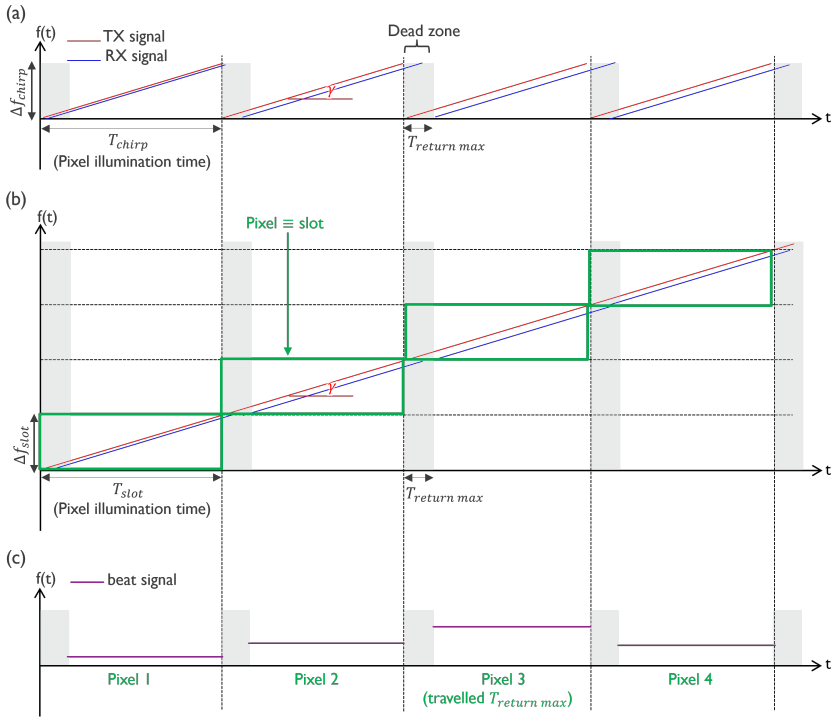

Figure 4.8: FMCW waveforms (not to scale): (a) Triangular FMCW chirp, showing a dead time equal to the maximum return time $T_{return\ max}$; (b) The swept source signal equivalent to the triangular signal of (a), where the laser sweep is divided into slots, to address each far field pixel; (c) The corresponding beat signal.

relationship, as shown in Fig. 4.8(b). At any point in time, the instantaneous frequency of the transmitted laser signal is:

$$f(t) = \frac{\Delta f_{sweep}}{T_{sweep}} t + f_0, \tag{4.21}$$

where f_0 is the initial frequency, Δf_{sweep} is the total tuning bandwidth, and T_{sweep} is the total tuning period.

The mixing between the local oscillator and the receiver signal is performed continuously. The swept source signal is then divided into N_{pixels} slots, i.e. corresponding to the number of addressed far field pixels, where the frequency bandwidth of the slot is Δf_{slot}, and the time duration of the slot is T_{slot}. The chirp rate can be equivalently calculated from the slot or from the total sweep: $\gamma = \frac{\Delta f_{slot}}{T_{slot}} = \frac{\Delta f_{sweep}}{T_{sweep}}$. The FFT operation to obtain the beat signal is performed at each slot, where Δf_{slot} corresponds to the chirp bandwidth required for the range resolution, as shown in Fig. 4.8(b). All the concepts that we introduced so far apply to our system.

So far, if we assume as first calculation that each frame corresponds to a single upward sweep, the laser sweep is constrained by:

- Δf_{slot} to achieve the range resolution requirement.
- ΔT_{slot} to achieve the SNR requirement.
- Δf_{sweep} to cover all the scene pixels (N_{pixels}), where $\Delta f_{sweep} = N_{pixels} \,.\, \Delta f_{slot}$.
- T_{sweep} to achieve the frame time requirement, where $T_{sweep} = N_{pixels} \,.\, T_{slot}$.

Dispersive beam steering with swept source

Up to this point, the discussion has been independent of the specific beam-steering mechanism. Let us now focus on spectral/dispersive beam steering, in which the steering angle is governed by the optical wavelength. The beam steering device can, for example, be the dispersive optical phased array (DOPA) introduced in the previous two chapters. DOPAs steer the beam as a function of frequency and therefore also as a function of time when driven by a wavelength-swept laser.

In such a configuration, as the laser is swept to perform FMCW ranging, the beam is simultaneously steered in the far field as a function of the instantaneous laser frequency $f(t)$. This concept is not entirely new, in fact, a few demonstrations

showed the swept-source LiDAR, where discrete components for wavelength-based beam steering are used, such as [95, 109, 110].

In this type of system, the building blocks get simplified and some of the design parameters of the scanning and ranging become interdependent which leads to new constraints and trade-offs that must be carefully managed.

4.4.3 Constraints

Sweep bandwidth and number of scan lines

This is the most straightforward constraint of the system. The laser sweep bandwidth of the ranging engine Δf_{sweep} should match the wavelength tuning range of the beam steering engine used in equation 2.22 to be able to scan through the whole 2D field of view.

Angular resolution and range resolution

Within a slot, the wavelength tuning range $\Delta\lambda_{slot}$, corresponding to the chirp bandwidth Δf_{chirp} in the frequency domain, would slightly move the far field angle in the fast scanning axis θ_x. The angle moves by an increment $\Delta\theta_{x,slot} = \frac{d\theta_x}{d\lambda} . \Delta\lambda_{slot}$, where $\frac{d\theta_x}{d\lambda}$ is defined by equations 2.20 and 2.21.

Consequently, if the scan rate in the fast axis $\frac{d\theta_x}{d\lambda}$ (due to differential delay length) is too high, the frequency chirp Δf_{chirp} required for ranging could move the spot away from the desired pixel. Additionally, for the pixelated DOPA, this bandwidth can be enough to move further away from the constructive interference condition, where the spot intensity is reduced and diffraction orders rise, which will be discussed further in section 4.5.3.

Generally, the angular deviation $\Delta\theta_{x,slot}$ resulting from the FMCW chirp should be smaller than the beam steering angular resolution requirement. The maximum possible chirp bandwidth becomes smaller as the differential delay increase, or equivalently as more scan lines are targeted.

Slot time and return time

If light reflects from multiple targets within a given frequency slot, the FFT of the signal exhibits multiple peaks, each corresponding to a target's range. This situation could happen when returns from previous slots (previous wavelengths/beam angle

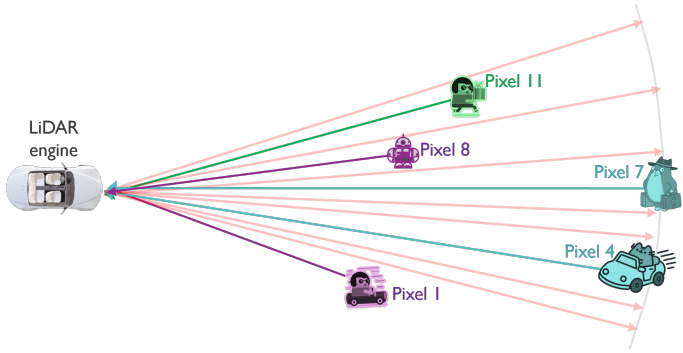

Figure 4.9: LiDAR scene corresponding to the return signals in figure 4.10.

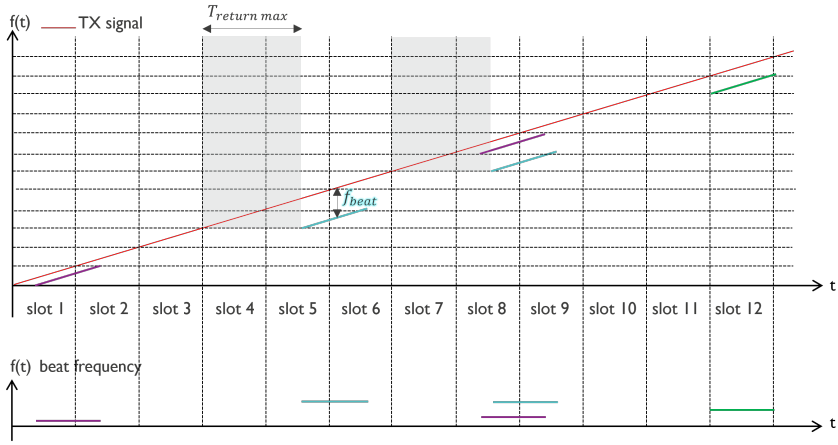

Figure 4.10: Corner cases associated with FMCW LiDAR with a swept source and DOPAs for the case of $T_{slot} < T_{return\ max}$, where the top plot shows the return signals in each slot corresponding to the scene in Fig. 4.9. The bottom plot shows the equivalent beat signals.

settings) are received. This effect is characteristic of passive dispersive OPAs, in contrast to their active counterparts, as explained below.

For active OPAs, at a point of time, the phase shifters of the OPA are in a state to point to a single direction. Consequently, the array transmits and receives only from that direction during that interval. For each direction, the phase shifters must first be reconfigured to direct the beam appropriately. Once the desired direction is set, the laser chirp is performed. The chirp time should be enough to allow the signal to return from the maximum range and be integrated over a sufficient time window to achieve the required SNR, as described by the formulas 4.19 and 4.20. After completing the chirp for one direction, the OPA is reconfigured to the next

angle, and the process repeats.

In this scheme, the frame rate is limited by two factors: the phase shifter switching time required to reconfigure the OPA for each angle and the chirp duration needed for reliable range measurements.

On the other hand, dispersive OPAs can receive and transmit their angle-wavelength combination at any point of time. In this case, we are in front of two possibilities for the dispersive OPA with a swept source.

Conventional slot timing

The first possibility is to set the chirp time of the slot T_{slot} similar to the convention, as described by the formulas 4.19 and 4.20. In this case, within a frequency/time slot, return signal that couple into the interference signal from previous slots would have a beat frequency higher than the frequency expected from the maximum range and can be removed using low-pass filtering during data processing.

Relaxed slot timing for higher frame rates

The second possibility is to allow the signal to return back to a later slot than that where it was transmitted. The slot time can then be shortened, $T_{slot} \geq T_{return\,max}$, or even $T_{slot} < T_{return\,max}$ [111], as shown in Fig. 4.10, allowing potentially higher frame rates. The constraints and consequences of this approach need to be studied, which is beyond the scope this thesis, however, some first thoughts are mentioned in the following lines.

Firstly, the slot time needs to be long enough for the SNR requirement. It should take into account the corner cases where the return signal is in-between slots that the integration time is not enough per slot, an example of this case is shown in Fig. 4.10(a) for the signal that is received within slot 5 and 6.

Additionally, the maximum beat signal frequency will be higher than the first possibility, so the electronics and signal processing should be able to detect such high frequencies, and be able to estimate the frequency of multiple beat signal from multiple return signals, as in the signals that are received within slot 8 and 9 in Fig. 4.10(a), which falls under the multiple tone frequency estimation problem [112].

Finally, to reconstruct the scene accurately, each return signal must be uniquely identifiable so it can be associated with the wavelength, and therefore the angle of emission. The wavelength can be estimated from the beat frequency as it provides the time delay information. The time of emission and the corresponding wavelength can then be back-traced, which would require some extra processing.

4.4.4 Multiplexed ranging engines

Let's recall the pixelated DOPA architecture from chapter 2. The architecture consists of a set of M blocks of continuous DOPA, where the light is distributed to the blocks via a $1 \times M$ light splitting network. The light splitting network can be implemented in various ways. A common approach is a cascaded tree of 1×2 multimode interference (MMI) splitters, which was the method used in the demonstration of chapter 3. The splitting function can also be realized by a star coupler.

Light distribution using a star coupler

A star coupler is composed of a slab diffraction region, also referred to as free propagation region, that separates an array of N input waveguides from an array of M output waveguides [113], as shown in Fig. 4.11(a). In the context of a pixelated DOPA, each output channel of the star coupler is routed to one of the M blocks of the pixelated DOPA. A star coupler can be designed to have the following behavior. The output waveguide array lies in the far field of the input waveguide array. Each of the input and output waveguide array lie on the perimeter of two different circles. The separation between the center waveguide and any waveguide on the output array is R which is the focal length of the star coupler The light diffracting from any input channel has a circular wavefront, where the power is uniformly distributed over the output channels. Note that the star coupler can also be designed to have a Gaussian distribution on the output channels.

For each input channel, the light impinging on the output channels has a small fixed phase difference for each consecutive channels. For the center input channel, this phase difference is zero. If only the central input waveguide is excited, the star coupler effectively functions as a splitter tree, aside from the differences in insertion loss and bandwidth.

Wavelength multiplexing using a star coupler

What happens then when the off-center input channels of the star coupler are used? This requires re-evaluating the constructive interference condition discussed in equations 2.29 and 2.30, taking the number of blocks (star coupler output channels) as M and the phase difference between consecutive output channels of the star

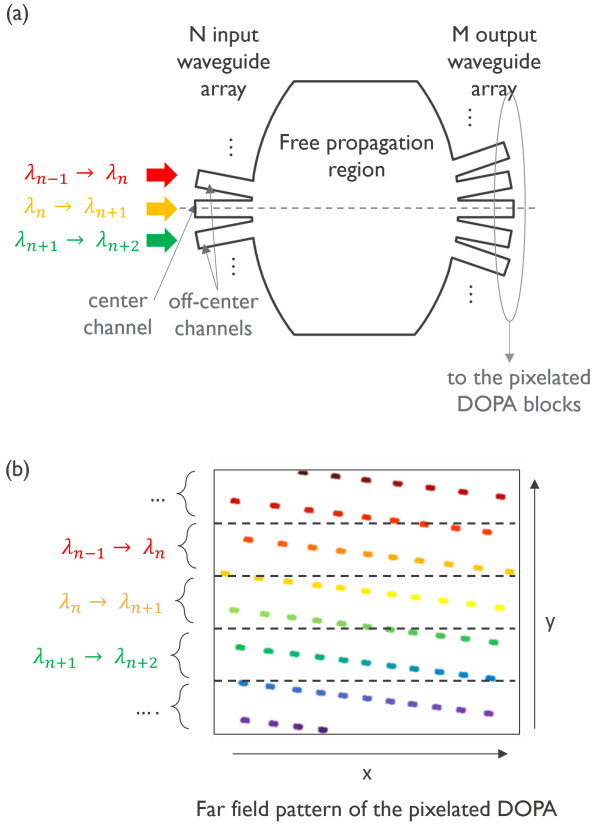

Figure 4.11: Wavelength multiplexing using a star coupler: (a) Basic star coupler geometry; (b) Each of the input tunable lasers to the star coupler sweep through a subset of the full far field.

coupler as $\Delta\phi_{SC}$:

$$\begin{aligned} \phi_{N'_x+1} - \phi_{N'_x} &= \Delta\phi \pm m \cdot 2\pi \\ M.\Delta\phi_{SC} - [(M-1).\Delta\phi_{SC} + (N'_x - 1)\Delta\phi] &= \Delta\phi \pm m \cdot 2\pi \\ N'_x\Delta\phi &= \pm m \cdot 2\pi + \Delta\phi_{SC} \\ N'_x \frac{\Delta L.n_{eff}(\lambda)}{\lambda} &= m + \frac{\Delta\phi_{SC}}{2\pi} \end{aligned} \tag{4.22}$$

The constructive interference between the blocks occurs at specific wavelengths:

$$\lambda_m = \frac{N'_x}{m + \frac{\Delta\phi_{SC}}{2\pi}} \,.\, \Delta L \,.\, n_{eff}(\lambda), \tag{4.23}$$

where m has a very large value as mentioned in chapter 2, and $\frac{\Delta\phi_{SC}}{2\pi} < 1$. This means that the constructive interference wavelengths will be very slightly shifted from the case of the balanced splitter tree. This does not pose an issue as long as the wavelengths and their corresponding far field locations are well-known.

Thus, instead of using only a single input channel of the star coupler, one can use multiple input channel with the pixelated DOPA. Each of the input channels can be connected to a different tunable laser, where each tunable laser has a wavelength band that is a subset of the full wavelength range required for the beam steering. Consequently, each laser wavelength band will sweep through a subset of the overall far field as shown in Fig. 4.11(b). In other words, the star coupler can be used as a wavelength multiplexer [114, 115], where by operating the lasers simultaneously, multiple far field points can be addressed simultaneously.

Multiplexed ranging engines using a star coupler

Considering the full LiDAR system, instead of being connected to only a tunable laser, each of the input ports of the star coupler can connected to an independent FMCW ranging engine, where a monostatic configuration is used, as shown in Fig. 4.12. Each engine incorporates a tunable laser that spans a specific sub-band of the total wavelength range.

This approach enables simultaneous addressing of multiple pixels, effectively increasing the integration time per pixel without compromising the frame rate. The extended measurement duration per pixel reduces the required receiver sensitivity needed to reach the target $SNR_{threshold}$, which will be more clear in the case study of section 4.5. An additional advantage of the monostatic configuration with DOPAs is that it offers high selectivity, not only due to coherent detection, but also due to the selectivity of the DOPA to only one wavelength for a specific far field receive angle.

On the other hand, a monostatic configuration is particularly sensitive to optical back-reflections, which can degrade the performance of the ranging engine through two distinct mechanisms. The first mechanism affects both monostatic and bistatic configurations: back-reflections can re-enter the laser cavity and form optical feedback, thereby deteriorating the laser performance. In the present context, this deterioration may be observed as linewidth broadening due to increased frequency noise, mode hopping, and distortion of the frequency chirp. The exact level of feedback suppression required depends on the laser design and the application requirements, and is therefore beyond the scope of this thesis. Nevertheless, this effect is especially critical when considering integrated laser sources, since practical on-chip optical isolators are not yet available.

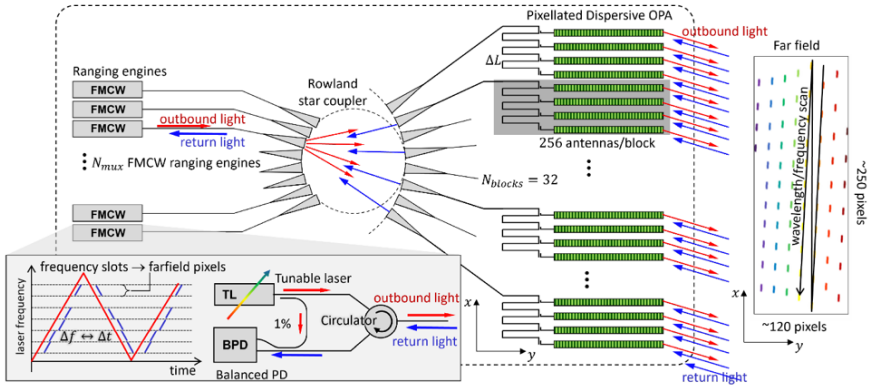

Figure 4.12: Beam steering and FMCW ranging with a single wavelength variable system incorporating a 2D pixelated DOPA beam scanner with multiplexed FMCW ranging engines. A wavelength-swept source drives both the beam steering and ranging functions. Multiple FMCW engines feed the star coupler input ports, allowing simultaneous addressing of multiple far field pixels, figure from [114].

The second mechanism is specific to the monostatic configuration. In this case, back-reflected light can reach the balanced photodetector directly, where it mixes with the local oscillator signal and produces an undesired beat note. Because these reflections typically experience very short delay times, the resulting beat frequencies are usually low and can, in principle, be suppressed using high-pass filtering. However, when the reflected light undergoes multiple reflections within the optical system, the effective delay increases, potentially shifting the beat frequency into the signal band of interest. This results in spurious tones that degrade the signal-to-noise ratio (SNR). Such beat signals can also impose an upper limit on the optical power that can be injected into the circuit to improve the SNR. This is because increasing the input power proportionally enhances the beat notes induced by backreflections, which in turn reduces the SNR, as reported in [22].

A summary of the updated design space, involving pixelation and multiplexing, demonstrating the coupling between the ranging and steering parameters is shown in Fig. 4.13

Laser control

At this stage, it is important to emphasize the extent to which beam steering and FMCW ranging with a single wavelength variable approach shifts a significant portion of the system complexity from the photonic circuit to the laser control and

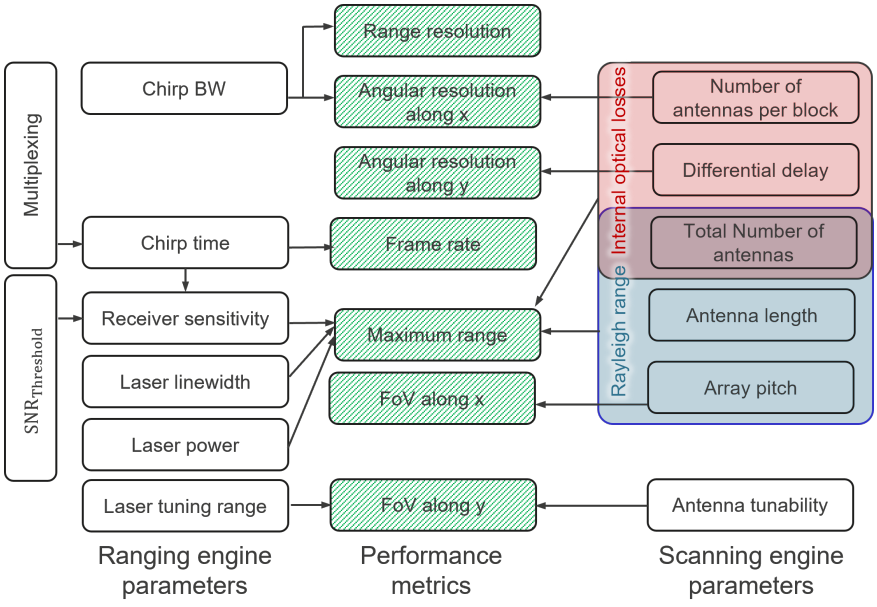

Figure 4.13: Design space of beam steering and FMCW ranging with a single wavelength variable, including pixelation and multiplexing concepts.

monitoring. This relevance can be examined from two complementary perspectives: beam steering and FMCW ranging.

From the beam-steering standpoint, the steering angle is a function of the optical wavelength. Consequently, the angular accuracy is governed not necessarily by the accuracy of the wavelength tuning itself, but rather by the accuracy with which the instantaneous emission wavelength is known. This relaxes the requirements on laser control, provided that accurate real-time wavelength monitoring is available. In this context, the integration of on-chip wavelength monitoring elements becomes particularly important. Integrated wavelength meters, for instance based on optical hybrid structures, can offer a scalable and compact solution for real-time wavelength tracking.

From the FMCW ranging perspective, the general requirements imposed on the laser source, are discussed in Sections 4.3 and 4.4.1. However, considering the requirements on the laser control, the key relevant parameter is the chirp linearity. Chirp nonlinearity broadens the beat spectrum and degrades the achievable range resolution beyond the theoretical limit set by the chirp bandwidth [92]. In the case of using a widely tunable laser or a swept source, the use of multiplexed ranging engine reduces the tuning range per laser which can simplify the laser control problem.

4.5 Case study of pixelated DOPA with FMCW ranging

Consider a DOPA designed on a platform with the waveguide parameters listed in Table 4.1. The table also shows the key beam steering engine design parameters and the corresponding performance metrics. We will explore some of these design parameters and link them to the ranging engine in the following subsections.

4.5.1 Insertion loss and number of far field pixels

The combination of the array pitch and the number of antennas yields an aperture size that is large enough to have the Rayleigh range along the x-axis at 200 m. If a continuous DOPA is used, then this yields a resolution along the x-axis of approximately 0.003°. However, the requirement for the angular resolution along x-axis is 0.1°. This corresponds to 250 pixels per scan line if we would use the pixelated DOPA, which corresponds to dividing the distribution network into 64 blocks. In this example, we work with the unbalanced tree architecture, so the

Parameter	Value	Target metric	Value
Center wavelength	1550 nm		
Wavelength tuning range	100 nm		
Waveguide loss	0.2 dB/cm		
Waveguide effective index	2.4		
Waveguide group index	4.5		
Total number of antennas	8192	Rayleigh range	200 m
Array pitch	3.47 µm	FOV along x	25°
Delay line length	634 µm	Resolution along y	0.1°
Grating dispersion	0.12 ∘/nm	FOV along y	12°
Grating length	28.5 mm	Rayleigh range	200 m
Number of blocks	32	Resolution along x	0.1°

Table 4.1: Example design parameters of a pixelated DOPA.

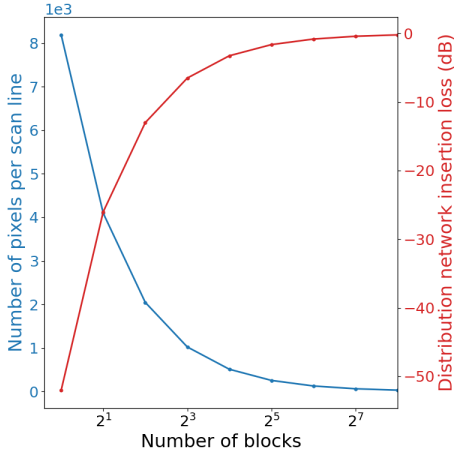

Figure 4.14: As the number of blocks increase, the number of far field pixels per scan line decreases and the delay lines distribution network insertion loss decreases. The values are based on the unbalanced splitter tree architecture with the design parameters of Table 4.1. The splitters insertion loss is neglected in this calculation.

number of antennas and number of antennas per block are powers of 2.

The calculation of the total loss $Loss_{tot}$ follows:

$$Loss_{tot}[dB] = M\,.L_{block}\,.Loss_{wg}, \tag{4.24}$$

where $Loss_{wg}$ is the waveguide loss in [dB/cm] and L_{block} is the total length of delay lines per block in [cm]. The total length of delay lines per block can be calculated using equation 2.26. The corresponding insertion loss of the distribution network waveguides is then approximately −1.62 dB, as shown in Fig. 4.14. As expected, without pixelation , i.e. number of blocks = 1, the insertion loss is worse than −50 dB. Thus, the number of blocks directly influences both the total number of far field pixels and the insertion loss of the distribution network.

4.5.2 Receiver sensitivity and LiDAR equation and Maximum range

Let's now move to the ranging engine. Considering that $SNR_{threshold}$ is a fixed parameter to achieve a reliable ranging, for example 13.2 dB, Eqs. 4.17 and 4.11 show that there are three factors to be co-optimized; that is the transceiver design to maximize the power at the receiver, the measurement bandwidth (time) and the maximum range. Let's consider that the required frame rate is 25 Hz (40 ms per frame), and the available photodetector on the platform has responsivity of 0.8 A/W.

Parameter	**Value**
$SNR_{threshold}$	13.2 dB
Frame rate	25 Hz
Responsivity	0.8 A/W
Target reflectivity	10%
Receive efficiency	9.8%
Aperture size	30 mm

Table 4.2: Example parameters associated with the ranging engine.

Without multiplexing

Continuing with the same pixelated DOPA design, the total number of pixels is 30000. Consequently, the pixel measurement time is 1.33 µs to achieve the frame requirement. Then, the receiver sensitivity is 3.14 pW, according to Eq. 4.17.

As we use a monostatic configuration, we can start the LiDAR equation from the transmitter emitted power regardless of the transmitter circuit loss. The contribution of the OPA losses will be taken into account in the receive path. In this particular analysis, the emitted power is set to the eye safety limit (10 mW). Atmospheric losses are neglected ($\eta_a = 1$) and the target reflectivity in the direction of the receiver circuit is 10 % ($\rho(\pi) = 0.1$).

Since we work with inline photodetectors in our integrated photonic platforms and a monostatic configuration for the transceiver, then we we can make first approximation for the mixing efficiency. The mixing efficiency is taken as 100 %, but we account for receive efficiency η_r as the efficiency of coupling from free space to the antenna array, and is calculated as:

$$\eta_r = \eta_{ant} \frac{2.78\lambda}{2\pi p_x}, \tag{4.25}$$

where η_{ant} is the individual grating emission efficiency, p_x is the antenna array pitch. Note that the polarization misalignment, deviations from Gaussian beam, reduction of useful signal due to phase errors are not taken into account. Taking the grating efficiency to be 0.5, the receive efficiency becomes 9.8 %. The distribution network loss is approximately 2 dB, based on the degree of pixelation.

Substituting these values in Eq. 4.11, the maximum range is then limited to approximately 100 m, as shown in Fig. 4.15. The large number of antennas was originally chosen to achieve the maximum range of 200 m. The pixelation has reduced the insertion loss significantly, but the very short measurement time is still limiting the maximum range.

With multiplexing

If a star coupler is used for light distribution to the blocks, a multi-input star coupler can be used. In this example, we use a 32 $\times$ 32 coupler. Note that there no strict requirement to use a symmetric star coupler. Each input can be connected to one of 32 FMCW ranging engines. In this case, the measurement time for a single pixel can go up to 43 µs. The receiver sensitivity is then 0.097 pW, and the maximum range can be more than 200 m. It is noted that the measurement time needed for 200 m is 5 µs. However, there are many losses along the path that were not accounted for in the first approximation (e.g. bad weather). Therefore, maintaining a sufficient margin above this estimate is a reasonable approach.

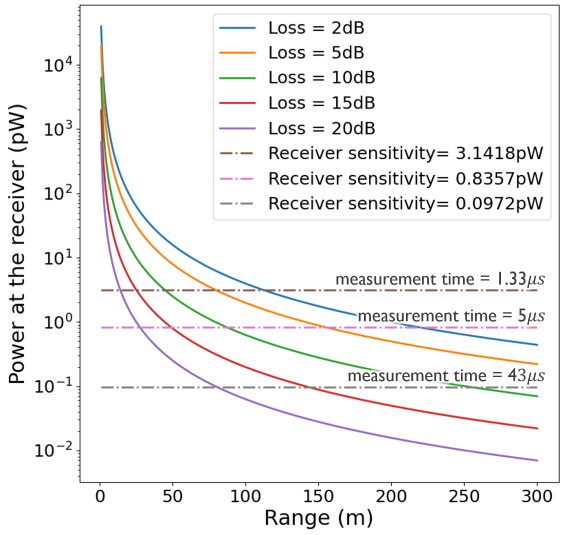

Figure 4.15: Power at the receiver versus range for different values of distribution network loss, based on the parameters in tables 4.1, 4.2.

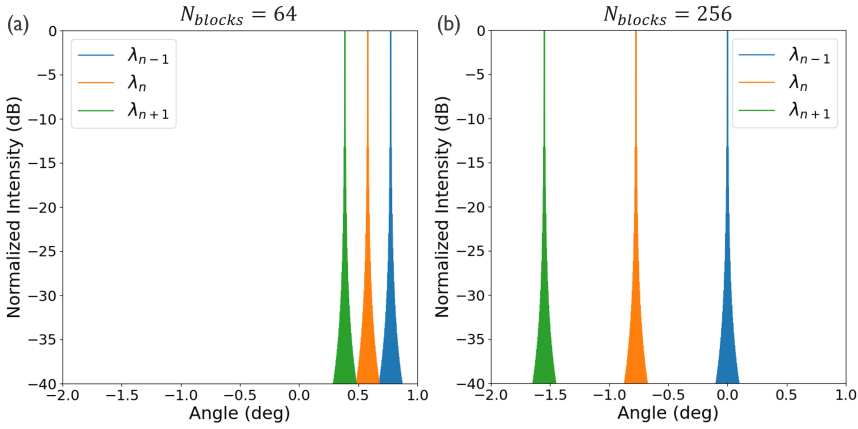

Figure 4.16: The array factor of three of three adjacent pixels of the pixelated DOPA of Table 4.1, for (a) 64 blocks, (b) 256 blocks.

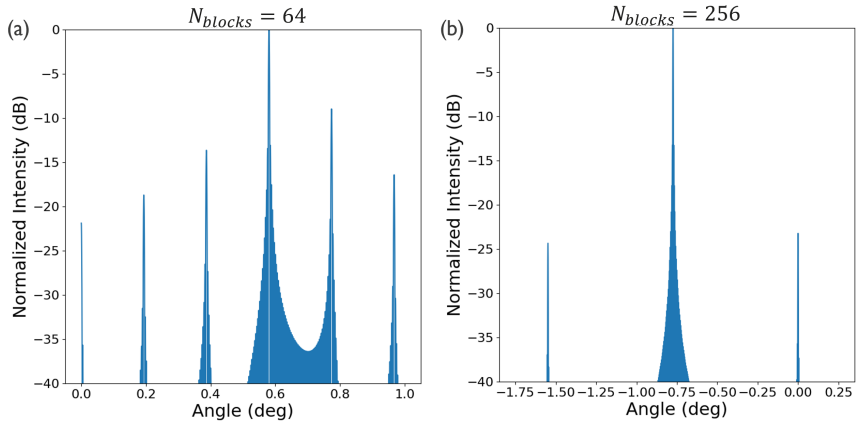

Figure 4.17: The array factor of at wavelength of (λ_n - 3 pm), for (a) 64 blocks, (b) 256 blocks.

4.5.3 Angular resolution and range resolution

The pixelated approach requires further consideration when approaching the chirp bandwidth, and hence the range resolution. Consider three consecutive operation wavelengths that satisfy the constructive interference condition of the pixelated DOPA, corresponding to three spatially adjacent far field pixels, as shown in Fig. 4.16. For a uniform power distribution across the antennas, the array factor at these wavelengths exhibits a theoretical SLSR of 13.2 dB.

Focusing on the wavelength λ_n in Fig. 4.16(a), a range resolution of 15 cm requires a chirp bandwidth of 1 GHz, Eq. 4.13, equivalent to a wavelength range of approximately 7.6 pm around λ_n. Within this range, prominent side lobes appear at the angles of neighboring pixels, arising from the diffraction orders of the blocks, as shown in Fig. 4.17(a). This causes the SLSR to fall well below 13 dB, degrading the performance relative to a continuous DOPA Fig. 4.18(a).

Reducing the chirp bandwidth to 0.5 GHz, about 3.3 pm around the center wavelength, corresponding to 30 cm range resolution, restores the SLSR above 13 dB, Fig. 4.18(a). Alternatively, increasing the number of blocks to 256 decreases the far field pixel count, Fig. 4.16(b), but allows an SLSR above 13 dB for 15 cm range resolution, Fig. 4.18(b).

These results indicate that in a pixelated DOPA, the full interpixel bandwidth cannot always be used without SLSR degradation, Fig. 4.19. A robust design strategy should therefore balance: (1) the number of blocks to prevent SLSR collapse within

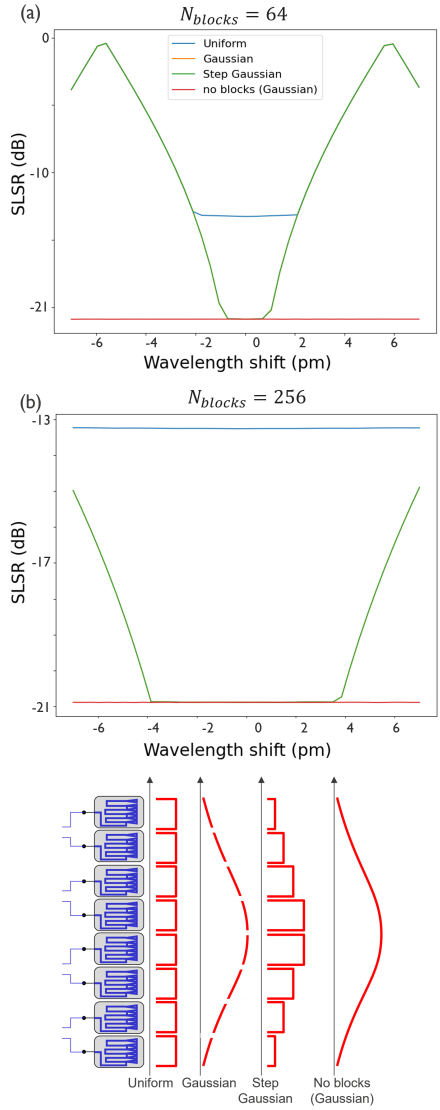

Figure 4.18: SLSR at different wavelength shifts from λ_n, using different input power profile to the aperture, for (a) 64 blocks, (b) 256 blocks.

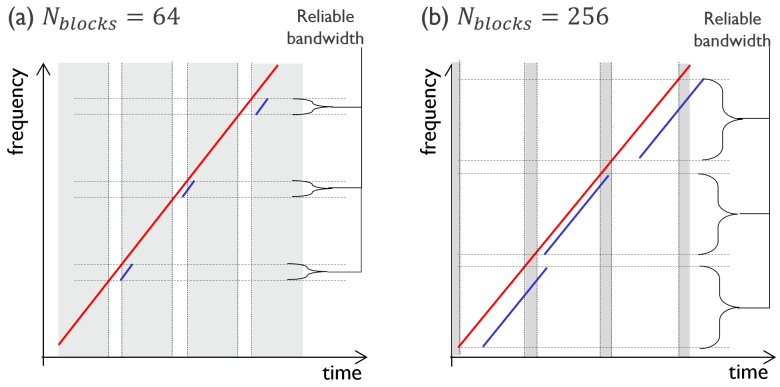

Figure 4.19: A sketch of a frequency sweep across three adjacent pixels, where low SLSR in the pixelated DOPA prevents full utilization of the interpixel bandwidth (not to scale). Increasing the block count degrades angular resolution but yields acceptable SLSR within a larger bandwidth. The figure compares (a) 64 blocks to (b) 256 blocks.

a frequency slot while keeping insertion loss and number of pixels acceptable, and (2) the range resolution matching the angular resolution requirements.

5

Medium-scale multiplexed pixelated DOPA with FMCW ranging

In this chapter, we construct a fully photonic integrated system for FMCW LiDAR. The system is based on a wavelength-multiplexed pixelated dispersive optical phased array with FMCW ranging in a monostatic configuration. The chip incorporates a beam steering circuit based on a 512-channel dispersive optical phased array, and an integrated ranging circuit including on-chip Germanium photodetectors and on-chip lasers based on transfer printed semiconductor optical amplifiers (SOAs). The connection between the beam steering circuit and the ranging circuit is based on a star coupler that allows multiple inputs to the optical phased array. We examine the functionality of the subcircuits and some of their building blocks. The chapter also aims to walk the reader through the design steps starting from the first schematics up to some insights into the device packaging. Due to the time limit of the PhD work and the set of issues that need to be dealt with before even demonstrating the beam steering of the device, the demonstration of the full system operation is left as a future work.

The work in this chapter involves multiple contributions from colleagues whose efforts are acknowledged. Thanks to Huaqing Qiu for providing the antenna design, to Jing Zhang for providing the laser design, to Michał Golas for the PCB design, to Yu Zhang for performing the fiber attach process, to Adam Barzanji and Michał Golas for working on the phase calibration and the thermal packaging.

5.1 System overview

In this system design, we continue to adopt a bottom-up design methodology, as in the designs presented in Chapter 3, with the goal of presenting a larger scale demonstration incorporating all relevant building blocks on a single chip. An overview of the system is presented in Fig. 5.1. This section provides a brief introduction to the overall system, with detailed descriptions of its subsystems provided in the following sections.

The system is composed of two main circuits: a beam steering circuit and a ranging circuit. The beam steering circuit is based on the pixelated DOPA concept. Light is coupled into the distribution network through a multi-input star coupler, which feeds individual blocks of the pixelated DOPA. The output of the distribution network is routed to the antenna array via a fan-in structure to accommodate the difference in pitch between the distribution network outputs and the antenna array elements. The multi-input design of the star coupler enables flexible operation. Certain inputs are directly connected to grating couplers, allowing the beam steering circuit to be driven by external lasers, while others interface with the ranging circuit. The

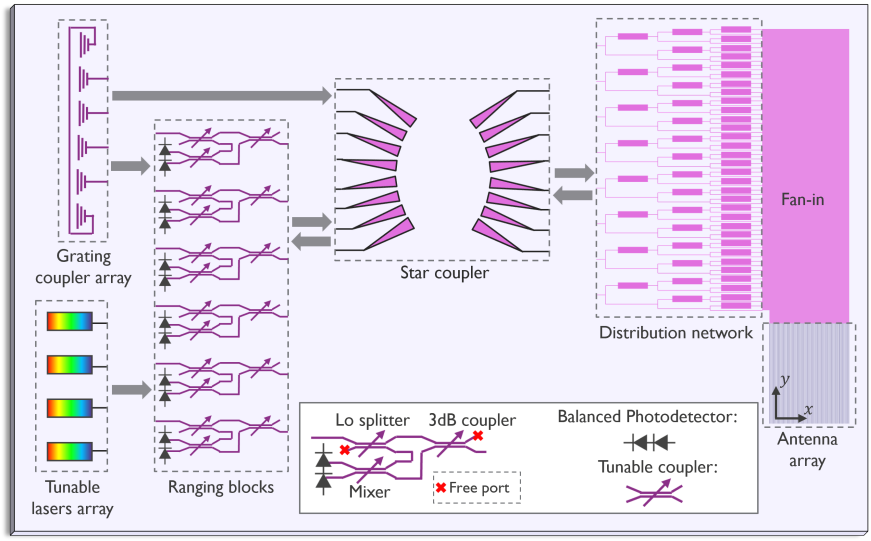

Figure 5.1: Conceptual illustration of the system implemented in this chapter. The system is based on wavelength-multiplexed pixelated dispersive optical phased array with FMCW ranging in a monostatic configuration. Note that the building blocks size is not to scale.

ranging circuit comprises a dedicated ranging block that can be driven by either an on-chip laser or an external laser coupled through grating couplers. The overall system is implemented in a monostatic configuration, in which the pixelated DOPA serves as both the transmitter and receiver. The choice of a monostatic configuration is due to the predominantly passive nature of the circuit, even if a limited number of calibration phase shifters is used to correct for phase errors. Employing two separate DOPAs for transmission and reception would complicate the alignment, as post-fabrication variations between the two circuits would make calibration and the additional task of alignment highly challenging.

This design is implemented using imec's iSiPP50G platform [117], as shown in Fig. 5.2. We rely entirely on the silicon-based building blocks, so we expect that we are challenged in terms of losses and phase errors. Additionally, developing a fully functional integrated system is inherently high-risk, thus, while the overall system architecture is ambitious, conservative choices were deliberately made in smaller design decisions to manage the system complexity. The system was designed in a modular approach, with functional blocks isolated and accessible through the grating coupler array to simplify characterization and troubleshooting.

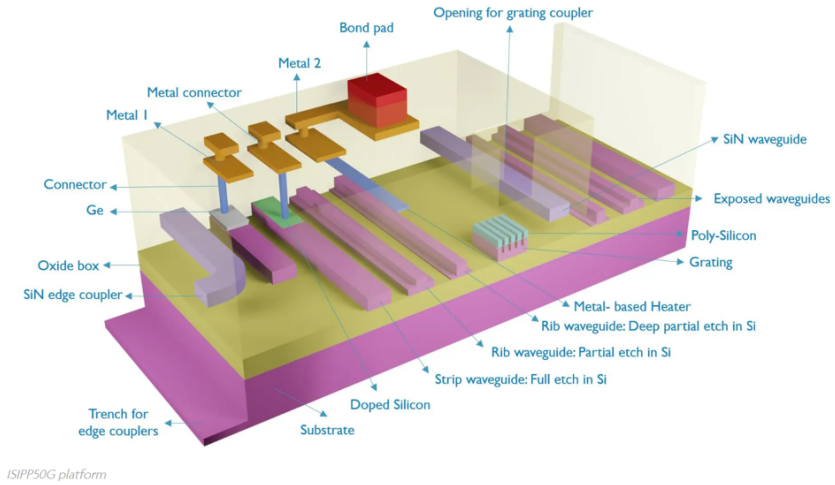

Figure 5.2: iSiPP50G platform, figure from [116].

WG specification	$N_{antennas}$ (N_x)	N_{blocks} (M)	$N_{scan\ lines}$ (N_y)	ΔL	Total loss
multimode Si, width = 1 μm, loss = 0.5dB/cm, n_{eff} = 2.77, n_g = 3.7.	256	8	16	205μm	7dB
			30	385μm	12dB
	512	8	16	206μm	16dB
			30	386μm	30dB

Figure 5.3: Delay lines loss for different combinations of distribution network parameters. The loss does not account for bend loss and MMI loss.

5.2 Beam steering circuit

5.2.1 Schematic

The unbalanced splitter tree architecture is used with the aim to have it in a more compact form than the demonstration of chapter 3. Due to the high propagation losses of single mode Si waveguides, the delay lines are based on multimode Si waveguides that taper into single mode Si bends, with bend radius of 10 μm. The single mode bends radiate away any possible higher order modes that can be generated in the multimode waveguides. The multimode waveguide width is 1 µm,

where effective index and group index of the ground mode are are 2.77 and 3.7, respectively. Multimode waveguides have less losses and phase errors. Based on previous measurement data, the waveguide loss of 1 μm-wide waveguide is better than 0.5 dB/cm.

The key parameters of the pixelated DOPA are the total number of antennas (N_x), the number of blocks (M), the differential delay length (ΔL), and the antenna array pitch (p_x). For the first three parameters, we calculate the resulting loss for different combination of the three parameters. For the unbalanced splitter tree in the pixelated variation, the calculation of the total loss $Loss_{tot}$ in [dB] follows:

$$Loss_{tot} = M \frac{N'_x . \log_2 N'_x}{2} . \Delta L . Loss_{wg}, \tag{5.1}$$

where $Loss_{wg}$ is the waveguide loss in [dB/cm] and N'_x is the number of antennas per block. The resulting total loss for different combinations of design parameters is shown in Fig. 5.3, where the delay line length is calculated from the number of scan lines N_y following Eq. 2.18 and Eq. 2.22. Eventually, the following combination is chosen: the total number of antennas is 512, the distribution network is subdivided into 8 blocks, and the differential delay length is approximately 200 μm. The loss of the distribution network would at least be 16 dB. The antenna array pitch is chosen to be 3 μm. The choice for the pitch is driven by the risk of cross coupling between the fan-in waveguides, which will be discussed in the layout subsection.

Antenna

The weak antenna design is based on sidewall corrugation of Si waveguide. The design parameters of the antenna are shown in Fig. 5.4(a), where the duty cycle is 50%. These design parameters provide the following performance metrics for the gratings. The antenna efficiency is approximately 50%. The antenna strength is approximately 7.15 dB/mm, resulting in an effective antenna length of approximately 2 mm. The scanning rate of the Si antenna is expected to be approximately 0.14 °/nm.

5.2.2 Relation to LiDAR performance metrics

A summary of the design parameters of the pixelated DOPA circuit is shown in Table. 5.1.

As will be discussed later in Section 5.2.3, the field of view (FoV) along the x-direction is primarily determined by the antenna pitch, which must be sufficiently large to avoid evanescent coupling between adjacent fan-in waveguides. A practical

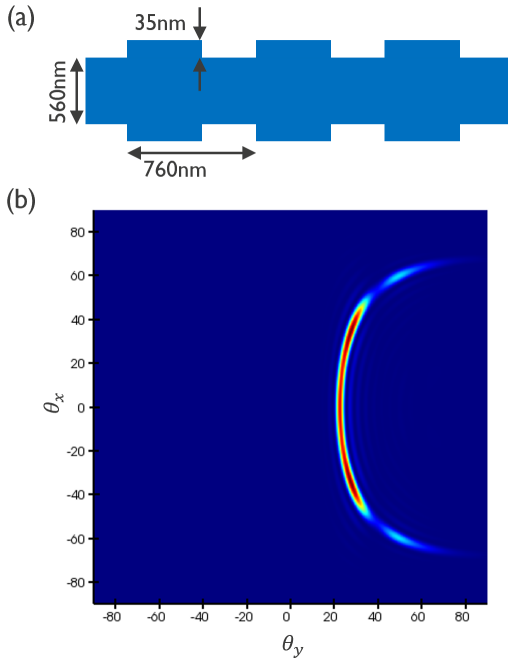

Figure 5.4: The Antenna used in the pixelated DOPA is based on the sidewall corrugation of Si waveguide: (a) Top view showing the geometrical parameters, (b) 2D emission profile in spherical coordinates.

approach to overcoming the resulting FoV limitation is to employ multiple OPAs. For example, using two OPAs to jointly cover a 60° horizontal FoV already satisfies typical automotive LiDAR requirements and represents a rapid and pragmatic solution. The FoV along the y-direction is 7° for an expected laser tuning range of 50 nm. By multiplexing two tunable lasers, each with a 50 nm tuning range, the vertical FoV can be extended to 14°. Similarly, employing four OPAs in combination with a 100 nm laser tuning range enables a total vertical FoV of 30° and a total horizontal FoV of 60°, thereby meeting the FoV specifications for automotive LiDAR.

The angular resolution along the x-direction is estimated as $\frac{FoV_x}{pixels\,per\,scan\,line} = \frac{30}{64}$ =0.64°. Similarly,the angular resolution along the y-direction is $\frac{FoV_y}{number\,of\,scan\,lines} = \frac{7}{16}$ =0.43°. Although the achieved resolutions are coarser than the 0.1° typically required for automotive LiDAR, they remain within a comparable order of magnitude. Reaching finer angular resolution would necessitate both increasing the number of antennas per block and extending the differential delay lines. However, such a decision is constrained by the relatively high waveguide propagation losses of the employed platform, as it is expected that the total waveguide losses of the chosen design would amount to 16 dB. Additionally the differential delay dictates the wavelength step to move from one resolvable point to the next, which is approximately 0.04 nm, i.e. 5 GHz, which should not compromise the range resolution.

The expected aperture size of the design is 1.5 mm × 2 mm, corresponding to a Rayleigh range of approximately 6 m. Extending the maximum achievable range therefore requires a substantial increase in the effective aperture, which can only be realized by significantly increasing the total number of antennas and employing extremely weak antennas. In this demonstration, increasing the antenna count is not feasible due to limited chip area and high waveguide losses. Moreover, alternative antenna concepts, such as the leaky fin antenna, are incompatible with the employed technology stack and were therefore not considered.

Design parameter	value	Performance metric	value
array pitch	3 µm	FoV_x	30°
aperture width	1.5 mm	$FWHM_x$	0.05°
antennas per block	64	pixel per scan line	64
ΔL	200 µm	number of scan lines	16
Tunability	0.14 ° nm^{-1}	FoV_y	7°
Antenna Strength	7.15 dB mm^{-1}	$FWHM_y$	0.04°

Table 5.1: Design parameters of the pixelated DOPA circuit, and the corresponding beam steering performance for 50 nm *wavelength range.*

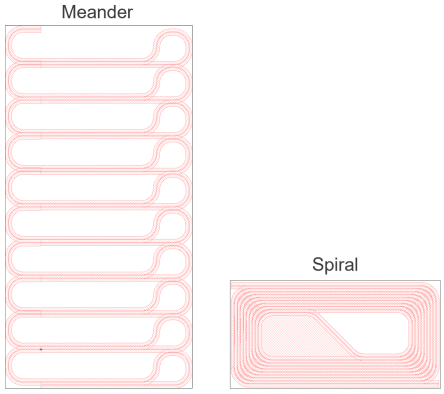

Figure 5.5: The footprint of meander delay line vs. spiral delay line at approximately the same length.

5.2.3 Layout

Delay lines

The delay lines could be implemented based on meanders or spirals, as shown in Fig. 5.5. The spiral shape is more compact. However, the meander shape is chosen as it is well-stackable within the distribution network, where ΔL corresponds to one meander, $2\Delta L$ corresponds to two stacked meanders and so on, as shown in Fig. 5.6. In addition, meanders allow linear progression in the number of bends within the meanders across the tree levels. Within each tree level, the path from one MMI to the next is matched, as shown in Fig. 5.6, so that only the meander contribute to the delay at each level. The meander shape is slightly altered from the one in Fig. 5.5 to have a more uniform waveguide pattern density.

The final full circuit layout is shown in Fig. 5.7, where further design details can be

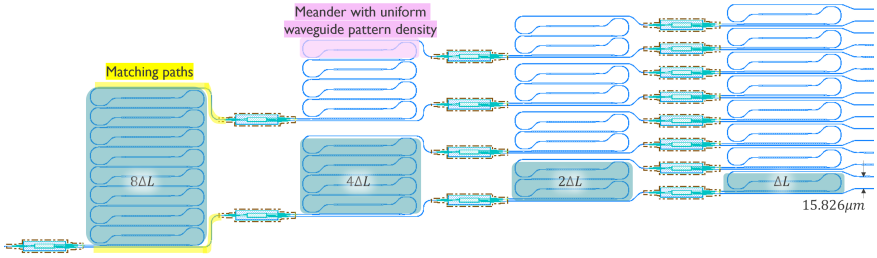

Figure 5.6: Unbalanced splitter tree based on meander delay lines, showing some of the layout considerations.

observed. For instance, phase shifters, to be used for phase errors compensation, are placed at the input to each block and at an intermediate level of the tree. Additionally, a fan-in structure and delay compensation structure are used, which are described below.

Fan-in

Due to the footprint of the delay lines and the MMIs, the output pitch of the distribution network is 15.826 µm, as shown in Fig. 5.6. An L-shaped fan-in is then used to match the output pitch of the distribution network to the antenna array pitch. In this design, the fan-in waveguide length is progressively increasing from one antenna to the next, hence contributing to an extra delay line length.

Due to its higher index contrast, Si has stronger mode confinement as opposed to SiN, which allows going to smaller pitch between the waveguides without optical crosstalk. However, it can be seen that the fan-in waveguides, especially from the top of the circuit, travel a long vertical distance. This requires simulating the cross-coupling length of these waveguides, the cross coupling length L_c follows [118]:

$$L_c = \frac{\lambda}{2\Delta n}, \tag{5.2}$$

where Δn is the effective index difference between the first two eigenmodes of the coupled waveguides. The cross coupling length for a gap of 2 µm is 20 km, while that for a gap of 1 µm is 1 m, as shown in Fig. 5.8. That is why an antenna pitch of 3 µm was a safer choice, so there is no risk of coupling between the fan-in waveguides. The longest path that the fan-in travels is 8 mm, without yet considering the antennas length. This path is approximately 0.1% of the cross coupling length if a pitch of 2 µm was used. To avoid any risk of optical crosstalk, a waveguide superlattice could be used [119]. For the superlattice, each waveguide

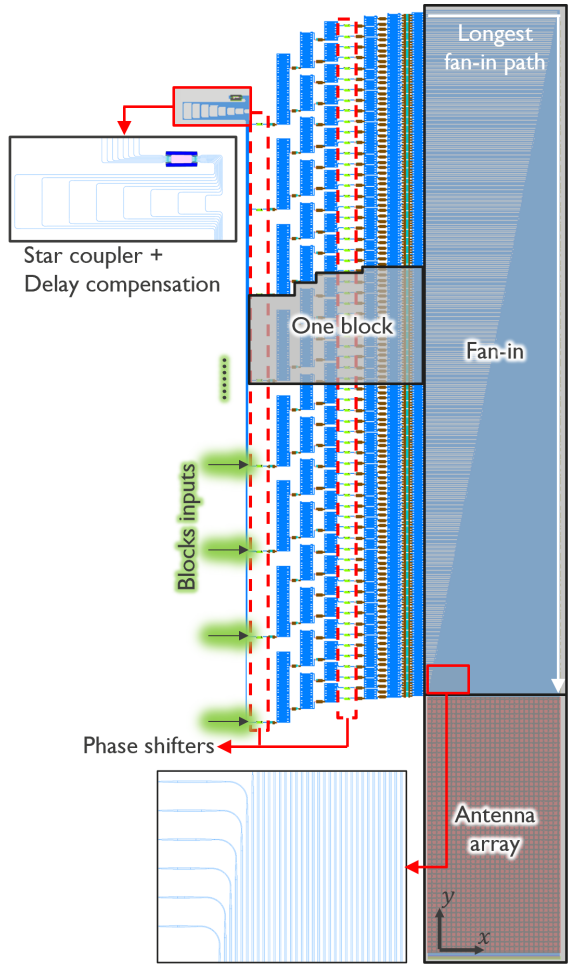

Figure 5.7: The beam steering circuit based on 512-channel pixelated DOPA showing the key layout elements. Note that the figure does not show the metal routing of the phase shifters.

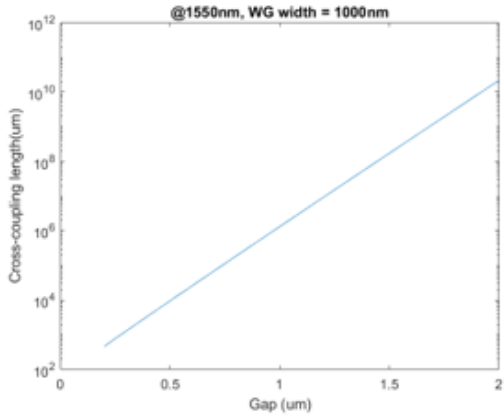

Figure 5.8: Cross coupling length for 1 µm*-wide silicon waveguide for different waveguide gap values.*

width alternates between at least two widths, such that neighboring waveguides do not couple to one another, which would raise the design complexity especially with multimode waveguides.

Delay compensation

The 8 blocks of the pixelated DOPA are fed through the output of an 8×8 star coupler. It is essential that there is no passive phase delay between the first antenna of each block. However, the routing between the star coupler and the inputs to the blocks and the fan-in, breaks the path length matching between the first antenna of each block. That is why a delay compensation is added between the star coupler and the inputs to the blocks. This delay difference could have been integrated in the fan-in or the meanders, but to avoid mistakes we kept this compensation in a separate section.

5.3 Ranging circuit

For a monostatic LiDAR, the ranging circuit consists of the (tunable) laser, the power tap for LO-TX splitting, a circulator, an optical mixer and a (balanced) photodetector, the schematic of such circuit is shown in Fig. 5.9. Here, all the components aside from the laser are described together as the *ranging block*.

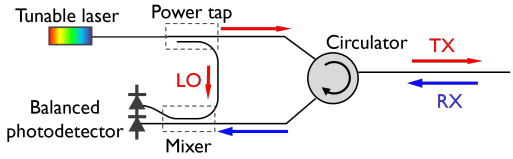

Figure 5.9: Schematic of the ranging circuit for monostatic LiDAR.

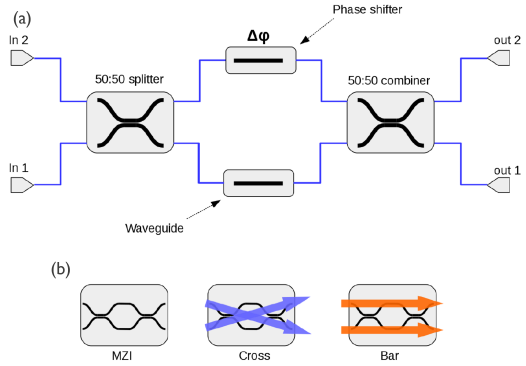

Figure 5.10: Tunable coupler: (a) schematic of MZI-based tunable coupler, consisting of two 50:50 directional couplers for splitting and combining and phase shifter on one or both arms, (b) the tunable coupler operates in a linear combination of cross and bar states, figure from [120].

5.3.1 Ranging block

The power tap and the mixer can be implemented using a directional coupler. Additionally, since there is no available on-chip circulators, a 3 dB coupler can be used instead, which is also essentially a directional coupler. However, a passive directional coupler is inherently dispersive, which means its coupling ratio varies with wavelength, specially when operating over a wide wavelength range. To overcome this, a tunable coupler such as a Mach-Zehnder interferometer (MZI) can be employed, as shown in Fig. 5.10 (a).

Tunable coupler

When used as a tunable power coupler, the MZI is symmetric, meaning that both arms have the same path length. By adding a phase shifter to one or both arms, the tunability is achieved. This configuration can act as a switch that can work in

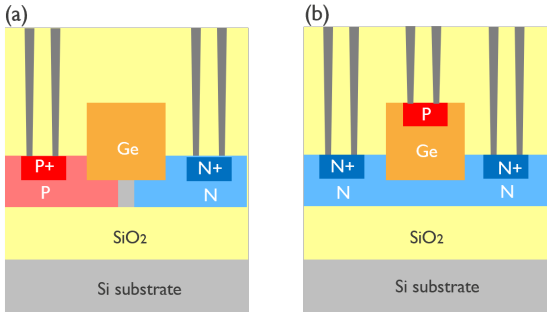

Figure 5.11: (a) Lateral p-i-n photodetector, (b) Vertical p-i-n photodetector.

the cross or bar state, as shown in Fig. 5.10 (b), and can also achieve any power coupling ratio in between. When operating such an MZI in a passive state, within the wavelength band of its passive components, i.e. the phase shifters are off and the phase difference $\phi = 0$, it corresponds to the cross state . When used as a tunable coupler, the MZI operates in a state that is a linear superposition of the bar and cross states, controlled through the differential phase shift between its arms.

Photodetector

The detection is based on a balanced photodetector configuration. Ge photodetectors are used, which are provided by the platform PDK [11, 121]. iSiPP50g platform offers two main kinds of photodetectors: lateral p-i-n (also refered to as monitor photodetector) and vertical p-i-n, as shown in Fig. 5.11. The lateral type has higher responsivity, in addition to lower dark current, but lower bandwidth than the vertical type. This makes the lateral type a good candidate for dealing with weak signals with slow variation. In this context, we used the lateral type with the following specifications: responsivity of 1.08 A/W, bandwidth of 15.3 GHz, and dark current of 7.4 nA.

Layout

The layout realization of the ranging block is shown in Fig. 5.12. It can be seen that all the ports that are not connected to on-chip circuits, are connected to the grating array that is to be connected to the fiber array (FA) for monitoring or for off-chip driving. In addition, the optical path from the mixer to the photodetectors, and the electric path from the photodetectors to the bondpads, are maintained as balanced as possible.

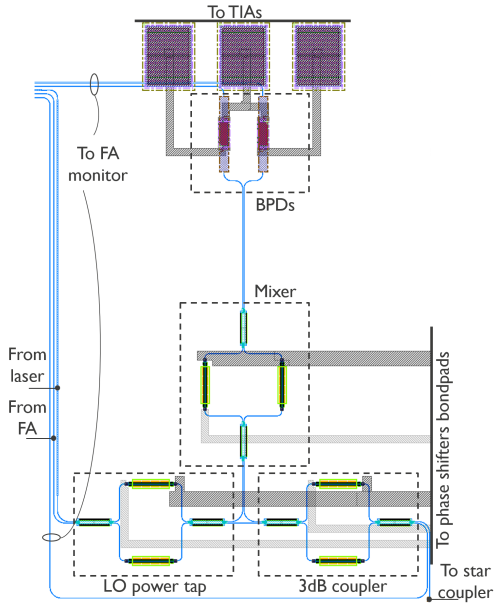

Figure 5.12: Layout of the ranging block. Note that only one phase shifter is used per tunable coupler.

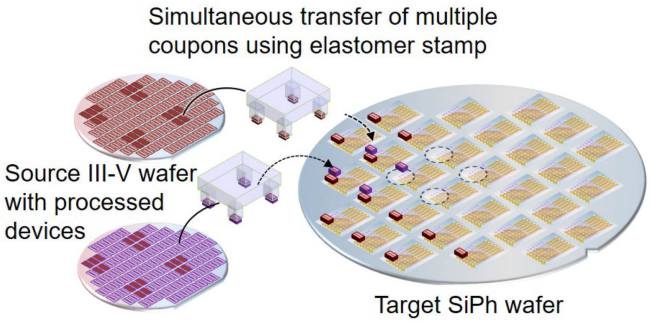

Figure 5.13: Illustration of micro-transfer printing-based integration of III-V devices on silicon photonic wafers, figure from [122]

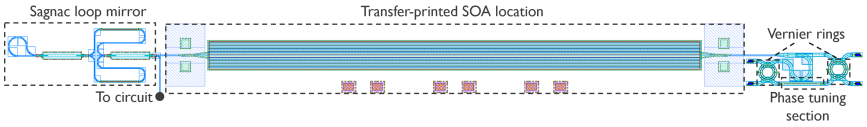

Figure 5.14: Layout of the laser design on the silicon photonics platform.

5.3.2 On-chip lasers

The on-chip tunable lasers used here are based on the micro-transfer-printing (MTP) of indium phosphide (InP) semiconductor optical amplifiers (SOAs) in silicon photonic cavity. In the MTP process, a stamp is used to retrieve a pre-fabricated SOA device (coupon) from the source III-V wafer and print it with a certain accuracy on the designated location on the silicon chip, as shown in Fig. 5.13. Coupling between the III–V device and the silicon waveguide is achieved through tolerant adiabatic tapers.

The laser design is similar to that reported in [123], which is an external cavity laser (ECL). The laser can be conceptually divided into three main sections aside from the SOA: phase tuning section, Vernier filter and Sagnac loop mirror, as shown in Fig. 5.14. The function of each section will be briefly described here, and the interested reader can find more details in various publications by the photonics research group, such as [122]. The laser cavity incorporates a thermo-optic phase tuning section to align the longitudinal modes. Since the InP amplifier provides a wide gain bandwidth, single mode operation is maintained by Vernier filtering. This is realized with two thermally tunable micro-ring resonators of slightly different radii, which together generate an extended effective free spectral

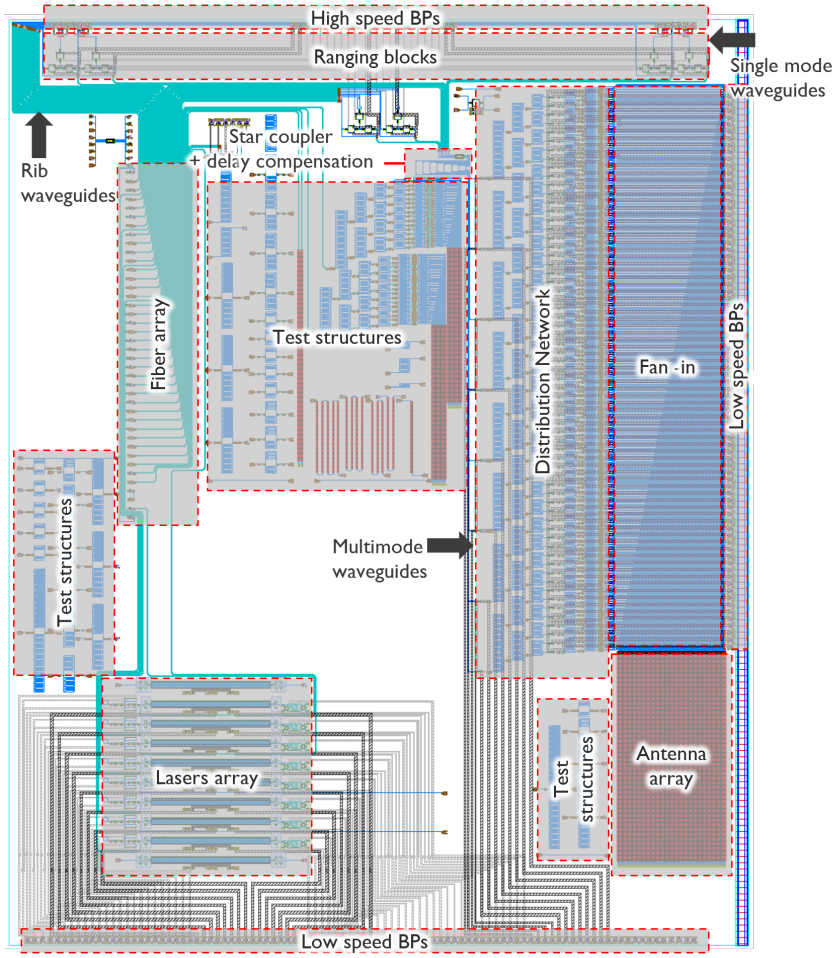

Figure 5.15: The final photonic layout of the LiDAR system.

range (FSR) and thus a broader wavelength tuning span than a single ring could provide. For output coupling, a thermally tunable Sagnac loop mirror based on a Mach-Zehnder interferometer (MZI) is integrated, enabling precise control over the mirror reflectivity.

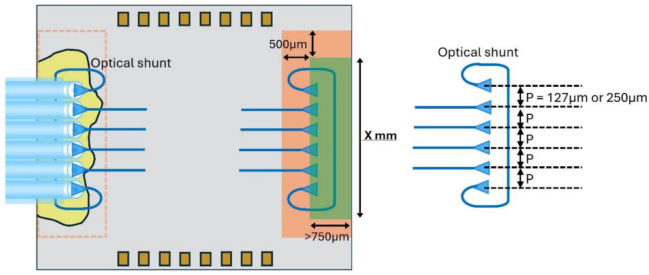

Figure 5.16: Guidelines for chip design for fiber array compatibility, figure from [124]. An exclusion area around the array location should be considered for mechanical bonding. This area should not cover any phase-sensitive components. The pitch between the grating couplers should be 127 µm *or* 250 µm.

5.4 Routing and packaging considerations

The final system layout is shown in Fig. 5.15. The placement and routing of each of the sub-circuits within the floorplan needs to be considered carefully as described below.

5.4.1 Crosstalk

Reducing optical, thermal and electrical crosstalk on the photonic chip is essential. A good example for thermal crosstalk is the on-chip lasers, where the transfer printed SOAs typically consume substantial electrical power, up to a few 100 mW, which in turn generates heat that may spread into adjacent regions. Since thermally sensitive circuitry, such as gratings of the fiber array and the antenna array, can be adversely affected by these temperature fluctuations, it is to preferred to spatially isolate high power elements from them during the layout stage. Consequently, a good location for the lasers array is the bottom left of the chip.

The transfer printed lasers are also a good example for optical crosstalk, as they lack on-chip optical isolation. Therefore, they are sensitive to back-reflections originating from other sections of the circuit. That is why the 3 dB coupler is used in the ranging block despite its power penalty.

Electrical crosstalk can occur when common ground connections are used to reduce the total number of required bondpads. That is why the maximum number of the shared common ground for the phase calibration phase shifters is four.

5.4.2 Optical packaging considerations

For the optical input and readout, i.e. IO ports, fiber arrays can be used to address large number of IO ports, where edge couplers or grating couplers can be used. Edge coupler-based fiber arrays can be realized using a lensed-fiber and integrated spot size converter. It has the advantage of providing high bandwidth, low insertion loss and low polarization sensitivity. However, their alignment during packaging is more challenging. Here, due to the difficulty in alignment and the additional process compatibility issues associated with edge coupling, grating couplers fiber arrays are used with a pitch of 127 µm.

For the fiber array placement, Europractice photonic packaging and assembly standard is followed, as shown in Fig. 5.16. The first and last channel of the grating array are connected to form an optical shunt (alignment loop). This is to be used for the active alignment of the fiber array during the packaging step. During packaging, the first and last channel of the fiber array are aligned to the first and last channel of the grating array with the goal of optimizing the power transmission between these two channels, and hence ensuring the alignment of the intermediate channels.

In addition, all the free ports of any photonic building block, such as the ranging block, are connected to the grating array resulting in 40-channel fiber array, including the optical shunt.

5.4.3 Electrical routing

The electrical wiring can broadly be categorized into high speed (RF) and low speed (DC) routing. The RF lines handle fast devices such as modulators and photodiodes and must be kept short to reduce loss, noise, and crosstalk. They also need to be placed at the chip edge to keep wirebonds as short as possible during packaging. On the other hand, the DC wires are dedicated to slower components, for example heaters, and can tolerate much longer routing lengths without performance concerns. That is why the ranging blocks are placed at the very top of the chip, as the photodetectors of the ranging block need to be as close possible to their high speed bondpads.

5.4.4 Optical waveguide routing

The choice of the routing waveguides in this work favors reducing propagation losses as opposed to compactness. For instance, standard strip waveguides allow tighter bends, while rib geometries can reduce propagation losses. Relatively wide

multimode waveguides can also be introduced to reduce insertion loss and phase fluctuations. As mentioned earlier, multimode waveguides are used for the beam steering circuit. On the other hand, rib waveguide bundles are used for routing between different sub-circuits. The rib waveguide bend radius is 50 µm, and the pitch between the waveguides within a bundle is 20 µm. The routing from the ranging block to the on-chip tunable lasers passes in-between the grating couplers of the fiber array gratings to avoid any crossings and make the routing as dense as possible to give space to other circuits that are not shown here.

5.4.5 Thermal packaging considerations

Temperature variations play a critical role in the performance of photonic circuits and devices, including DOPAs. Thermal perturbations originate from multiple sources, including ambient environmental changes, on-chip electrical heating, and self-heating of active components. These effects can be broadly categorized according to their spatial extent (local versus global). Global temperature variations primarily induce a uniform change in the effective refractive index of the waveguides through the thermo-optic effect, resulting in a collective phase shift across all array elements. In dispersive OPAs, which results in a shift in the wavelength-angle mapping, leading to a deterministic displacement of the far field beam direction. While this effect can be substantial due to the large thermo-optic coefficient of silicon, it is generally slow and highly correlated across the array, enabling compensation through wavelength recalibration or closed-loop feedback using integrated wavelength monitoring. In contrast, local temperature variations produce spatially non-uniform refractive index changes, introducing differential phase errors between array elements. Depending on the temperature gradient, the perturbation in the refractive index can distort the phase front, leading to beam broadening and increase in background level.

The incorporation of active components such as thermo-optic phase shifters and transfer-printed SOAs introduces localized heat sources that can significantly affect the thermal stability of the silicon photonic chip. Without adequate management, these thermal gradients may degrade device performance, alter optical phase relationships, and compromise measurement repeatability. To address this, best practices have been applied as described earlier in terms of components placement to reduce thermal crosstalk. In addition, precise temperature regulation can be achieved using a thermoelectric cooler (TEC) element operating via the Peltier effect, which maintains a controlled environment throughout operation.

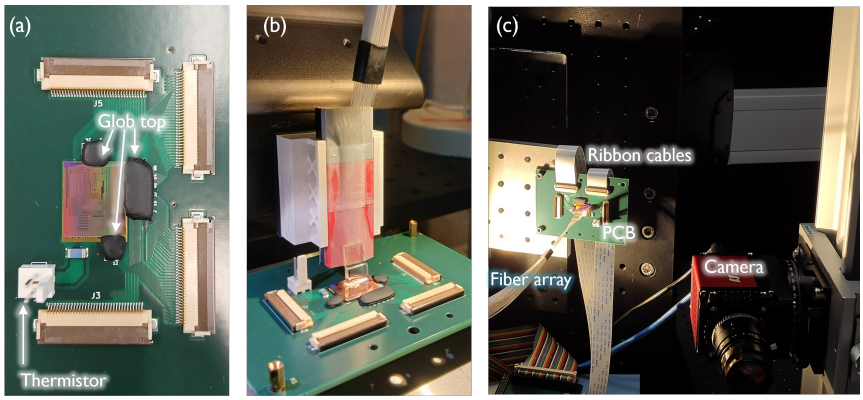

Figure 5.17: packaging Sample packaging: (a) Wirebonded sample to the PCB, where Glob top dispensing is used to protect the wire bonds, (b) Fiber attached sample to a vertical fiber array, (c) Sample connected optically and electrically.

5.5 Sample packaging

5.5.1 Wirebonding

A printed circuit board (PCB) is designed only for the control of the calibration phase shifters on the optical phased array. This is because the integrated photodetectors are not operating properly in the available samples, at the time of writing this thesis. In addition, the transfer printed lasers are not available. The function of the PCB here is to connect the phase shifters to the electric driver.

Wirebonding is the standard approach to link the bond pads on the chip to the corresponding pads on the PCB using fine metal wires. The wirebonding is done at imec, where Aluminum wires are used. In addition, since wire bonds are fragile, glob top dispensing is used, as shown in Fig. 5.17(a). Glob top dispensing involves applying a layer of epoxy or resin over wire bonds to mechanically reinforce them and protect them from damage.

5.5.2 Fiber attachment

The fiber array attachment can be in a horizontal or a vertical configuration to the sample, as shown in Fig. 5.18. The horizontal coupling requires angle polished facet with angle ranging between 40° to 45° depending on the coupling angle of the grating coupler, where total internal reflection occurs at the facet and the

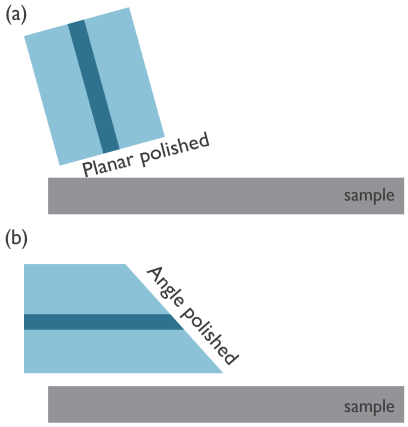

Figure 5.18: Types of fiber array coupling: (a) vertical coupling, and (b) Horizontal or quasi-planar-coupling.

reflected light is coupled into the gratings. It offers larger physical interface with the chip surface, resulting in mechanically stronger attachment compared to vertically mounted ones. However, the quality of the polishing depends on the manufacturer. On the other hand, the vertical coupling requires planar polishing of the fiber and the fiber itself is angled at around 8°. The vertical coupling can be used for prototyping, and it was the choice for the fiber attach for our sample, since there is more in-house experience with it, as shown in Fig. 5.17(b).

5.6 Initial evaluation of the chip

The first characterization of the 512-channel pixelated DOPA was carried out using an external laser source coupled via the fiber array. During fine wavelength sweeps, a strong and persistent background was observed, as shown in Fig. 5.19(a). Because this background remained, it confirmed that the background is not due to the diffraction orders at non-constructive interference wavelengths, and is then attributed to phase errors. The high background level made it challenging to clearly identify the main lobe of the DOPA.

To address this, the integrated correction phase shifters are employed to compensate for phase errors and achieve a collimated far field beam. In this initial phase correction approach, the far field image was analyzed by designating a small region of interest (ROI) corresponding to the expected main lobe position, as shown in Fig. 5.19(b). The goal is to determine the phase shifters state that maximizes the

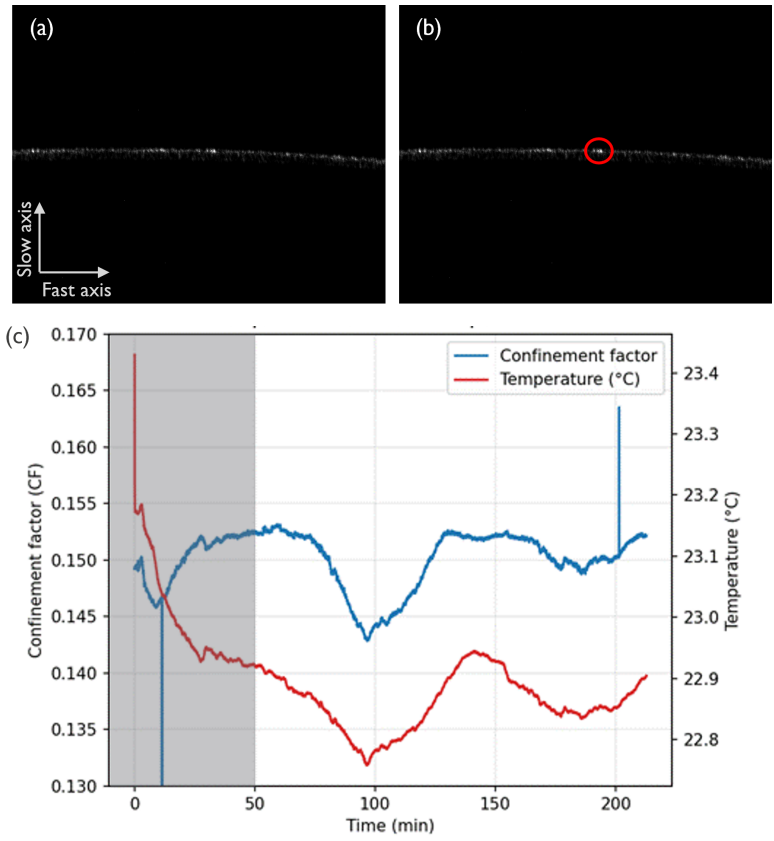

Figure 5.19: Initial work on the pixelated DOPA phase error correction(a) Far field image at 1550 nm *showing a strong background. (b) The same far field image marking the region of interest whose pixel strength is to be maximized, (c) Measurement of the confinement factor and the temperature of the laboratory versus time. The useful measurement starts at 50 min time point. The measurement shows a strong correlation between confinement factor and the temperature of the laboratory.*

confinement factor, defined as the ratio of the camera pixel level within the ROI to the total background level.

However, a significant complication emerged. Any optimization algorithm for phase correction or calibration requires extended run times, but temperature fluctuations in the laboratory during these time spans caused instability in the measured confinement factor. Even with all the phase shifters held at zero voltage, the confinement factor was observed to vary strongly with temperature. This was confirmed by monitoring the PCB-mounted thermistor using a digital multimeter and correlating its resistance measurements with confinement factor variations over a 200-minute interval, as shown in Fig. 5.19(c).

This pronounced temperature sensitivity is a direct consequence of the high thermo-optic coefficient of silicon waveguides, where the rate of change of the refractive index of silicon with temperature $\frac{dn}{dt} = 1.8 \times 10^{-4}/K$ [125], which is further amplified by the long optical delay lines of the dispersive OPA design. As a result, temperature fluctuations hinder the convergence of any algorithm designed to optimize the phase shifters state. Although thermal packaging was originally planned for later stages of the project, once the integrated lasers and well-operating Ge photodetectors are available, it became evident that robust thermal stabilization is essential at this early stage to enable effective calibration of the phase shifters.

Due to these constraints, further work on the characterization and optimization of this chip will be pursued in future efforts once improved thermal control is implemented.

6

Conclusion and Outlook

6.1 Conclusion

Integrated photonics is becoming a key enabler of compact, low-power optical subsystems, including solid-state LiDAR. This thesis advances the field by combining dispersive optical phased arrays (DOPAs) for beam steering with frequency-modulated continuous-wave (FMCW) ranging, addressing both circuit-level implementation and system-level integration for photonic LiDAR.

A central contribution of the work is the introduction and demonstration of pixelated DOPAs, which decouple the specification of beam divergence from that of angular resolution. This motivates the distinction between two classes of DOPA operation: the continuous DOPA, in which a laser wavelength sweep traces a continuous trajectory across the far field, and the pixelated DOPA, in which the far field is

discretized into resolvable spots. Pixelation introduces a new design degree of freedom: the optical aperture can be engineered to project narrow beams over long range while setting a practical value for the angular resolution independently. This enables designers to balance the size, and hence the loss and phase errors, of the distribution network against the desired angular resolution.

Building on these concepts, the thesis presented the circuit-level design and experimental realization of two DOPA proof-of-concept devices fabricated on a silicon-nitride platform. The first prototype followed the continuous scanning approach and constituted the first experimental demonstration of the unbalanced splitter tree architecture. In terms of scalability, this architecture strikes a favorable balance for footprint, loss, and design complexity of the circuit.

A second proof-of-concept prototype implemented a pixelated DOPA, validating its practical feasibility and providing an initial assessment of its far field beam steering capability. An important theme in this study was the impact of phase errors, primarily originating from fabrication-induced effective index variations, which were shown to redistribute power into the background.

The thesis further examined the integration of DOPA-based beam steering with FMCW ranging, proposing a unified LiDAR architecture in which the laser wavelength serves as the sole tuning parameter for both angular scanning and range measurement. We also discussed the new opportunities and considerations of implementing this unified architecture with a swept-source and demonstrated that the pixelated DOPA, regardless of its distribution network architecture, is compatible with wavelength multiplexing.

In the final part of the work, we reported on a medium-scale multiplexed pixelated DOPA integrated with on-chip lasers on a silicon platform, intended as a step toward a fully integrated photonic LiDAR engine. Initial evaluation of the fabricated chip highlighted the need for phase error correction with the current material platform, underlining that future large-scale DOPAs will require improved process control or phase trimming.

6.2 Outlook

The work presented here opens several directions for further investigation before the full potential of the proposed architecture can be assessed.

6.2.1 Medium-scale chip

Beam steering of the medium-scale pixelated DOPA has not yet been experimentally demonstrated, marking the next milestone toward validating multiplexed beam steering. Active phase correction using the integrated phase tuners requires a stabilized chip temperature, as the thermo-optic sensitivity of silicon waveguides is amplified by the long optical delay lines. This is in contrast to actively calibrated OPAs that do not rely on such delay lines. Several open questions remain. How effective is active phase correction in compensating accumulated phase errors, and is there an optimal placement of phase shifters within the unbalanced splitter tree? Furthermore, for a given set of phase shifter states, over what wavelength range does this configuration remain effective before recalibration is needed?

The ranging capability of the integrated system can be assessed incrementally. As a first step, the pixelated DOPA can be used as a transmitter with an external collimating receiver to characterize the far field projection and evaluate the link budget. In this configuration, a tunable laser with external modulation can be employed to assess performance at discrete wavelength points, without performing a continuous wavelength sweep. Subsequently, a monostatic configuration can be implemented using an off-chip ranging engine, initially with a retroreflective target to maximize the return signal. At this point, an important consideration would be the extent to which back-reflections in a monostatic configuration affect the FMCW beat signal. This can then be extended to a setup that combines an off-chip swept laser source (or a tunable laser with external modulation) with the on-chip ranging block in a monostatic arrangement. This step will require designing an RF PCB to drive the on-chip ranging circuitry effectively. Finally, once stable operation of the transfer-printed lasers is achieved, the fully integrated on-chip system can be evaluated to demonstrate beam steering and ranging simultaneously.

6.2.2 Performance optimization

Throughout this thesis, the emphasis has been on demonstrating core functionality rather than maximizing performance. Future work can therefore focus on enhancing the performance of the overall system as well as its individual subcircuits.

Optical antenna Improving the antenna efficiency beyond 50% is critical for improving the link budget. This could be achieved through two-layer grating design or by introducing reflectors between the waveguide layer and the substrate that are designed to maximize upward emission. Developing weak waveguide antennas that support long apertures along the y-axis is important for extending the projection range. This can be investigated by exploring the technological feasibility of transitioning from grating-based to leaky-fin antennas, as discussed in chapter 2. Further, optimizing the antenna tunability to achieve a larger y-axis field of view (FoV) within the operational wavelength range remains relatively unexplored; some promising approaches employ photonic crystal structures. Similarly, tailoring the antenna field profile along the x-axis to suppress grating lobes can significantly improve the link budget by minimizing power leakage into undesired directions. It is evident that no single antenna design satisfies all performance criteria simultaneously, and therefore identifying the most critical design metrics within the intended application context will be essential.

Phase errors and material platform Mitigating phase errors remains a key challenge in advancing dispersive OPAs. While improved fabrication processes is always a solution, such advances are often difficult to achieve in practice. Alternatively, post-fabrication passive phase-trimming techniques applied to the waveguides or antennas could offer a viable means of phase errors correction. This also raises the broader question of material choice within silicon photonics. Silicon enables compact circuits but suffers from higher propagation loss, more phase errors, and stronger thermo-optic coefficient compared to silicon nitride. Furthermore, while increasing laser output power can help offset losses, silicon's nonlinear absorption and limited power-handling capability impose practical constraints on this approach.

Finally, extending phase trimming techniques to dispersive optical phased arrays introduces several additional challenges. First, most existing demonstrations focus on interferometric structures of single delay line, whereas dispersive OPAs require simultaneous calibration of a large number of delay paths, which would require more creative design of experiment and closed-loop feedback methodologies. In this context, investigating phase trimming in wavelength routing components such as arrayed waveguide gratings, where phase errors can be observed directly at the star coupler outputs, may provide a more accessible test platform than free space far field measurements. Furthermore, the optical bandwidth over which phase trimming remains effective is a critical consideration that need to be characterized. Finally, reducing the trimming-induced excess loss is essential, for example by minimizing the overlap between the optical mode and the induced defect through targeted modification of the cladding region, or by distributing weaker defects over

longer interaction lengths.

Components In terms of the x-axis FoV, exploring superlattice waveguide layouts could enable tighter antenna spacing while maintaining low crosstalk. Another key direction is ensuring broadband operation of all passive components, excluding the antennas and delay lines which must remain strongly dispersive to enable beam steering. Finally, minimizing the footprint and optical loss of bends in the long dispersive delay lines will be essential for scaling up to larger apertures.

6.2.3 Further developments

Beyond performance optimization, future research should also focus on system-level enhancements, such as integrating on-chip wavelength monitors for accurate angle measurement and calibration.

From a signal-processing perspective, several open questions remain. In particular, the implications of increasing the laser sweep rate in the swept-source approach, discussed in chapter 4, require further investigation. Potential effects include discontinuities in the beat signal and the receiver response in the presence of multiple simultaneous return signals. Understanding these effects is essential for evaluating the practical limits and benefits of higher sweep rates. Moreover, assessing the accuracy of algorithms that infer the emission angle corresponding to each beat frequency based on wavelength measurements will be critical for constructing accurate 3D point clouds.

A major next step is to demonstrate that the transfer-printed laser can operate as a swept source with a a reasonable tuning range for wavelength multiplexing, while maintaining a narrow linewidth and a highly linear chirp. Achieving these characteristics will enable efficient FMCW ranging. Additionally, integrating on-chip optical isolation could help ensure stable laser operation by mitigating feedback and back-reflections.

Another promising research direction is the development of circuit-level and system-level simulation frameworks for swept-source LiDAR system. An ideal simulator would enable the generation of realistic point clouds for a given scene, given a complete LiDAR system design. Such a simulation platform must capture multiple time scales, encompassing both the optical domain (e.g., the swept source wavelength sweep, and optical propagation) and the electronic domain (e.g., detection, signal conditioning, and digitization). However, existing photonic circuit simulators typically rely on baseband approximations or scattering-matrix formalisms, which are insufficient for accurately modeling the dynamic behavior

of a fully swept-source system. Despite these limitations, partial simulations and reduced-order models that target specific subsystems can already provide valuable design insights. For example, incorporating fabrication-informed models of waveguide phase errors would enable more accurate performance predictions and facilitate the design of photonic circuits that are inherently more robust to phase non-uniformities.

Finally, it is important to identify which of the aforementioned challenges represent critical bottlenecks, and whether any of them are likely to remain prohibitive in the near future. To the best of the author knowledge, Dispersive OPAs with FMCW ranging do not impose more stringent laser power requirements than other scanning LiDAR implementations. In fact, the use of multiplexed ranging engines enables a reduction in the optical power required per laser. Increasing the launched optical power beyond moderate levels is undesirable, as it can induce nonlinear effects in silicon waveguides. Furthermore, in monostatic configurations, optical back-reflections ultimately limit the achievable SNR at high power levels. These considerations indicate that reducing optical losses, rather than increasing laser power, is the most critical performance lever. Encouragingly, both industry and academia are actively pursuing aggressive loss reduction in silicon photonics, driven primarily by the demands of data communication applications. This trend suggests a favorable trajectory for further improvements in passive optical losses. In contrast, the mitigation of phase errors in large-scale photonic circuits remains a comparatively underexplored challenge and is likely to represent a critical research direction for enabling the practical deployment of this architecture.

In summary, the results of this thesis establish the feasibility of wavelength-steered pixelated DOPAs for integrated FMCW LiDAR, while also highlighting the technological challenges, particularly those related to phase errors and their correction. By unifying beam steering and ranging within a single wavelength-controlled photonic chip, this thesis lays the groundwork for compact, low-cost solid-state LiDAR systems, with potential applications extending beyond automotive sensing to robotics and advanced 3D imaging technologies.

References

[1] B. Jalali and S. Fathpour, "Silicon photonics," *Journal of Lightwave Technology*, vol. 24, no. 12, pp. 4600–4615, 2006.

[2] N. Margalit, C. Xiang, S. M. Bowers, A. Bjorlin, R. Blum, and J. E. Bowers, "Perspective on the future of silicon photonics and electronics," *Applied Physics Letters*, vol. 118, p. 220501, 06 2021.

[3] S. Shekhar, W. Bogaerts, L. Chrostowski, J. E. Bowers, M. Hochberg, R. Soref, and B. J. Shastri, "Roadmapping the next generation of silicon photonics," *Nature Communications*, vol. 15, p. 751, Jan 2024.

[4] N. C. Harris, G. R. Steinbrecher, M. Prabhu, Y. Lahini, J. Mower, D. Bunandar, C. Chen, F. N. Wong, T. Baehr-Jones, M. Hochberg, *et al.*, "Quantum transport simulations in a programmable nanophotonic processor," *Nature Photonics*, vol. 11, no. 7, pp. 447–452, 2017.

[5] J. Sun, E. Timurdogan, A. Yaacobi, E. S. Hosseini, and M. R. Watts, "Large-scale nanophotonic phased array," *Nature*, vol. 493, pp. 195–199, Jan 2013.

[6] W. Bogaerts and L. Chrostowski, "Silicon photonics circuit design: Methods, tools and challenges," *Laser & Photonics Reviews*, vol. 12, no. 4, p. 1700237, 2018.

[7] D. S. Boning, S. I. El-Henawy, and Z. Zhang, "Variation-aware methods and models for silicon photonic design-for-manufacturability," *Journal of Lightwave Technology*, vol. 40, no. 6, pp. 1776–1783, 2022.

[8] Y. Xing, J. Dong, U. Khan, and W. Bogaerts, "Capturing the effects of spatial process variations in silicon photonic circuits," *ACS Photonics*, vol. 10, pp. 928–944, Apr 2023.

[9] R. A. Soref and J. P. Lorenzo, "Single-crystal silicon: a new material for 1.3 and 1.6 μm integrated-optical components," *Electronics Letters*, vol. 21, p. 953, Oct. 1985.

[10] A. Rahim, J. Goyvaerts, B. Szelag, J.-M. Fedeli, P. Absil, T. Aalto, M. Harjanne, C. Littlejohns, G. Reed, G. Winzer, S. Lischke, L. Zimmermann, D. Knoll, D. Geuzebroek, A. Leinse, M. Geiselmann, M. Zervas, H. Jans, A. Stassen, C. Domínguez, P. Muñoz, D. Domenech, A. L. Giesecke, M. C. Lemme, and R. Baets, "Open-access silicon photonics platforms in europe," *IEEE Journal of Selected Topics in Quantum Electronics*, vol. 25, no. 5, pp. 1–18, 2019.

[11] S. Y. Siew, B. Li, F. Gao, H. Y. Zheng, W. Zhang, P. Guo, S. W. Xie, A. Song, B. Dong, L. W. Luo, C. Li, X. Luo, and G.-Q. Lo, "Review of silicon photonics technology and platform development," *Journal of Lightwave Technology*, vol. 39, no. 13, pp. 4374–4389, 2021.

[12] R. Soref and B. Bennett, "Electrooptical effects in silicon," *IEEE Journal of Quantum Electronics*, vol. 23, no. 1, pp. 123–129, 1987.

[13] L. Colace, G. Masini, G. Assanto, H.-C. Luan, K. Wada, and L. C. Kimerling, "Efficient high-speed near-infrared ge photodetectors integrated on si substrates," *Applied Physics Letters*, vol. 76, pp. 1231–1233, 03 2000.

[14] M. J. R. Heck, J. F. Bauters, M. L. Davenport, D. T. Spencer, and J. E. Bowers, "Ultra-low loss waveguide platform and its integration with silicon photonics," *Laser & Photonics Reviews*, vol. 8, no. 5, pp. 667–686, 2014.

[15] R. Baets, A. Z. Subramanian, S. Clemmen, B. Kuyken, P. Bienstman, N. Le Thomas, G. Roelkens, D. Van Thourhout, P. Helin, and S. Severi, "Silicon photonics: Silicon nitride versus silicon-on-insulator," in *2016 Optical Fiber Communications Conference and Exhibition (OFC)*, pp. 1–3, 2016.

[16] D. Liang, G. Roelkens, R. Baets, and J. E. Bowers, "Hybrid integrated platforms for silicon photonics," *Materials*, vol. 3, no. 3, pp. 1782–1802, 2010.

[17] W. Xie, T. Komljenovic, J. Huang, M. Tran, M. Davenport, A. Torres, P. Pintus, and J. Bowers, "Heterogeneous silicon photonics sensing for autonomous cars [invited]," *Opt. Express*, vol. 27, pp. 3642–3663, Feb 2019.

[18] G. Roelkens, J. Zhang, L. Bogaert, E. Soltanian, M. Billet, A. Uzun, B. Pan, Y. Liu, E. Delli, D. Wang, V. B. Oliva, L. T. Ngoc Tran, X. Guo, H. Li, S. Qin, K. Akritidis, Y. Chen, Y. Xue, M. Niels, D. Maes, M. Kiewiet, T. Reep, T. Vanackere, T. Vandekerckhove, I. L. Lufungula, J. De Witte, L. Reis, S. Poelman, Y. Tan, H. Deng, W. Bogaerts, G. Morthier, D. Van Thourhout, and B. Kuyken, "Present and future of micro-transfer

printing for heterogeneous photonic integrated circuits," *APL Photonics*, vol. 9, p. 010901, 01 2024.

[19] P. McManamon, "Review of ladar: a historic, yet emerging, sensor technology with rich phenomenology," *Optical Engineering*, vol. 51, no. 6, p. 060901, 2012.

[20] B. Behroozpour, P. A. M. Sandborn, M. C. Wu, and B. E. Boser, "Lidar system architectures and circuits," *IEEE Communications Magazine*, vol. 55, no. 10, pp. 135–142, 2017.

[21] I. Kim, R. J. Martins, J. Jang, T. Badloe, S. Khadir, H.-Y. Jung, H. Kim, J. Kim, P. Genevet, and J. Rho, "Nanophotonics for light detection and ranging technology," *Nature Nanotechnology*, vol. 16, pp. 508–524, May 2021.

[22] T. Baba, T. Tamanuki, H. Ito, M. Kamata, R. Tetsuya, S. Suyama, H. Abe, and R. Kurahashi, "Silicon photonics fmcw lidar chip with a slow-light grating beam scanner," *IEEE Journal of Selected Topics in Quantum Electronics*, vol. 28, no. 5: Lidars and Photonic Radars, pp. 1–8, 2022.

[23] Lumentum, "Automotive LiDAR and In-Cabin Sensing." https://www.lumentum.com/en/diode-lasers/applications/automotive-3d-sensing. Accessed: 17. 06. 2025.

[24] R. Roriz, J. Cabral, and T. Gomes, "Automotive lidar technology: A survey," *IEEE Transactions on Intelligent Transportation Systems*, vol. 23, no. 7, pp. 6282–6297, 2022.

[25] W. Bogaerts, M. Dahlem, S. Dwivedi, R. Jansen, and X. Rottenberg, "Dispersive optical phased array circuit for high-resolution pixelated 2D far-field scanning controlled by a single wavelength variable," in *Smart Photonic and Optoelectronic Integrated Circuits XXII*, p. 112841Z, SPIE, 2020.

[26] Hesai, "HESAI LiDAR." https://www.hesaitech.com/product/atx/. Accessed: 17. 06. 2025.

[27] Cepton, "CEPTON LiDAR." https://www.cepton.com/products/ultra. Accessed: 17. 06. 2025.

[28] Valeo, "Valeo LiDAR." https://www.valeo.com/en/catalogue/cda/long-range-lidar-sensors-valeo-scala-gen-3/. Accessed: 17. 06. 2025.

[29] L. Matthews and G. Garcia, *Laser and eye safety in the laboratory*. New York: IEEE Press, 1995. Includes bibliographical references (p. 73-74) and index.

[30] M. J. Heck, "Highly integrated optical phased arrays: photonic integrated circuits for optical beam shaping and beam steering," *Nanophotonics*, vol. 6, no. 1, pp. 93–107, 2017.

[31] N. Li, C. P. Ho, J. Xue, L. W. Lim, G. Chen, Y. H. Fu, and L. Y. T. Lee, "A progress review on solid-state lidar and nanophotonics-based lidar sensors," *Laser & Photonics Reviews*, vol. 16, no. 11, p. 2100511, 2022.

[32] S. J. Spector, "Review of lens-assisted beam steering methods," *Journal of Optical Microsystems*, vol. 2, no. 1, p. 011003, 2022.

[33] Z. Li, Y. Han, L. Wu, Z. Zang, M. Dai, S. Y. Set, S. Yamashita, Q. Li, and H. Y. Fu, "Towards an ultrafast 3d imaging scanning lidar system: a review," *Photon. Res.*, vol. 12, pp. 1709–1729, Aug 2024.

[34] C. Rogers, A. Y. Piggott, D. J. Thomson, R. F. Wiser, I. E. Opris, S. A. Fortune, A. J. Compston, A. Gondarenko, F. Meng, X. Chen, G. T. Reed, and R. Nicolaescu, "A universal 3d imaging sensor on a silicon photonics platform," *Nature*, vol. 590, pp. 256–261, Feb 2021.

[35] C. Li, X. Cao, K. Wu, G. Qiu, M. Cai, G. Zhang, X. Li, and J. Chen, "Blind zone-suppressed hybrid beam steering for solid-state lidar," *Photon. Res.*, vol. 9, pp. 1871–1880, Sep 2021.

[36] X. Zhang, K. Kwon, J. Henriksson, J. Luo, and M. C. Wu, "A large-scale microelectromechanical-systems-based silicon photonics lidar," *Nature*, vol. 603, pp. 253–258, Mar 2022.

[37] D. Inoue, T. Ichikawa, T. Shimogaki, H. Matsubara, A. Kawasaki, and T. Yamashita, "Solid-state optical scanning device using a beam combiner and switch array," *Optica*, vol. 10, pp. 1358–1365, Oct 2023.

[38] D. A. Miller, "Why optics needs thickness," *Science*, vol. 379, no. 6627, pp. 41–45, 2023.

[39] R. Fatemi, A. Khachaturian, and A. Hajimiri, "A nonuniform sparse 2-d large-fov optical phased array with a low-power pwm drive," *IEEE Journal of Solid-State Circuits*, vol. 54, no. 5, pp. 1200–1215, 2019.

[40] K. V. Acoleyen, W. Bogaerts, J. Jágerská, N. L. Thomas, R. Houdré, and R. Baets, "Off-chip beam steering with a one-dimensional optical phased array on silicon-on-insulator," *Opt. Lett.*, vol. 34, pp. 1477–1479, May 2009.

[41] K. Van Acoleyen, W. Bogaerts, and R. Baets, "Two-dimensional dispersive off-chip beam scanner fabricated on silicon-on-insulator," *IEEE Photonics Technology Letters*, vol. 23, no. 17, pp. 1270–1272, 2011.

[42] D. N. Hutchison, J. Sun, J. K. Doylend, R. Kumar, J. Heck, W. Kim, C. T. Phare, A. Feshali, and H. Rong, "High-resolution aliasing-free optical beam steering," *Optica*, vol. 3, pp. 887–890, Aug 2016.

[43] T. Fukui, R. Tanomura, K. Komatsu, D. Yamashita, S. Takahashi, Y. Nakano, and T. Tanemura, "Non-redundant optical phased array," *Optica*, vol. 8, pp. 1350–1358, Oct 2021.

[44] H. Qiu, Y. Liu, X. Meng, X. Guan, Y. Ding, and H. Hu, "Ultra-sparse aperiodic silicon optical phased array using high-performance thermo-optic phase shifter," *Laser & Photonics Reviews*, vol. n/a, no. n/a, p. 2301177, 2024.

[45] J. C. Hulme, J. K. Doylend, M. J. R. Heck, J. D. Peters, M. L. Davenport, J. T. Bovington, L. A. Coldren, and J. E. Bowers, "Fully integrated hybrid silicon two dimensional beam scanner," *Opt. Express*, vol. 23, pp. 5861–5874, Mar 2015.

[46] N. Dostart, B. Zhang, A. Khilo, M. Brand, K. A. Qubaisi, D. Onural, D. Feldkhun, K. H. Wagner, and M. A. Popović, "Serpentine optical phased arrays for scalable integrated photonic lidar beam steering," *Optica*, vol. 7, pp. 726–733, Jun 2020.

[47] P. Muñoz, D. Pastor, L. A. Bru, G. M. Cabanes, J. Benítez, D. Goodwill, and E. Bernier, "Scalable switched slab coupler based optical phased array on silicon nitride," *IEEE Journal of Selected Topics in Quantum Electronics*, vol. 28, no. 5: Lidars and Photonic Radars, pp. 1–16, 2022.

[48] L. Yu, P. Wang, P. Ma, L. Cui, Z. Wang, Y. Yang, Y. Zhang, and J. Pan, "Two-dimensional beam scanning of passive optical phased array based on silicon nitride delay line," *Journal of Lightwave Technology*, vol. 41, no. 9, pp. 2756–2764, 2023.

[49] Y. Misugi, T. Nakano, and T. Kita, "Silicon-based high-resolution and low-power-consumption two-dimensional beam scanner integrated with hybrid wavelength-tunable laser diode," *Opt. Express*, vol. 32, pp. 13746–13760, Apr 2024.

[50] C. A. Balanis, *Antenna theory: analysis and design*. John wiley & sons, 2016.

[51] R. Mailloux, *Phased Array Antenna Handbook, Second Edition*. Artech House Publishers, 2005.

[52] M. Skolnik, *Introduction to Radar Systems*. Electrical engineering series, McGraw-Hill, 2001.

[53] S. R. Saunders and A. A. Aragón-Zavala, *Antennas and propagation for wireless communication systems*. John Wiley & Sons, 2007.

[54] J. W. Goodman, *Introduction to Fourier optics*. Roberts & Co. Publishers, 2005.

[55] D. Taillaert, *Grating Couplers as Interface between Optical Fibres and Nanophotonic Waveguides*. PhD thesis, Universiteit Gent, 2004.

[56] B. ZHANG, *Design of high performance radiative and resonant silicon photonic devices by efficient control of light propagation and radiation*. PhD thesis, Boston University, 2016.

[57] R. Bruck and R. Hainberger, "Efficient small grating couplers for low-index difference waveguide systems," in *Integrated Optics: Devices, Materials, and Technologies XIII*, vol. 7218, pp. 88–98, SPIE, 2009.

[58] Y. Tang, Z. Wang, L. Wosinski, U. Westergren, and S. He, "Highly efficient nonuniform grating coupler for silicon-on-insulator nanophotonic circuits," *Opt. Lett.*, vol. 35, pp. 1290–1292, Apr 2010.

[59] M. Raval, C. V. Poulton, and M. R. Watts, "Unidirectional waveguide grating antennas with uniform emission for optical phased arrays," *Opt. Lett.*, vol. 42, pp. 2563–2566, Jul 2017.

[60] L. V. Iseghem and W. Bogaerts, "Optical leaky fin waveguide for long-range optical antennas on high-index contrast photonic circuit platforms," *Photon. Res.*, vol. 11, pp. 1570–1582, Sep 2023.

[61] M. Smit and C. Van Dam, "Phasar-based wdm-devices: Principles, design and applications," *IEEE Journal of Selected Topics in Quantum Electronics*, vol. 2, no. 2, pp. 236–250, 1996.

[62] S. Pathak, *Silicon Nano-Photonics Based Arrayed Waveguide Gratings*. PhD thesis, Universiteit Gent, 2014.

[63] W. Bogaerts, S. Dwivedi, R. Jansen, X. Rottenberg, and M. S. Dahlem, "A 2d pixelated optical beam scanner controlled by the laser wavelength," *IEEE Journal of Selected Topics in Quantum Electronics*, vol. 27, no. 1, pp. 1–12, 2021.

[64] T. Goh, S. Suzuki, and A. Sugita, "Estimation of waveguide phase error in silica-based waveguides," *Journal of Lightwave Technology*, vol. 15, no. 11, pp. 2107–2113, 1997.

[65] S. Pathak, M. Vanslembrouck, P. Dumon, D. Van Thourhout, P. Verheyen, G. Lepage, P. Absil, and W. Bogaerts, "Effect of mask discretization on performance of silicon arrayed waveguide gratings," *IEEE Photonics Technology Letters*, vol. 26, no. 7, pp. 718–721, 2014.

[66] R. Adar, C. H. Henry, M. A. Milbrodt, and R. C. Kistler, "Phase coherence of optical waveguides," *Journal of Lightwave Technology*, vol. 12, pp. 603–606, Apr. 1994.

[67] P. Dumon, *Ultra-Compact Integrated Optical Filters in Silicon-on-insulator by Means of Wafer-Scale Technology*. PhD thesis, Universiteit Gent, 2007.

[68] S. K. Selvaraja, W. Bogaerts, P. Dumon, D. Van Thourhout, and R. Baets, "Subnanometer linewidth uniformity in silicon nanophotonic waveguide devices using cmos fabrication technology," *IEEE Journal of Selected Topics in Quantum Electronics*, vol. 16, no. 1, pp. 316–324, 2010.

[69] X. Chen, M. M. Milosevic, D. J. Thomson, A. Z. Khokhar, Y. Franz, A. F. J. Runge, S. Mailis, A. C. Peacock, and G. T. Reed, "Post-fabrication phase trimming of mach–zehnder interferometers by laser annealing of germanium implanted waveguides," *Photon. Res.*, vol. 5, pp. 578–582, Dec 2017.

[70] M. M. Milosevic, X. Chen, W. Cao, A. F. J. Runge, Y. Franz, C. G. Littlejohns, S. Mailis, A. C. Peacock, D. J. Thomson, and G. T. Reed, "Ion implantation in silicon for trimming the operating wavelength of ring resonators," *IEEE Journal of Selected Topics in Quantum Electronics*, vol. 24, no. 4, pp. 1–7, 2018.

[71] H. Jayatilleka, H. Frish, R. Kumar, J. Heck, C. Ma, M. N. Sakib, D. Huang, and H. Rong, "Post-fabrication trimming of silicon photonic ring resonators at wafer-scale," *Journal of Lightwave Technology*, vol. 39, no. 15, pp. 5083–5088, 2021.

[72] L.-R. Robichaud and S. Duval, "Short pulse mid-ir fiber lasers for advanced applications in industry and science," in *2022 Conference on Lasers and Electro-Optics (CLEO)*, pp. 1–2, 2022.

[73] S. Duval, P. Lassonde, F. Légaré, I. Piacentini, and L.-R. Robichaud, "Post-fab laser trimming: Increasing yield and lowering power consumption of pics," in *2024 IEEE CPMT Symposium Japan (ICSJ)*, pp. 208–211, 2024.

[74] Femtum, "Exploring Femtum's Laser Trimming Platform: Achieving Permanent Phase Correction for Advanced Photonic Devices." https://femtum.com/resources/exploring-femtums-laser-trimming-platform-achieving-permanent-phase-correction-for-advanced-photonic-devices/. Accessed: 02. 2026.

[75] T. Kim, P. Bhargava, C. V. Poulton, J. Notaros, A. Yaacobi, E. Timurdogan, C. Baiocco, N. Fahrenkopf, S. Kruger, T. Ngai, Y. Timalsina, M. R. Watts, and V. Stojanović, "A single-chip optical phased array in a wafer-scale silicon photonics/cmos 3d-integration platform," *IEEE Journal of Solid-State Circuits*, vol. 54, no. 11, pp. 3061–3074, 2019.

[76] Y. Li, B. Chen, Q. Na, Q. Xie, M. Tao, L. Zhang, Z. Zhi, Y. Li, X. Liu, X. Luo, G. Lo, F. Gao, X. Li, and J. Song, "Wide-steering-angle high-resolution optical phased array," *Photon. Res.*, vol. 9, pp. 2511–2518, Dec 2021.

[77] D. Kwong, A. Hosseini, J. Covey, Y. Zhang, X. Xu, H. Subbaraman, and R. T. Chen, "On-chip silicon optical phased array for two-dimensional beam steering," *Opt. Lett.*, vol. 39, pp. 941–944, Feb 2014.

[78] P. Wang, G. Luo, Y. Xu, Y. Li, Y. Su, J. Ma, R. Wang, Z. Yang, X. Zhou, Y. Zhang, and J. Pan, "Design and fabrication of a sin-si dual-layer optical phased array chip," *Photon. Res.*, vol. 8, pp. 912–919, Jun 2020.

[79] W. Bogaerts and S. K. Selvaraja, "Compact single-mode silicon hybrid rib/strip waveguide with adiabatic bends," *IEEE Photonics Journal*, vol. 3, no. 3, pp. 422–432, 2011.

[80] F. Vogelbacher, S. Nevlacsil, M. Sagmeister, J. Kraft, K. Unterrainer, and R. Hainberger, "Analysis of silicon nitride partial euler waveguide bends," *Opt. Express*, vol. 27, pp. 31394–31406, Oct 2019.

[81] J. H. Song, T. D. Kongnyuy, P. De Heyn, S. Lardenois, R. Jansen, and X. Rottenberg, "Low-loss waveguide bends by advanced shape for photonic integrated circuits," *Journal of Lightwave Technology*, vol. 38, no. 12, pp. 3273–3279, 2020.

[82] T. Kim, *Realization of Integrated Coherent LiDAR*. PhD thesis, University of California, Berkeley, 2019.

[83] A. Marinins, J. Kjellman, M. Prost, T. D. Kongnyuy, S. Saseendran, M. S. Dahlem, X. Rottenberg, R. Jansen, and P. Soussan, "Bragg reflector co-integrated with sin and a-si on 300 mm wafers for low loss optical beamformers," in *2022 Conference on Lasers and Electro-Optics (CLEO)*, pp. 1–2, 2022.

[84] D. Vercruysse, N. V. Sapra, K. Y. Yang, and J. Vučković, "Inverse-designed optical phased array with a wide steering angle," in *2022 Conference on Lasers and Electro-Optics (CLEO)*, pp. 1–2, 2022.

[85] J. Barry and E. Lee, "Performance of coherent optical receivers," *Proceedings of the IEEE*, vol. 78, no. 8, pp. 1369–1394, 1990.

[86] G. R. Osche, *Optical Detection Theory for Laser Applications*. Wiley, 2002.

[87] A. E. Siegman, "The antenna properties of optical heterodyne receivers," *Appl. Opt.*, vol. 5, pp. 1588–1594, Oct 1966.

[88] P. M. Woodward, *Probability and Information Theory, with Applications to Radar*. Pergamon Press, 1953.

[89] M. A. Richards, J. A. Scheer, and W. A. Holm, *Principles of Modern Radar: Basic principles*. SciTech Publishing, 2010.

[90] M.-C. Amann, T. M. Bosch, M. Lescure, R. A. Myllylae, and M. Rioux, "Laser ranging: a critical review of unusual techniques for distance measurement," *Optical Engineering*, vol. 40, no. 1, pp. 10 – 19, 2001.

[91] A. Vasilyev, *The Optoelectronic Swept-Frequency Laser and Its Applications in Ranging, Three-Dimensional Imaging, and Coherent Beam Combining of Chirped-Seed Amplifiers*. PhD thesis, California Institute of Technology, 2013.

[92] S. Bianconi, P. Ribes-Pleguezuelo, and F. Silvestri, "Requirements for next-generation integrated photonic fmcw lidar sources," *Nature Communications*, vol. 16, p. 6739, Jul 2025.

[93] P. A. M. Sandborn, *FMCW Lidar: Scaling to the Chip-Level and Improving Phase-Noise-Limited Performance*. PhD thesis, University of California, Berkeley, 2017.

[94] T. Baba, T. Tamanuki, H. Ito, M. Kamata, R. Tetsuya, S. Suyama, H. Abe, and R. Kurahashi, "Silicon photonics fmcw lidar chip with a slow-light grating beam scanner," *IEEE Journal of Selected Topics in Quantum Electronics*, vol. 28, no. 5: Lidars and Photonic Radars, pp. 1–8, 2022.

[95] M. Okano and C. Chong, "Swept source lidar: simultaneous fmcw ranging and nonmechanical beam steering with a wideband swept source," *Opt. Express*, vol. 28, pp. 23898–23915, Aug 2020.

[96] P. Shi, L. Lu, C. Liu, G. Zhou, W. Xu, J. Chen, and L. Zhou, "Optical fmcw signal generation using a silicon dual-parallel mach-zehnder modulator," *IEEE Photonics Technology Letters*, vol. 33, no. 6, pp. 301–304, 2021.

[97] H. Hu, Y. He, B. Chen, Z. Wang, Y. Li, Q. Xie, Q. Na, Z. Zhi, X. Li, H. Qu, P. Lo, and J. Song, "Silicon-based optical phased array with a reconfigurable aperture for "gaze" scanning of lidar," *Photon. Res.*, vol. 12, pp. 932–940, May 2024.

[98] X. Zhang, J. Pouls, and M. C. Wu, "Laser frequency sweep linearization by iterative learning pre-distortion for fmcw lidar," *Opt. Express*, vol. 27, pp. 9965–9974, Apr 2019.

[99] N. Satyan, A. Vasilyev, G. Rakuljic, V. Leyva, and A. Yariv, "Precise control of broadband frequency chirps using optoelectronic feedback," *Opt. Express*, vol. 17, pp. 15991–15999, Aug 2009.

[100] T. Hariyama, P. A. M. Sandborn, M. Watanabe, and M. C. Wu, "High-accuracy range-sensing system based on fmcw using low-cost vcsel," *Opt. Express*, vol. 26, pp. 9285–9297, Apr 2018.

[101] S. R. Chinn, E. A. Swanson, and J. G. Fujimoto, "Optical coherence tomography using a frequency-tunable optical source," *Opt. Lett.*, vol. 22, pp. 340–342, Mar 1997.

[102] M. A. Choma, M. V. Sarunic, C. Yang, and J. A. Izatt, "Sensitivity advantage of swept source and fourier domain optical coherence tomography," *Opt. Express*, vol. 11, pp. 2183–2189, Sep 2003.

[103] R. Paschotta, "Wavelength-swept lasers." https://www.rp-photonics.com/wavelength_swept_lasers.html. Accessed: 17. 09. 2025.

[104] G. Lihachev, J. Riemensberger, W. Weng, J. Liu, H. Tian, A. Siddharth, V. Snigirev, V. Shadymov, A. Voloshin, R. N. Wang, J. He, S. A. Bhave, and T. J. Kippenberg, "Low-noise frequency-agile photonic integrated lasers for coherent ranging," *Nature Communications*, vol. 13, p. 3522, Jun 2022.

[105] D. Jeong, H. Jang, M. U. Jung, T. Jeong, H. Kim, S. Yang, J. Lee, and C.-S. Kim, "Spatio-spectral 4d coherent ranging using a flutter-wavelength-swept laser," *Nature Communications*, vol. 15, p. 1110, Feb 2024.

[106] L. Zhang, M. Gagino, A. Millan-Mejia, K. A. Williams, and V. Dolores Calzadilla, "Directly modulated fmcw tunable laser with highly linear frequency chirp and narrow linewidth," *APL Photonics*, vol. 9, p. 106101, 10 2024.

[107] C. Liu, Y. Guo, Y. Zhou, X. Li, L. Lu, Y. Li, W. Bao, J. Chen, and L. Zhou, "Fast-tuning and narrow-linewidth hybrid laser for fmcw ranging," *Laser & Photonics Reviews*, vol. 19, no. 8, p. 2401338, 2025.

[108] B. R. Mahafza, *Radar Systems Analysis and Design Using MATLAB*. Chapman and Hall/CRC, 2005.

[109] Y. Zhai, Q. Liu, H. Li, D. Chen, and Z. He, "Non-mechanical beam-steer lidar system based on swept-laser source," in *2018 Conference on Lasers and Electro-Optics (CLEO)*, pp. 1–2, 2018.

[110] Z. Li, Z. Zang, Y. Han, L. Wu, and H. Y. Fu, "Solid-state fmcw lidar with two-dimensional spectral scanning using a virtually imaged phased array," *Opt. Express*, vol. 29, pp. 16547–16562, May 2021.

[111] P. Feneyrou, L. Leviandier, J. Minet, G. Pillet, A. Martin, D. Dolfi, J.-P. Schlotterbeck, P. Rondeau, X. Lacondemine, A. Rieu, and T. Midavaine, "Frequency-modulated multifunction lidar for anemometry, range finding, and velocimetry-1. theory and signal processing," *Appl. Opt.*, vol. 56, pp. 9663–9675, Dec 2017.

[112] D. Rife and R. Boorstyn, "Single tone parameter estimation from discrete-time observations," *IEEE Transactions on Information Theory*, vol. 20, no. 5, pp. 591–598, 1974.

[113] C. Dragone, "Efficient n*n star couplers using fourier optics," *Journal of Lightwave Technology*, vol. 7, pp. 479–489, 1989.

[114] W. Bogaerts, M. Kandil, and M. S. Dahlem, "Integrated optical beam scanning and fmcw ranging using multiplexed tunable lasers," in *2022 IEEE Photonics Conference (IPC)*, pp. 1–2, 2022.

[115] W. Bogaerts, "Dispersive optical phased array for two-dimensional scanning." https://photonics.intec.ugent.be/publications/patents.asp?ID=152, 2022. Patent No.: US-11249371 B2.

[116] imec, "Prototyping and low-volume manufacturing of silicon photonic ICs." https://www.imeciclink.com/en/asic-fabrication/si. Accessed: 11. 09. 2025.

[117] F. J. Ferraro, P. D. Heyn, M. Kim, N. Rajasekaran, M. Berciano, G. Muliuk, D. Bode, G. Lepage, S. Janssen, R. Magdziak, J. D. Coster, H. Kobbi, S. Lardenois, N. Golshani, L. Shiramin, C. Marchese, S. Rajmohan, S. Nadarajan, N. Singh, S. Radhakrishnan, A. Tsiara, P. Xu, A. Karagoz, D. Yudistira, M. Martire, A. Shahar, M. Chakrabarti, D. Velenis, W. Guo, A. Miller, K. Croes, S. Balakrishnan, P. Verheyen, Y. Ban, J. V. Campenhout, and P. P. Absil, "Imec silicon photonics platforms: performance overview and roadmap," in *Next-Generation Optical Communication: Components, Sub-Systems, and Systems XII* (G. Li, K. Nakajima, and A. K. Srivastava,

eds.), vol. 12429, p. 1242909, International Society for Optics and Photonics, SPIE, 2023.

[118] L. Chrostowski and M. Hochberg, *Silicon Photonics Design: From Devices to Systems*. Cambridge University Press, 2015.

[119] W. Song, R. Gatdula, S. Abbaslou, M. Lu, A. Stein, W. Y.-C. Lai, J. Provine, R. F. W. Pease, D. N. Christodoulides, and W. Jiang, "High-density waveguide superlattices with low crosstalk," *Nature Communications*, vol. 6, p. 7027, May 2015.

[120] A. Ribeiro, *Building Blocks and Subcircuits for Programmable Silicon Photonic Circuits*. PhD thesis, Universiteit Gent, 2019.

[121] P. Absil, K. Croes, A. Lesniewska, P. De Heyn, Y. Ban, B. Snyder, J. De Coster, F. Fodor, V. Simons, S. Balakrishnan, G. Lepage, N. Golshani, S. Lardenois, S. A. Srinivasan, H. Chen, W. Vanherle, R. Loo, R. Boufadil, M. Detalle, A. Miller, P. Verheyen, M. Pantouvaki, and J. Van Campenhout, "Reliable 50gb/s silicon photonics platform for next-generation data center optical interconnects," in *2017 IEEE International Electron Devices Meeting (IEDM)*, pp. 34.2.1–34.2.4, 2017.

[122] G. Roelkens, J. Zhang, L. Bogaert, M. Billet, D. Wang, B. Pan, C. J. Kruckel, E. Soltanian, D. Maes, T. Vanackere, T. Vandekerckhove, S. Cuyvers, J. De Witte, I. L. Lufungula, X. Guo, H. Li, S. Qin, G. Muliuk, S. Uvin, B. Haq, C. Op de Beeck, J. Goyvaerts, G. Lepage, P. Verheyen, J. Van Campenhout, G. Morthier, B. Kuyken, D. Van Thourhout, and R. Baets, "Micro-transfer printing for heterogeneous si photonic integrated circuits," *IEEE Journal of Selected Topics in Quantum Electronics*, vol. 29, no. 3: Photon. Elec. Co-Inte. and Adv. Trans. Print., pp. 1–14, 2023.

[123] E. Soltanian, G. Muliuk, S. Uvin, D. Wang, G. Lepage, P. Verheyen, J. V. Campenhout, S. Ertl, J. Rimböck, N. Vaissiere, D. Néel, J. Ramirez, J. Decobert, B. Kuyken, J. Zhang, and G. Roelkens, "Micro-transfer-printed narrow-linewidth iii-v-on-si double laser structure with a combined 110 nm tuning range," *Opt. Express*, vol. 30, pp. 39329–39339, Oct 2022.

[124] Photonics Packaging and Systems Integration Group, Tyndall National Institute, EUROPRACTICE Partner, "PACKAGING DESIGN RULES and SERVICE." https://europractice-ic.com/wp-content/uploads/2024/11/Photonics-Packaging-Design-Rules-Ver-1.7-Sep-2024.pdf. Accessed: 20. 08. 2025.

[125] B. J. Frey, D. B. Leviton, and T. J. Madison, "Temperature-dependent refractive index of silicon and germanium," in *Optomechanical Technologies*

for Astronomy (E. Atad-Ettedgui, J. Antebi, and D. Lemke, eds.), vol. 6273 of *Society of Photo-Optical Instrumentation Engineers (SPIE) Conference Series*, p. 62732J, June 2006.